FREQUENCY CONVERSION IN NEW NONLINEAR OPTICAL MATERIALS

By

JAMES THOMAS MURRAY

Bachelor of Science

Colorado School of Mines

Golden, Colorado

1989

Submitted to the Faculty of the
Graduate College of the
Oklahoma State University
in partial fulfillment of
the requirements for
the Degree of
MASTER OF SCIENCE
December, 1992

FREQUENCY CONVERSION IN NEW NONLINEAR OPTICAL MATERIALS

Thesis Approved:

Richard C. Powell

Thesis Adviser

Xincheng Xie

James P. Wicksted

Thomas C. Collins

Dean of the Graduate College

ACKNOWLEDGMENTS

It is my sincere pleasure to thank my adviser Dr. Richard C. Powell for giving me the opportunity to work with him. Through his guidance I have gained the skills and confidence needed to be competitive in this field. For this I am greatly in his debt.

I would also like to thank Dr. James Wicksted, Dr. Xin-Cheng Xie and Dr. Roger J. Reeves for kindly serving as the members of my thesis committee.

Acknowledgments are extended to each and every one of my co–group members and to all the members of the OSU Physics Department, especially Dr. P. Westhaus for his endless campaigns to bring me here.

Special thanks is deserving of my collaborators Roger R. Petrin, Dr. Bahaeddin Jassemnejad, Dr. Mahendra G. Jani, and Dr. Petr V. Zverev.

None of this would have been possible had it not been for my family. I inherited my fathers tenacity and work ethic. My soul–mate mother always stood by my side encouraging me all the way. I walked in the foot steps of my oldest brother Tim admiring choice of foot. My twin brother Matthew was a live–in best friend. Life would have been impossible without his presence. My younger sister Sarah always gave her love and confidence freely. My younger brother Joel always has made me feel important.

My wife, Amy who is most deserving of my thanks. If anyone is to be a co–author of this work... she is to be. She typed the entire manuscript, listened to all my lectures on nonlinear optics and answered all my questions on transient stimulated Raman scattering.

I gratefully acknowledge the financial support provided by the U.S. Department of Education Fellowship in Areas of National Needs.

All the materials investigated in this thesis were provided by our friends and collaborators Gabe M. Loiacono and Dominic N. Loiacono of Crystal Associates, Inc..

TABLE OF CONTENTS

LIST OF TABLES

LIST OF FIGURES

Figure Page

Figure Page

Figure Page

CHAPTER I

INTRODUCTION

Coherent optical radiation provides scientists and technologists with highly directional, spectrally pure, optical signals that can be amplified, modulated and transmitted. Thus providing the utility of electrical signals on a spatial-temporal scale equivalent to that of light.

The first coherent source of optical radiation was the ruby laser (λ = 694.3nm) which was introduced in 1960 [1]. Since then, several materials have been found to be useful as laser media. However, most of these sources oscillate at only one wavelength (e.g. Nd:YAG, HeNe, Ar–ion, ect.) and only a few (Ti–Sapphire, Alexandrite, F–center, Cr–Forsterite, Cr–$LiCaAlF_6$, dye) oscillate efficiently over a range of wavelengths. Considerable effort has gone into the research and development of new laser materials to increase the current spectral range.

Frequency conversion in nonlinear media is a viable alternative to the search for new laser materials. The propagation of intense electromagnetic waves through nonlinear media gives rise to electron-ion vibrations at various harmonics of the fundamental frequency, at sum and difference frequencies of two or more fundamental frequencies, and so on. These vibrations give rise to the generation of various order harmonic, sum and difference frequencies in the medium. In this way, the oscillation frequency of a laser source can be transformed into a new spectral region. The frequency conversion processes studied in this thesis are: second harmonic generation (SHG), optical parametric oscillation (OPO), and stimulated Raman scattering (SRS).

SHG employs a nonlinear media to convert an input beam into an output beam with spectral components of both the fundamental and second harmonic where conversion efficiencies of 60% are possible (for a single pass device).

The OPO utilizes a nonlinear media enclosed in an optical cavity. This device provides output with three spectral components; the fundamental, signal, and idler. Here, the fundamental frequency is "split" between the signal and idler components, hence down shifting the frequency of the input (i.e. increasing the wavelength). In this application, the output frequencies are allowed to take on various value with the constraint that energy and momentum are conserved, hence providing for tunable output.

In SRS, the input beam interacts strongly with a phonon mode in the media to produce up (anti–Stokes) and down (Stokes) shifted frequency components in the output. The Stokes and anti–Stokes shifts are independent of the pump beam's wavelength, hence providing shifted frequencies for any wavelength not absorbed by the Raman shifting medium. Raman shifting media can be incorporated inside a laser cavity (intra–cavity Raman shifters) to provide intense, spectrally pure, unidirectional output beams at the Raman shifted frequency of parent laser.

The purpose of the research presented in this thesis is not to re–demonstrate the utility of the aforementioned processes, but rather to present original research on new nonlinear materials used in these nonlinear optical processes. The nonlinear materials under study as efficient SHG and OPO media belong to the family of materials with the formula $MTiOXO_4$ where M is K, Rb ,Tl , NH_4, or Cs and X is P or As. Specifically, the investigated materials include KTP, KTA, RTA, and KCTA.

This family of crystals has been conjectured to have much larger nonlinear figure of merits than the standard materials currently used [2], i.e. $LiNbO_3$, $LiIO_3$, $Ba_2NaNb_5O_{15}$, ADP and KDP. The materials are also easily grown, optically perfect, phase matchable, transparent over a large spectral region, and have large damage thresholds. All these crystals are orthorhombic and belong to the acentric point group $mm2$ (space group $Pna2$). The structure is characterized by chains of TiO_6 octahedra, which are linked at two corners. These chains are separated by either PO_4 or AsO_4 tetrahedra [3]. There are two chains per unit cell and the chain direction alternated between [011] and $[0\bar{1}1]$. Alternating long and short Ti-O bonds occur along these chains, which result in a net $\hat{z}$–directed polarization and are the major contributor to these materials having large nonlinear optic and electro-optic coefficients.

The nonlinear material under study as a SRS media is $Ba(NO_3)_2$. This material is unique among SRS media in that $Ba(NO_3)_2$ is crystalline while most SRS media are either gas or liquid phase devices. $Ba(NO_3)_2$ demonstrates a conversion efficiency that rivals that of conventional devices. The introduction of efficient crystalline SRS media is important for the development of all solid state laser systems which is presently a priority in the field of laser physics and engineering. $Ba(NO_3)_2$ is highly transparent over a large spectral region, has a high damage threshold, and is easily grown from solution. The internal properties of $Ba(NO_3)_2$ will be extensively reviewed in a future section of this thesis.

Summary of Thesis

This thesis is divided into two main parts: theoretical and experimental. The theoretical part is composed of five chapters. These chapters cover the topics of nonlinear optics (NLO), second harmonic generation (SHG), optical parametric oscillation (OPO), phase matching theory (PMT) and stimulated Raman scattering (SRS). Their function is to develope the theory necessary to describe the nonlinear optical processes responsible for the phenomena observed in our experiments.

The second part contains three chapters—one for each of the aforementioned nonlinear optical phenomena. These chapters describe the procedures used and results obtained for each of these experiments.

CHAPTER II

NONLINEAR OPTICAL PHENOMENA

Introduction

When an electro-magnetic wave enters a dielectric media, it is met by electrons bound to positive ion cores. In the presence of this field, the electron-ion pair becomes polarized and is easily driven provided the incident fields oscillate at optical frequencies. These oscillating dipoles in turn regenerate an optical field which is likewise incident on other electron-ion pairs in the material. These pairs become polarized and the process continues throughout the entire media. This is the mechanism responsible for the propagation of optical waves in dielectric media.

For normal optical processes, the electron-ion pair has a linear response to the driving field and thus re–emits an optical wave of the same frequency as the driving field. However, under extraordinary conditions the driving field magnitude can be large enough to rival the internal field E_a which binds the electrons and ions; typically $E_a \sim 3 \times 10^{10}\,\mathrm{V/m}$. Under these conditions, the electron-ion pairs' response is manifestly nonlinear.

The majority of nonlinear optical processes can be described by adding perturbations to the classical model of Drude and Lorentz [4]. This model views the electron-ion pair as being a driven harmonic oscillator. In the limit that the driving field magnitude becomes comparable to the internal electron-ion field, E_a, higher order (anharmonic) perturbation to the potential becomes important and cannot be ignored. In this limit the Hamiltonian of the system becomes

$$H = H_o + H_1 + H_2 + \dots \tag{1}$$

where,

$$H_o = \sum_{i=1}^{3} \left[\frac{p_i^2}{2m} + \frac{m}{2}\omega_i^2 r_i^2 \right] - e\,\vec{r} \cdot \vec{E} \tag{2}$$

is the unperturbed Hamiltonian, and

$$H_1 = \sum_{i,j,k=1}^{3} \beta_{ijk} r_i r_j r_k \ , \tag{3}$$

$$H_2 = \sum_{i,j,k,l=1}^{3} \beta_{ijkl} r_i r_j r_k r_l \tag{4}$$

are the first and second order perturbations.

We start by writing Hamilton's equations of motion for the unperturbed Hamiltonian, i.e.

$$\ddot{r}_i + \gamma_i \dot{r}_i + \omega_i^2 r_i = e\,\mathcal{E}_i \tag{5}$$

where the anisotropic damping term, $\gamma_i \,(\gamma_x \neq \gamma_y \neq \gamma_z)$, is introduced in the usual phenomenological manner [5].

Assuming a linearly polarized driving field of the form

$$\mathcal{E}_i = E_i(\omega_\alpha)\, e^{-i\omega_\alpha t} + E_i^*(\omega_a)\, e^{i\omega_\alpha t} \tag{6}$$

we find, by substitution of the Fourier series

$$r_i = \sum_{n=\infty}^{-\infty} r_i(\omega_n)\, e^{i\omega_n t}\,, \tag{7}$$

the solutions

$$r_i(\omega_\alpha) = \frac{e\, E_i(\omega_\alpha)}{\omega_i^2 - \omega_a^2 + i\,\gamma_i\,\omega_a}\,. \tag{8}$$

The unperturbed displacement $r_i(\omega_\alpha)$ in Eq.8 gives rise to the unperturbed polarization $p_i(\omega_\alpha) = \epsilon_o e r_i(\omega_\alpha)$. For N oscillators per unit volume the linear polarization of the materials simply

$$\begin{aligned} P_i(\omega_\alpha) &= N\, p_i(\omega_\alpha) \\ &= N\, e\, r(\omega_\alpha) \\ &= \frac{N\, e^2\, E_i(\omega_\alpha)}{\omega_i^2 - \omega_\alpha^2 + i\gamma_i\omega_\alpha} \end{aligned} \tag{9}$$

Defining the susceptibility in the normal manner, $P_i(\omega_\alpha) = \chi_i^{(1)}(\omega_\alpha) E_i(\omega_\alpha)$, we find

$$\chi_i^{(1)}(\omega_\alpha) = \frac{N\ e^2}{\omega_i^2 - \omega_\alpha^2 + i\gamma_i(\omega_\alpha)}, \tag{10}$$

which is the central result of the Drude, Lorentz model.

The first order perturbation to the electrons motion can be found by considering the first order correction to the Hamiltonian, i.e.

$$H^{(1)} = H_o + H_1. \tag{11}$$

Before we apply Hamilton's equation of motion to Eq.11 we first note that many terms in the sum $\sum_{i,j,k=1}^{3} \beta_{ijk} r_i r_j r_k$ are equivalent. This point is made more clear when the origin of the expansion coefficients β_{ijk} is exposed. By expanding the electron-ion potential, V, in a Taylor Series we find

$$\begin{aligned} V &= V_o + \sum_i \left(\frac{\partial V}{\partial r_i}\right)_o r_i + \sum_{ij} \left(\frac{\partial^2 V}{\partial r_i \partial r_j}\right)_o r_i r_j + \sum_{ijk} \left(\frac{\partial^3 V}{\partial r_i \partial r_j \partial r_k}\right)_o r_i r_j r_k + \ldots \\ &= V_o + \sum_i \beta_i r_i + \sum_{ij} \beta_{ij} r_i r_j + \sum_{ijk} \beta_{ijk} r_i r_j r_k + \ldots \end{aligned} \tag{12}$$

From the expansion it is clear that

$$\beta_{ijk} = \beta_{kij} = \beta_{jki} \tag{13}$$

and

$$\beta_{ijk} = \beta_{ikj} = \beta_{jik} \, . \tag{14}$$

The number of items in the sum can be greatly reduced by defining the tensor

$$\nu_{ijk} = \beta_{ijk} + \beta_{ikj} + \beta_{jik} \tag{15}$$

which preserves the permutation symmetry, i.e. $\nu_{ijk} = \nu_{kij} = \nu_{jki}$.

We continue by applying Hamilton's equations of motion to the corrected Hamiltonian in Eq.11. We find the equations of motion to be given by

$$\ddot{r}_i + \gamma_i \dot{r}_i + \omega_i^2 r_i + \sum_{j,k=1}^{3} \nu_{ijk} r_j r_k = e\,\mathcal{E}_i \, . \tag{16}$$

To further generalize the solution we will assume the driving field has two driving frequencies ω_α and ω_β, thus

$$\mathcal{E}_i = 2 \ \Re_e \{ E_i(\omega_\alpha) e^{i\omega_\alpha t} + E_i(\omega_\beta) e^{i\omega_\beta t} \} \tag{17}$$

Note that the real amplitude of the wave is $2 \mid \mathcal{E} \mid$; which is half the amplitude of the usual definition. This convention, introduced by Pershan [6], leaves the linear susceptibility unchanged but increases the lowest order nonlinear susceptibility by a factor of two. Additional factors of two appear in higher order susceptibilities. This convention is advantageous when discussing the symmetry properties of the nonlinear susceptibilities.

We now substitute in Eq.7 for r_i, and Eq.17 for $\mathcal{E}_i$ into Eq.16. Collecting terms in various orders of $e^{i\omega_n t}$, we find

$$[e^{i\omega_a t}]: \; -\omega_a^2 r_i(\omega_\alpha) + i\Gamma_i \omega_\alpha r_i(\omega_\alpha) + \omega_i^2 r_i(\omega_a) = e \; E_i(\omega_\alpha) \;, \tag{18}$$

$$[e^{i\omega_\beta t}]: \; -\omega_\beta^2 r_i(\omega_\beta) + i\Gamma_i \omega_\beta r_i(\omega_\beta) + \omega_i^2 r_i(\omega_\beta) = e \; E_i(\omega_\beta) \;, \tag{19}$$

$$[e^{i(\omega_\alpha+\omega_\beta)t}]: \; \begin{array}{c} -(\omega_\alpha+\omega_\beta)^2 r_i(\omega_a+\omega_\beta) + i\Gamma_i(\omega_\alpha+\omega_\beta) + \omega_o^2 r_i(\omega_a+\omega_\beta) \\ +\nu_{ijk} r_j(\omega_a) r_k(\omega_\beta) + \nu_{ijk} r_j(\omega_\beta) r_k(\omega_\alpha) = 0 \end{array} \tag{20}$$

and

$$[e^{i(\omega_\alpha-\omega_\beta)t}]: \; \begin{array}{c} -(\omega_\alpha-\omega_\beta)^2 r_i(\omega_a-\omega_\beta) + i\Gamma_i(\omega_\alpha-\omega_\beta) + \omega_o^2 r_i(\omega_a-\omega_\beta) \\ +\nu_{ijk} r_j(\omega_a) r_k^*(\omega_\beta) + \nu_{ijk} r_j^*(\omega_\beta) r_k(\omega_\alpha) = 0 \end{array} \; . \tag{21}$$

The solutions of Eq.18 and Eq.19 are given by

$$r_i(\omega_\alpha) = \frac{e \; E_i(\omega_\alpha)}{\omega_i^2 - \omega_\alpha^2 + i\Gamma_i\omega_\alpha} = \frac{e \; E_i(\omega_\alpha)}{\Delta_i(\omega_\alpha)} \tag{22}$$

and

$$r_i(\omega_\beta) = \frac{e \; E_i(\omega_\beta)}{\omega_i^2 - \omega_\beta^2 + i\Gamma_i\omega_\beta} = \frac{e \; E_i(\omega_\beta)}{\Delta_i(\omega_\beta)} \; . \tag{23}$$

These solutions describe the linear, unperturbed response of the electron to the driving fields. If we now substitute the linear responses $r_i(\omega_\alpha)$ and $r_i(\omega_\beta)$ into Eqs.20 and 21, and solve for $r_i(\omega_\alpha \pm \omega_\beta)$, we find

$$r_i(\omega_\alpha+\omega_\beta) = \frac{-\nu_{ijk} e^2 E_j(\omega_\alpha) E_k(\omega_\beta)}{\Delta_i(\omega_\alpha+\omega_\beta)\Delta_j(\omega_\alpha)\Delta_k(\omega_\beta)} - \frac{\nu_{ijk} e^2 E_j(\omega_\beta) E_k(\omega_\alpha)}{\Delta_i(\omega_\alpha+\omega_\beta)\Delta_j(\omega_\beta)\Delta_k(\omega_\alpha)} \tag{24}$$

and

$$r_i(\omega_\alpha-\omega_\beta) = \frac{-\nu_{ijk} e^2 E_j(\omega_\alpha) E_k^*(\omega_\beta)}{\Delta_i(\omega_\alpha-\omega_\beta)\Delta_j(\omega_\alpha)\Delta_k^*(\omega_\beta)} - \frac{\nu_{ijk} e^2 E_j^*(\omega_\beta) E_k(\omega_\alpha)}{\Delta_i(\omega_\alpha-\omega_\beta)\Delta_j^*(\omega_\beta)\Delta_k(\omega_\alpha)} \; . \tag{25}$$

The solutions to the perturbed displacement $r_i(\omega_\alpha \pm \omega_\beta)$ give rise to a perturbed polarization $p_i(\omega_\alpha \pm \omega_\beta) = \epsilon_o e r_i(\omega_\alpha \pm \omega_\beta)$. Following the same arguments leading up to Eq.10 we find the perturbed polarizations of the media to be

$$\begin{aligned} P_i(\omega_a + \omega_\beta) = & \sum_{jk} \chi^{(2)}_{ijk}(\omega_\alpha + \omega_\beta; \omega_\alpha, \omega_\beta) E_j(\omega_\alpha) E_k(\omega_\beta) \\ & + \sum_{jk} \chi^{(2)}_{ijk}(\omega_\alpha + \omega_\beta; \omega_\beta, \omega_\alpha) E_j(\omega_\beta) E_k(\omega_\alpha) \end{aligned} \tag{26}$$

and

$$\begin{aligned} P_i(\omega_a - \omega_\beta) = & \sum_{jk} \chi^{(2)}_{ijk}(\omega_\alpha - \omega_\beta; \omega_\alpha, \omega_\beta) E_j(\omega_\alpha) E^*_k(\omega_\beta) \\ & + \sum_{jk} \chi^{(2)}_{ijk}(\omega_\alpha - \omega_\beta; \omega_\beta, \omega_\alpha) E^*_j(\omega_\beta) E_k(\omega_\alpha) \, , \end{aligned} \tag{27}$$

where

$$\chi^{(2)}_{ijk}(\omega_\alpha + \omega_\beta; \omega_\alpha, \omega_\beta) = - \frac{\epsilon_o \, N \, e^3 \nu_{ijk}}{\Delta_i(\omega_\alpha + \omega_\beta)\Delta_j(\omega_\alpha)\Delta_k(\omega_\beta)} \tag{28}$$

and

$$\chi^{(2)}_{ijk}(\omega_\alpha - \omega_\beta; \omega_\alpha, \omega_\beta) = - \frac{\epsilon_o \, N \, e^3 \nu_{ijk}}{\Delta_i(\omega_\alpha - \omega_\beta)\Delta_j(\omega_\alpha)\Delta^*_k(\omega_\beta)} \, . \tag{29}$$

Equations 26 and 27 represent the source terms responsible for the generation of the optical fields of frequency $\omega_\alpha \pm \omega_\beta$, propagating in the media. These nonlinear source terms will be used extensively in future sections to describe the nonlinear optical phenomena: SHG, OPO and SRS.

The continued addition of higher order perturbations results in higher order nonlinearities in the driving polarizations. All additional orders can be combined under one sum to yield the generalized nonlinear source polarization:

$$P_i = \chi^{(1)}_{ij} E_j + \chi^{(2)}_{ijk} E_j E_k + \chi^{(3)}_{ijkl} E_j E_k E_l + ... \tag{30}$$

Coupled Wave Equations

We are now in a position to derive a coupled set of wave equations generated by the nonlinear driving polarization. We start by writing Maxwell's equations in a dispersive media, namely

$$\vec{\nabla} \otimes \vec{E} \;=\; -\frac{\partial \vec{B}}{\partial t} \tag{31}$$

$$\vec{\nabla} \otimes \vec{H} \;=\; \frac{\partial \vec{D}}{\partial t} + \vec{J} \tag{32}$$

$$\begin{aligned}\vec{\nabla}\cdot\vec{E} &= \tfrac{\rho}{\epsilon_o} && (33)\\ \vec{\nabla}\cdot\vec{B} &= 0 && (34)\end{aligned}$$

with the constitutive relations

$$\begin{aligned}\vec{D} &= \epsilon\vec{E}+\vec{P}\\ \vec{J} &= \sigma\vec{E}\\ \vec{B} &= \mu\vec{H}\end{aligned} \qquad (35)$$

Taking the curl of Eq.31, assuming a non-magnetic media, we find

$$\begin{aligned}\vec{\nabla}\otimes\left(\vec{\nabla}\otimes\vec{E}\right) &= -\tfrac{\partial}{\partial t}\left(\vec{\nabla}\otimes\vec{B}\right)\\ &= -\mu\tfrac{\partial}{\partial t}\left(\vec{\nabla}\otimes\vec{H}\right)\end{aligned} . \qquad (36)$$

Upon substitution of Eq.32 into Eq.36 we find

$$\vec{\nabla}\otimes\left(\vec{\nabla}\otimes\vec{E}\right) = -\mu\frac{\partial}{\partial t}\left(\frac{\partial\vec{D}}{\partial t}+\vec{J}\right). \qquad (37)$$

Using a well-known vector identity we can rewrite the left-hand side of Eq.37 as

$$\vec{\nabla}\otimes\left(\vec{\nabla}\otimes\vec{E}\right) = \nabla\left(\vec{\nabla}\cdot\vec{E}\right)-\nabla^2\vec{E}. \qquad (38)$$

Upon substitution of Eq.33 and Eq.35 into Eq.38 we find

$$\vec{\nabla}\left(\frac{\rho}{\epsilon_o}\right)-\nabla^2\vec{E} = -\mu\frac{\partial}{\partial t}\left[\frac{\partial}{\partial t}\left(\epsilon\vec{E}+\vec{P}\right)+\sigma\vec{E}\right]. \qquad (39)$$

Assuming a dielectric media, Eq.39 becomes

$$\nabla^2\vec{E}-\mu\sigma\frac{\partial\vec{E}}{\partial t}-\mu\epsilon\frac{\partial^2\vec{E}}{\partial t^2} = \mu\frac{\partial\vec{P}}{\partial t}. \qquad (40)$$

This wave equation describes the electric field in a medium generated by the driving polarization $\vec{P}$.

The fields in Eq.40 are the instantaneous fields. As was done previously, it is customary to define the nonlinear susceptibility not in terms of the instantaneous fields but rather their Fourier components defined by

$$\vec{\mathcal{E}}(\vec{r},t) = \frac{1}{2}\left[\vec{E}(\vec{r},\omega)e^{i\left(\vec{k}\cdot\vec{r}-\omega t\right)}+c.c.\right] \qquad (41)$$

and

$$\mathcal{P}(\vec{r},t) = \frac{1}{2}\left[\vec{P}(\vec{r},t)e^{i(\vec{k}\cdot\vec{r}-\omega t)} + c.c.\right]. \tag{42}$$

We now assume propagation in an arbitrary direction, say $\vec{r} = z\hat{z}$, to reduce Eq.40 to a one-dimensional equation. Substituting Eq.41 and Eq.42 into Eq.40 and differentiating, we find the equation

$$\begin{aligned} \frac{1}{2}\frac{\partial^2 E(\omega)}{\partial z^2} + ik\frac{\partial E(\omega)}{\partial z} - \frac{\mu\sigma}{2}\frac{\partial E(\omega)}{\partial t} &+ \frac{i\omega\mu\sigma}{2}E(\omega) - \frac{\mu\epsilon}{2}\frac{\partial^2 E(\omega)}{\partial t^2} + i\omega\mu\epsilon\frac{\partial E(\omega)}{\partial t} \\ &= \frac{\mu}{2}\frac{\partial^2 P(\omega)}{\partial t^2} - i\omega\mu\frac{\partial P(\omega)}{\partial t} - \frac{\omega^2\mu}{2}P(\omega)\,. \end{aligned} \tag{43}$$

The slowly varying amplitude approximation encompasses the following assumptions:

$$\omega^2 P(\omega) \gg \omega\frac{\partial P(\omega)}{\partial t} \gg \frac{\partial^2 P(\omega)}{\partial t^2}, \tag{44}$$

$$\omega E(\omega) \gg \frac{\partial E(\omega)}{\partial t}$$

and

$$k\frac{\partial E(\omega)}{\partial z} \gg \frac{\partial^2 E(\omega)}{\partial z^2}. \tag{45}$$

With these approximations, the wave equation in Eq.43 reduces to

$$ik\frac{\partial E(\omega)}{\partial z} + \frac{i\omega\mu\sigma}{2}E(\omega) + i\omega\mu\epsilon\frac{\partial E(\omega)}{\partial t} = -\frac{\omega^2\mu}{2}P(\omega)\,. \tag{46}$$

Dividing by ik we find

$$\frac{\partial E(\omega)}{\partial z} + \alpha E(\omega) + \frac{1}{v}\frac{\partial E(\omega)}{\partial t} = \frac{i\mu c\omega}{2n}P(\omega) \tag{47}$$

where we have used $k = n\omega/c$, $\mu\epsilon = 1/v^2$ and defined $\alpha = \mu\sigma c/2$ as the electric field loss coefficient. When a nonlinear polarization is substituted into Eq.47, a set of coupled equations will arise. This set of equations can then be solved simultaneously to yield the fields associated with each frequency component arising from the perturbed polarization.

CHAPTER III

SECOND HARMONIC GENERATION

Introduction

Second harmonic generation (SHG) was first observed by Franken et al. [7] in 1961 shortly after the advent of the laser and was explained shortly thereafter [8–13]. In his experiments, a ruby laser oscillating at λ_p =694.3nm, was focused on the front surface of a crystalline quartz plate. The emergent radiation was analyzed by a spectrometer and was found to contain radiation at twice the input frequency (i.e. λ =347.15nm).

The conversion efficiency of this first experiment was only on the order $\sim 10^{-8}$. It will be shown that conversion efficiencies of $\sim 10^{-1}$ can easily be achieved and efficiencies approaching unity are possible by utilizing efficient materials and index matching techniques.

Theory

SHG most typically is generated by the nonlinear polarization

$$P_i(2\omega) = \epsilon_o \chi^{(2)}_{ijk}(2\omega; \omega, \omega) E_j(\omega) E_k(\omega) \,. \tag{48}$$

However, SHG can be obtained through higher order nonlinearities if one or more of the frequency's components is zero or negative [10,11]. For example, SHG via a third order nonlinearity can be produced by the term

$$P_i^{NLS}(2\omega) = \epsilon_o \chi^{(3)}_{ijkl}(2\omega; \omega, \omega, 0) E_j(\omega) E_k(\omega) E_l(0) \,. \tag{49}$$

It is customary to write the nonlinear second order susceptibility in terms of the components of the piezo-electric $\tilde{d}$ tensor. As a result of using Pershan's convention for the definition of the field magnitudes in Eq.17, the trivial relation for the nonlinear susceptibility follows:

$$\chi^{(2)}_{ijk}(\omega_3;\omega_1,\omega_2) = d_{ijk}(\omega_3;\omega_2,\omega_1)\,. \tag{50}$$

It should be pointed out that although the number of conventions is almost as numerous as the number of authors, the resulting second order nonlinear polarization,

$$P_i(\vec{r},\omega_3) = \epsilon_o d_{ijk}(\omega_3;\omega_2,\omega_1)E_j(\vec{r},\omega_1)E_k(\vec{r},\omega_2)e^{i(\vec{k}_1+\vec{k}_2-\vec{k}_3)\cdot\vec{r}} \tag{51}$$

is universal.

The $i^{\underline{th}}$ component of the polarization, responsible for driving the second harmonic field, can therefore be written as

$$P_i(\vec{r},2\omega) = \epsilon_o d_{ijk}(2\omega;\omega,\omega)E_j(\vec{r},\omega)E_k(\vec{r},\omega)e^{i(2\vec{k}_\omega-\vec{k}_{2\omega})\cdot\vec{r}} \tag{52}$$

where we have used $\omega_1 = \omega_2 = \omega$ and $\omega_3 = 2\omega$ in Eq.51. Equation 52 can be converted into an expression relating the magnitude of the driving polarization to the magnitude of the electric field, $E(\omega)$, by utilizing the geometrical relationships

$$\begin{aligned} P_i(\vec{r},2\omega) &= a_iP(\vec{r},2\omega) &&= a_iP_2(\vec{r}) \\ E_j(\vec{r},\omega) &= a_jE(\vec{r},\omega) &&= a_jE_1(\vec{r}) \\ E_k(\vec{r},\omega) &= a_kE(\vec{r},\omega) &&= a_kE_1(\vec{r}) \end{aligned} \tag{53}$$

where a_i, a_j and a_k are the direction cosines and $F_n(\vec{r}) = F(\vec{r},\omega_n)$, where F is either P or E. The magnitude of the driving polarization can therefore be written as

$$\begin{aligned} P_2(\vec{r}) &= \epsilon_o a_i d_{ijk} a_j a_k E_1(\vec{r})E_1(\vec{r})e^{i(2\vec{k}_\omega-\vec{k}_{2\omega})\cdot\vec{r}} \\ &= d_{eff}E_1(\vec{r})E_1(\vec{r})e^{-i\Delta\vec{k}\cdot\vec{r}} \end{aligned} \tag{54}$$

where $d_{eff} = \epsilon_o a_i d_{ijk} a_j a_k$ is the effective second-order nonlinear coefficient and $\Delta\vec{k} = k_{2\omega} - 2\vec{k}_\omega$ is the phase mismatch vector.

We are now in a position to calculate the magnitude of the generated second-harmonic field, $E_2(\vec{r})$. Substituting the driving polarization of Eq.54 into Eq.47, assuming the media is lossless (i.e. $\alpha = 0$), we find the differential equation in the steady-state limit (i.e. $\frac{\partial E}{\partial t} = 0$)

$$\begin{aligned} \frac{dE_2(z)}{dz} &= \frac{i\mu_o c\omega}{2n(2\omega)} d_{eff} E_1(z) E_1(z) e^{i(2\vec{k}_\omega - \vec{k}_{2\omega})\cdot\vec{r}} \\ &= i\kappa_{2\omega} E_1(z) E_1(z) e^{-i\Delta k z} \end{aligned} \tag{55}$$

where

$$\kappa_{2\omega} = \frac{\mu_o c\omega}{2n(2\omega)} d_{eff} \,. \tag{56}$$

Equation 55 cannot be solved without prior knowledge of $E_1(z)$. Hence, we must find a similar equation in terms of $E_1(z)$. As with $E_2(z)$ the field $E_1(z)$ is driven by a nonlinear polarization field. This field can be determined by substituting $\omega_3 = \omega$, $\omega_2 = 2\omega$ and $\omega_1 = -\omega$ into Eq.51 which yields the magnitude

$$\begin{aligned} P_1(\vec{r}) &= \epsilon_o a_i d_{ijk} a_j a_k E_2(\vec{r}) E_1^*(\vec{r}) e^{i(\vec{k}_{2\omega} - 2\vec{k}_\omega)\cdot\vec{r}} \\ &= d_{eff} E_2(\vec{r}) E_1^*(\vec{r}) e^{i\Delta\vec{k}\cdot\vec{r}} \,. \end{aligned} \tag{57}$$

Here we see that the fundamental field is re-generated by the SH field. Following the steps leading up to Eq.55 we find the differential equation

$$\frac{dE_1(z)}{dz} = i\kappa_\omega E_2(z) E_1(z) e^{i\Delta k z} \,. \tag{58}$$

Equations 55 and 58 constitute a set of coupled, nonlinear, differential equations which can only be solved exactly using advanced methods. Armstrong et al. [14–17] found the solution for the second harmonic intensity for the special case of zero initial harmonic intensity to be given by

$$I_2(L) = I_1(0)\ \nu_b^2\ \mathrm{sn}\left(\frac{\Gamma L}{\nu_b} \mid \nu_b^4\right) \tag{59}$$

where sn is a Jacobian elliptic function [18] with the following definition of constants:

$$\frac{1}{\nu_b} = \frac{\Delta s}{4} + \sqrt{1 + \left(\frac{\Delta s}{4}\right)^2} \tag{60}$$

where

$$\begin{aligned} \Delta s &= \Delta k / \Gamma \,, \\ \Gamma &= \kappa_\omega \mid E_1(0) \mid . \end{aligned} \tag{61}$$

The sign of the square root in Eq.60 is chosen such that $\nu_b^2 \leq 1$.

The familiar solutions to the coupled equations for zero wave vector mismatch and for no fundamental depletion [11,20,21], are special cases of the above solution. First, for zero wave vector mismatch, $\Delta k = 0$, $\Delta s = 0$ and $\nu_b = 1$. Using the identity $\mathrm{sn}(u \mid 1) = \tanh(u)$, Eq.59 becomes

$$I_2^{(\Delta k=0)}(L) = I_1(0) \tanh^2(\Gamma L). \tag{62}$$

The conservation of energy requires that

$$I_2(L) + I_1(L) = I_1(0) \tag{63}$$

Using this relation along with the trigonometric identity $\tanh^2 + \mathrm{sech}^2 = 1$ we find the fundamental field intensity in this limit to be

$$I_1(L) = I_1(0) \, \mathrm{sech}^2(\Gamma L). \tag{64}$$

Figures 1 and 2

show the intensity build-up and depletion of the second harmonic and fundamental waves, respectively. In theory, SHG should proceed towards 100% conversion efficiency for plane wave interactions. In practice, however, Gaussian intensity laser beams are used instead of plane waves and peak power conversion efficiencies are limited to near 60%.

When depletion of the fundamental wave is small, we have $\Delta s \gg 1$ except near $\Delta k = 0$ where the weak pump limit of Eq.62 applies. For $\Delta s \gg 1$, $\nu_b \simeq \frac{2}{\Delta s} \simeq 0$. Using $\mathrm{sn}(u \mid 0) \simeq \sin(u)$, Eq.59 becomes

$$I_2^{(small)}(L) = I_1(0) \; (\Gamma L)^2 \, \mathrm{sinc}^2 \left(\frac{\Delta k L}{2} \right). \tag{65}$$

According to Eq.65, a prerequisite for efficient SHG is that $\Delta k = 0$. If $\Delta k \neq 0$, the second harmonic wave generated at some plane z_1, having propagated to some other plane z_2. This results in the interference described by the factor $\mathrm{sinc}^2(\frac{\Delta k}{2})$ in Eq.65. Two adjacent peaks of this spatial interference pattern are separated by the so-called 'coherence length' given by

$$l_c = \frac{2\pi}{\Delta k} = \frac{2\pi}{k_{2\omega} - 2k_\omega}. \tag{66}$$

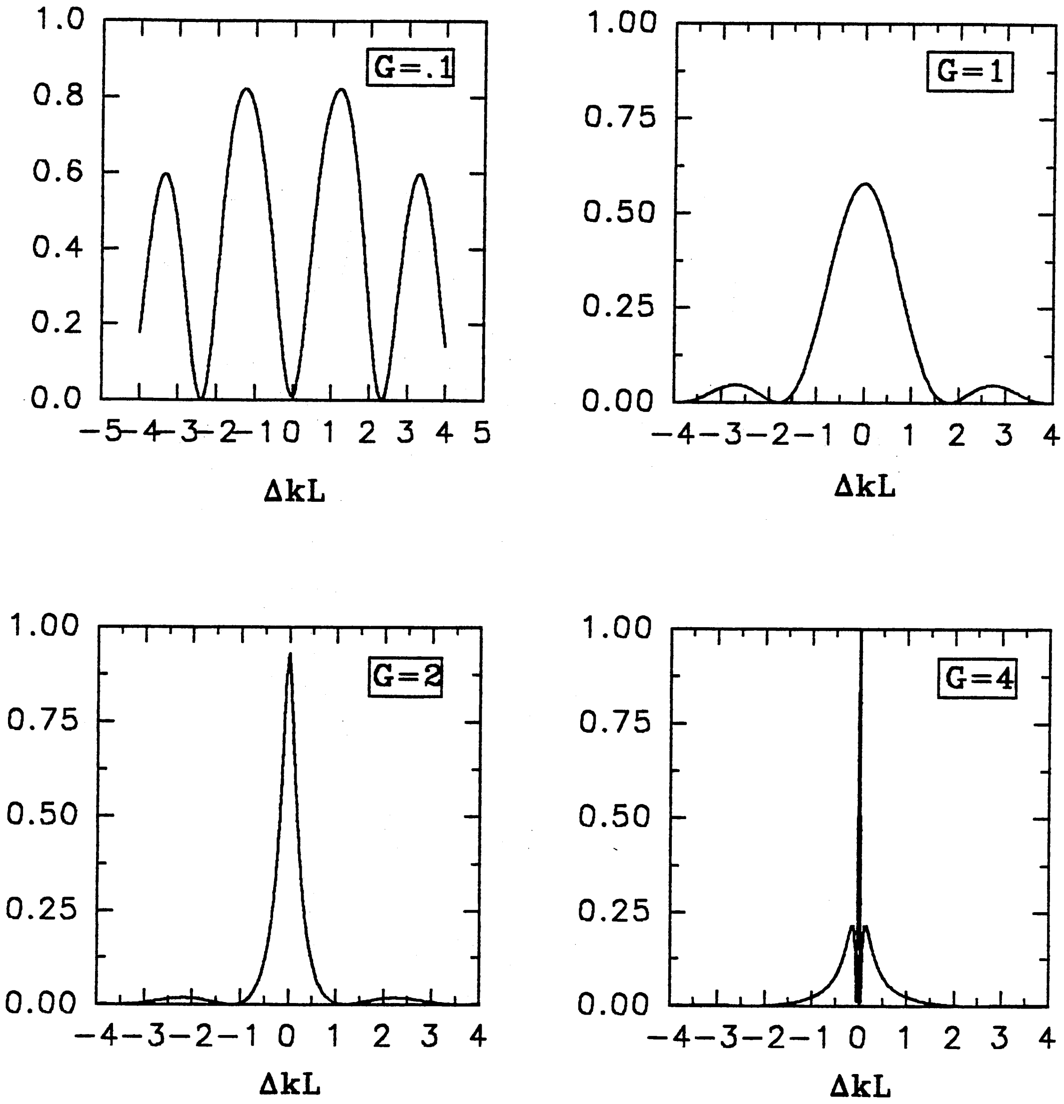

Figure 1. These series of graphs show the SHG intensity output pattern versus phase mismatch for various values of G, the gain coefficient. The first graph shows the intensity pattern in the small gain (or length) limit. This pattern is commonly refered to as 'Maker' fringes which were first observed by Terhune in 1962. [19]. This pattern is normally obtained in samples with interaction lengths smaller than the coherence length, l_c. The fringes correspond to effective interaction lengths which are intergral multiples of l_c.The second pattern is the most commonly observed pattern in SHG crystals. The last two graphs display how the pattern becomes spatially condensed in the high gain limit. As the gain increases the central peak reachs unity, which corresponds to a unit conversion efficiency.

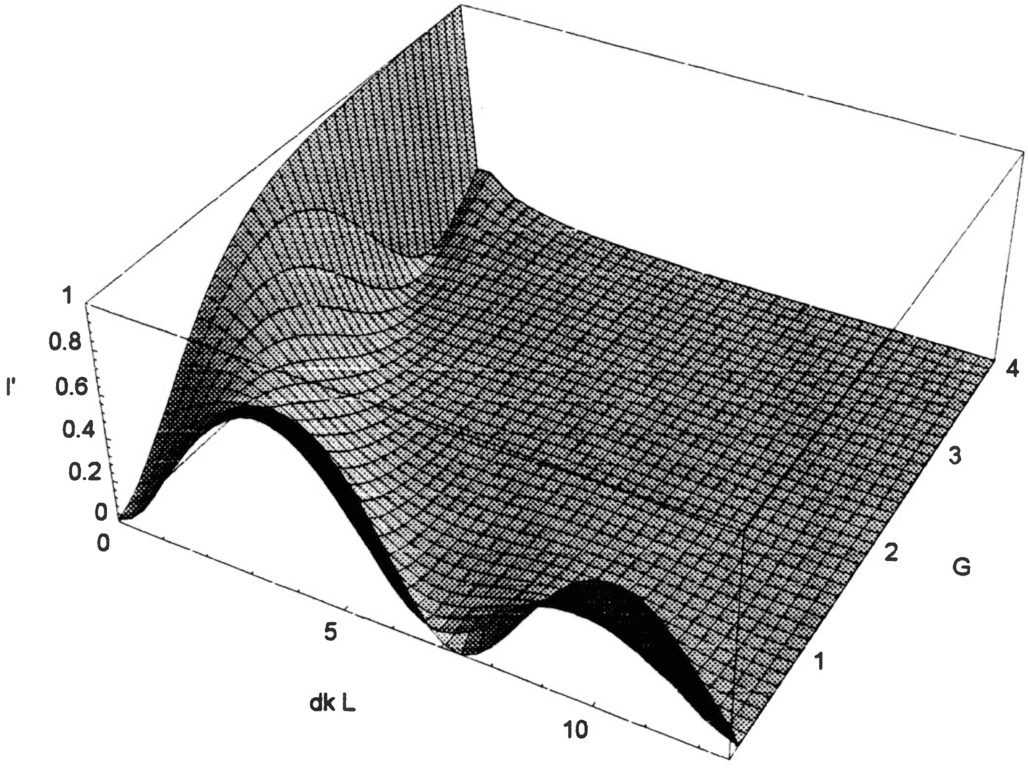

Figure 2. This figure shows the SH output intensity as a function of the gain coefficient, G and the phase mismatch, ΔkL. The growth and depletion of the SH intensiy for various values of the phase mismatch can easily be seen in this figure.

The coherence length l_c is thus a measure of the maximum crystal length, useful for the production of second harmonic power. Under ordinary circumstances, it may be no longer than 10^{-2}cm. This is because the index of refraction n_ω normally increases with ω so Δk is given by

$$\begin{aligned} \Delta k &= k_{2\omega} - 2k_\omega \\ &= \tfrac{2\omega}{c}\left(n_{2\omega} - n_\omega\right) \end{aligned} \tag{67}$$

where we used the relation $k_\omega = \frac{\omega n_\omega}{c}$. The coherence length is thus

$$\begin{aligned} l_c &= \frac{\pi c}{\omega(n_{2\omega} - n_\omega)} \\ &= \frac{\lambda}{2(n_{2\omega} - n_\omega)} \end{aligned} \tag{68}$$

where λ is the free-space wavelength of the fundamental beam. If we take a typical value of $\lambda = 1\mu$m and $n_{2\omega} - n_\omega \simeq 10^{-2}$, we obtain $l_c \simeq 100\mu$m. An increase of l_c from 100μm to 2cm for example, according to Eq.66, would result in an increase of the second harmonic intensity by a factor of 4×10^4! Utilizing a naturally birefringent nonlinear media, in theory, would allow the possibility of matching the index of refraction of the fundamental n_ω to that of the second harmonic $n_{2\omega}$. Under these fortuitous conditions the coherence length would tend towards infinity. This could result in tremendously efficient second harmonic output intensities. This ‘phase-matching’ technique will be described and applied to specific crystals in a future section of this thesis.

CHAPTER IV

OPTICAL PARAMETRIC OSCILLATORS

Introduction

The optical parametric oscillator (OPO), first demonstrated in 1965 by Giordmaine and Miller [22], like SHG is a second order of nonlinear optical phenomena. However, in the case of the OPO, there are two output waves, which can be simultaneously tuned. The OPO is closely analogous to the parametric amplifier commonly used at microwave frequencies to obtain low-noise amplification. Although low range amplification at optical frequencies is possible, most emphasis has been placed on the use of the parametric gain to produce oscillation rather than amplification.

Theory

Parametric or variable-parameter interactions in general can involve three or more waves. However, to remain within the context of our experiments, we will discuss three wave interactions only. The basic interaction to be considered here is one in which a high-frequency electromagnetic wave, called the pump, interacts with a pair of lower frequency electromagnetic fields, called the signal and idler, amplifying them. If feedback is provided and the gain exceeds the losses the oscillation occurs resulting in the generation of signal and idler radiation. By varying parameters associated with the interaction, the signal and idler frequencies can be changed resulting in a tunable source of radiation.

Parametric Amplification

We will begin by first discussing the parametric process responsible for creating the oscillation in the cavity [23–25,14,26–28]. The theoretical description of this parametric process follows that of SHG. We begin by first finding a set of three coupled differential equations, one for each of the interacting waves. The driving polarizations for the three waves can be found by substituting $\omega_3 = \omega_p$, $\omega_2 = \omega_s$ and $\omega_1 = \omega_i$ (where p, s and i denote pump, signal and idler) into Eq.30 which yields a set of second order nonlinear driving polarizations, given by

$$\begin{aligned} P_p(\vec{r}) &= d_{eff} E_s(\vec{r}) E_i(\vec{r}) e^{i\left(\vec{k}_s+\vec{k}_i-\vec{k}_p\right)\cdot\vec{r}} \\ P_s(\vec{r}) &= d_{eff} E_p(\vec{r}) E_i^*(\vec{r}) e^{i\left(\vec{k}_p-\vec{k}_s-\vec{k}_i\right)\cdot\vec{r}} \\ P_i(\vec{r}) &= d_{eff} E_p(\vec{r}) E_s^*(\vec{r}) e^{i\left(\vec{k}_p-\vec{k}_s-\vec{k}_i\right)\cdot\vec{r}} \end{aligned} \tag{69}$$

where we have denoted $E_p(\vec{r})$, $E_s(\vec{r})$ and $E_i(\vec{r})$ as the pump, signal and idler fields, respectively.

Substituting these polarizations into Eq.47, assuming loss less media (i.e. $\alpha_p = \alpha_s = \alpha_i = 0$) we find for $\vec{r} = z\ \hat{z}$ the set of coupled equations

$$\frac{dE_p^*(z)}{dz} = -i\kappa_p E_s^*(z) E_i^*(z)\ e^{i\Delta k\, z} \tag{70}$$

$$\frac{dE_s(z)}{dz} = i\kappa_s E_p(z) E_i^*(z)\ e^{i\Delta k\, z} \tag{71}$$

$$\frac{dE_i(z)}{dz} = i\kappa_i E_p(z) E_s^*(z)\ e^{i\Delta k\, z} \tag{72}$$

where, as with SHG, $\Delta k = k_p - k_s - k_i$, and $\kappa_\beta = \frac{\omega_\beta d_{eff}}{n(\omega_\beta)c}$.

Multiplying these equations successively by $-\left(\frac{n_p e\, \epsilon_o}{2}\right)\frac{E_p}{\omega_p}$, $\left(\frac{n_s c \epsilon_o}{2}\right)\frac{E_s^*}{\omega_s}$ and $\left(\frac{n_i c \epsilon_o}{2}\right)\frac{E_i^*}{\omega_i}$ we find

$$\begin{aligned} -\left(\frac{n_p c\epsilon_o}{2}\right)\frac{E_p(z)}{\omega_p}\frac{dE_p^*(z)}{dz} &= \frac{i}{4}E_p(z)E_s^*(z)E_i^*(z)\, e^{i\Delta k\, z} \\ \left(\frac{n_s c\epsilon_o}{2}\right)\frac{E_s^*(z)}{\omega_s}\frac{dE_s(z)}{dz} &= \frac{i}{4}E_p(z)E_s^*(z)E_i^*(z)\, e^{i\Delta k\, z} \\ \left(\frac{n_i c\epsilon_o}{2}\right)\frac{E_i^*(z)}{\omega_i}\frac{dE_i(z)}{dz} &= \frac{i}{4}E_p(z)E_s^*(z)E_i^*(z)\, e^{i\Delta k\, z}. \end{aligned}$$

Recognizing that the right-hand side of each equation is equivalent, we find, using the relation $\frac{dI}{dz} = \frac{d}{dz}(\frac{n\,c\epsilon_o}{2}) \mid E \mid^2 = n\,c\epsilon_o E\,\frac{dE^*}{dz}$, the Manley-Rowe relation [29]

$$-\frac{1}{\omega_p}\frac{dI_p}{dz} = \frac{1}{\omega_s}\frac{dI_s}{dz} = \frac{1}{\omega_i}\frac{dI_i}{dz} \tag{73}$$

which is a form of photon conservation. Simply stated: parametric generation splits one photon into two photons which satisfy conservation of energy at every point in the nonlinear crystal.

We now proceed to solve the set of coupled equations, viz. Eqs.70, 71 and 72. Assuming minimal pump depletion from the onset, i.e. $\frac{dE_p(z)}{dz} = 0$ or $E_p(z) = E_p\,e^{i\varphi_p}$ where φ_p is the initial phase of the pump wave, the set of three coupled equations reduce to a set of two coupled equations given by

$$\frac{dE_s(z)}{dz} = i\kappa_s E_p E_i^*(z)\,e^{i(\Delta k\,z+\varphi_p)} \tag{74}$$

$$\frac{dE_i(z)}{dz} = i\kappa_s E_p E_s^*(z)\,e^{i(\Delta k\,z+\varphi_p)}. \tag{75}$$

A little forethought leads to the conclusion that the solutions of these equations contain both a gain term $e^{\Gamma' z}$and an oscillatory term $e^{i\frac{\Delta k\,z}{2}}$. That is, the assumed solutions will be of the form

$$E_s^*(z) = E_s^*\,e^{\left(\Gamma' - i\frac{\Delta k}{2}\right)z} \tag{76}$$

$$E_i(z) = E_i\,e^{\left(\Gamma' - i\frac{\Delta k}{2}\right)z}. \tag{77}$$

where the complex conjugate of Eq.71 will be used. Substituting these assumed solutions into Eqs.74 and 75 we find

$$E_s^* = -\frac{i\kappa_s E_p^* E_i e^{-i\varphi_p}}{\left(\Gamma' - i\frac{\Delta k}{2}\right)} \tag{78}$$

$$E_i = \frac{i\kappa_i E_p E_s^* e^{i\varphi_p}}{\left(\Gamma' + i\frac{\Delta k}{2}\right)}. \tag{79}$$

Solving Eqs.78 and 79 simultaneously yields the characteristic equation

$$\left(\Gamma' - i\frac{\Delta k}{2}\right)\left(\Gamma' + i\frac{\Delta k}{2}\right) = \kappa_i\kappa_s\left|E_p\right|^2. \tag{80}$$

The roots of this equation are found to be

$$\Gamma'^2 = \frac{\omega_i \omega_s d_{eff}^2 \left|E_p\right|^2}{n_i n_s c^2} - \frac{\Delta k^2}{4}. \tag{81}$$

Recognizing the first factor in Eq. 81 as being the SHG conversion efficiency in Eq.61 where $\omega_i = \omega_s = \omega$, i.e.

$$\Gamma^2 = \frac{\omega_i \omega_s d_{eff}^2 \left|E_p\right|^2}{n_i n_s c^2} \tag{82}$$

we find the reduced gain constant g, as the roots

$$\begin{aligned} \Gamma' &= \pm\sqrt{\Gamma^2 - \tfrac{\Delta k^2}{4}} \\ &= \pm g\,. \end{aligned} \tag{83}$$

The general solutions to the signal and idler fields will therefore be in the form

$$E_s^*(z) = E_{s_+}^* e^{g\,z} + E_{s_-}^* e^{-g\,z} \tag{84}$$

$$E_i(z) = E_{i_+} e^{g\,z} + E_{i_-} e^{-g\,z} \tag{85}$$

where the coefficients $E_{s_\pm}$ and $E_{i_\pm}$ are determined by the boundary conditions at $z = 0$. If we assume that at $z = 0$ the signal and idler have values $E_{so} e^{i\varphi_s}$ and $E_{io} e^{i\varphi_i}$, where time dependent factors $e^{i\omega_{s,i}t}$ have been dropped, then all the phase information will be included in φ_s and φ_i. Hence E_{so} and E_{io} will be real constants. The surrounding black body radiation is assumed to be the source of the initial signal and idler wave. In the case of the OPO, quantum vacuum fluctuations give rise to the initial signal and idler cavity modes. Using the above boundary conditions in Eqs.84 and 85 we find the relations

$$E_{so}^* e^{-i\varphi_s} = E_{s_+}^* + E_{s_-}^* \tag{86}$$

$$E_{io} e^{i\varphi_i} = E_{i_+} + E_{i_-}\,. \tag{87}$$

Substituting Eq.78 into Eq. 86 and adding $\left(g - i\frac{\Delta k}{2}\right)^{-1}$ times Eq.87 we find

$$E_{i_-} = -\frac{i\Gamma}{2g}\sqrt{\frac{\omega_i n_s}{\omega_s n_i}} E_{so}^* e^{i(\varphi_p - \varphi_s)} + \frac{\left(g + i\frac{\Delta k}{2}\right)}{2g} E_{io} e^{i\varphi_i} \tag{88}$$

where we have used $\kappa_i E_p = \sqrt{\frac{\omega_i n_s}{\omega_s n_i}}\Gamma$. Likewise, adding $-\left(g + i\frac{\Delta k}{2}\right)$ times Eq.87 we find

$$E_{i_+} = \frac{i\Gamma}{2g}\sqrt{\frac{\omega_i n_s}{\omega_s n_i}}E^*_{so}e^{i(\varphi_p - \varphi_s)} + \frac{\left(g - i\frac{\Delta k}{2}\right)}{2g}E_{io}e^{i\varphi_i}\,. \tag{89}$$

The signal fields, $E_{s\pm}$ can now be found by substituting Eqs.88 and 89 into Eq.78 which yields

$$E^*_{s_+} = \frac{\left(g + i\frac{\Delta k}{2}\right)}{2g}E^*_{so}e^{-i\varphi_s} - \frac{i\Gamma}{2g}\sqrt{\frac{\omega_s n_i}{\omega_i n_s}}E_{io}e^{-i(\varphi_p - \varphi_i)} \tag{90}$$

$$E^*_{s_+} = \frac{\left(g - i\frac{\Delta k}{2}\right)}{2g}E^*_{so}e^{-i\varphi_s} + \frac{i\Gamma}{2g}\sqrt{\frac{\omega_s n_i}{\omega_i n_s}}E_{io}e^{-i(\varphi_p - \varphi_i)}. \tag{91}$$

These expressions can be simplified by utilizing the Manley-Rowe relation in Eq.73 to eliminate the initial idler field, E_{io} in terms of the initial signal field, E_{so}. That is,

$$E_{io} = r\sqrt{\frac{\omega_i n_s}{\omega_s n_i}}E_{so}. \tag{92}$$

where $r = 1$ corresponds to the ratio satisfying the Manly-Rowe limit given in Eq.73. In general, r can take on any positive value, however, as a convention we will define the signal field as the field containing the larger number of photons, hence $0 \leq | r | \leq 1$. Using this definition Eqs.88, 89, 90 and 91 become

$$E_{i_-} = \frac{E_{so}e^{i\varphi_i}}{2g}\sqrt{\frac{n_s\omega_i}{n_i\omega_s}}\left\{\left(g + i\frac{\Delta k}{2}\right)r - i\Gamma e^{i\varphi}\right\} \tag{93}$$

$$E_{i_+} = \frac{E_{so}e^{i\varphi_i}}{2g}\sqrt{\frac{n_s\omega_i}{n_i\omega_s}}\left\{\left(g - i\frac{\Delta k}{2}\right)r + i\Gamma e^{i\varphi}\right\} \tag{94}$$

$$E^*_{s_+} = \frac{E^*_{so}e^{-i\varphi_s}}{2g}\left\{\left(g + i\frac{\Delta k}{2}\right)r - i\Gamma e^{-i\varphi}\right\} \tag{95}$$

$$E^*_{s_-} = \frac{E^*_{so}e^{-i\varphi_s}}{2g}\left\{\left(g - i\frac{\Delta k}{2}\right)r + i\Gamma e^{-i\varphi}\right\} \tag{96}$$

where φ is defined as the relative initial phase between the three waves,

$$\varphi = \varphi_p - \varphi_s - \varphi_i. \tag{97}$$

Substituting Eqs.93 and 96 into Eqs.84 and 85 we find the signal and idler fields to be given by

$$E_s^*(z) = \frac{E_{so}e^{-i\varphi_s}}{g} \times$$
$$\left\{g \cosh(g\,z) + \Gamma r \sin\varphi \sinh(g\,z) + i\left[\frac{\Delta k}{2} - \Gamma r \cos\varphi\right] \sinh(g\,z)\right\} \tag{98}$$

and

$$E_i(z) = \frac{E_{so}e^{i\varphi_i}}{g}\sqrt{\frac{n_s\omega_i}{n_i\omega_s}} \times$$
$$\left\{g\,r \cosh(g\,z) + \Gamma \sin\varphi \sinh(g\,z) - i\left[\frac{\Delta k}{2} - \Gamma r \cos\varphi\right] \sinh(g\,z)\right\} \tag{99}$$

From these fields we can calculate the spatial dependence of the signal and idler intensities. Using the relationship $I = \frac{ncE_o}{2} \mid E \mid^2$, we find the intensities

$$I_s(z) = I_s(0)\ \frac{1}{g^2} \times$$
$$\left\{[g \cosh(g\,z) + \Gamma r \sin\varphi\ \sinh(g\,z)]^2 + \left[\frac{\Delta k}{2} - \Gamma r \cos\varphi\right]^2 \sinh^2(g\,z)\right\} \tag{100}$$

and

$$I_i(z) = I_s(0)\ \frac{1}{g^2} \times$$
$$\left\{[g \cosh(g\,z) + \Gamma r \sin\varphi\ \sinh(g\,z)]^2 + \left[\frac{\Delta k}{2} - \Gamma r \cos\varphi\right]^2 \sinh^2(g\,z)\right\} \tag{101}$$

these are the central results of this section.

From these results it is evident that the relative initial phase φ, is important in determining the rate of growth (or decay) of the two waves. In the case where the signal, idler and pump are all simultaneously injected by sources external to the nonlinear medium, then the phase φ will be uniquely determined. However, if only the pump and signal (or pump and idler) are injected, or if only the pump is injected and the signal and idler are required to grow from vacuum fluctuations, then one expects an optimum phase for maximum growth of the signal and idler and another corresponding to maximum attenuation.

In a practical case, we are interested in finite interaction lengths. Hence, we take the medium in which the waves interact to have length L, and maximize (or minimize) the intensity I_s with respect to the arbitrary phase, φ. It is equivalent to maximize either I_s or I_i since it is known from the Manley-Rowe relations that, in terms of the photons, both signal and idler grow (or attenuate) by the same amount. Thus, setting the derivative of I_s in Eq.101 equal to zero we find the relationship for the optimum phase to be

$$\frac{\cos\varphi}{\sin\varphi} = -\,\frac{\Delta k}{2g}\,\frac{\sinh(g\,L)}{\cosh(g\,L)} \tag{102}$$

which can be rearranged to give the condition,

$$\cos\varphi = \pm\,\frac{\sinh(g\,L)}{\sqrt{1+\left(\frac{\Gamma}{g}\right)^2\sinh^2(g\,L)}} \tag{103}$$

where we have used $\left(\frac{\Gamma}{g}\right)^2 = 1+\left(\frac{\Delta k}{2g}\right)^2$ from Eq.83.

For any value of g and Δk there are two values of the phase φ which satisfy Eq.103; one value gives rise to growth and the other to decay of both the signal and idler waves. We can find the signal and idler intensities for the optimum phase condition by substituting Eq.103 into Eqs.100 and 101. Collecting terms we find the optimum signal and idler intensities to be

$$I_s^{(opt)}(L) = I_s(0)\left\{\sqrt{1+\left(\frac{\Gamma}{g}\right)^2\sinh^2(g\,L)}\;\mp\;r\left(\frac{\Gamma}{g}\right)\sinh(g\,L)\right\}^2 \tag{104}$$

and

$$I_i^{(opt)}(L) = \left(\frac{\omega_i}{\omega_s}\right)I_s(0)\left\{r\sqrt{1+\left(\frac{\Gamma}{g}\right)^2\sinh^2(g\,L)}\;\mp\;\left(\frac{\Gamma}{g}\right)\sinh(g\,L)\right\}^2 \tag{105}$$

where the $\mp$ sign corresponds to the choice of sign $\pm$ of $\cos\varphi$ in Eq.103.

We first consider the amplification of the signal when no idler is injected (i.e. $r = 0$). From Eq.105 we find for $r = 0$ the intensities at $z = L$ to be given by

$$\begin{aligned} I_s^{(r=0)}(L) &= I_s(0)\left\{1+(\Gamma L)^2\left(\tfrac{\sinh(\Gamma L)}{\Gamma L}\right)^2\right\} \\ I_i^{(r=0)}(L) &= \left(\tfrac{\omega_i}{\omega_s}\right)I_s(0)\left\{1+(\Gamma L)^2\left(\tfrac{\sinh(\Gamma L)}{\Gamma L}\right)^2\right\}. \end{aligned} \tag{106}$$

These intensities are shown in Fig.3 as a function of momentum mismatch. As with SHG the maximum gain is obtained when the phase matching condition is obeyed, i.e. $\Delta k = 0$. Using the relation given in Eq.83, i.e.

$$g^2 = \Gamma^2 - \left(\frac{\Delta k}{2}\right)^2 \tag{107}$$

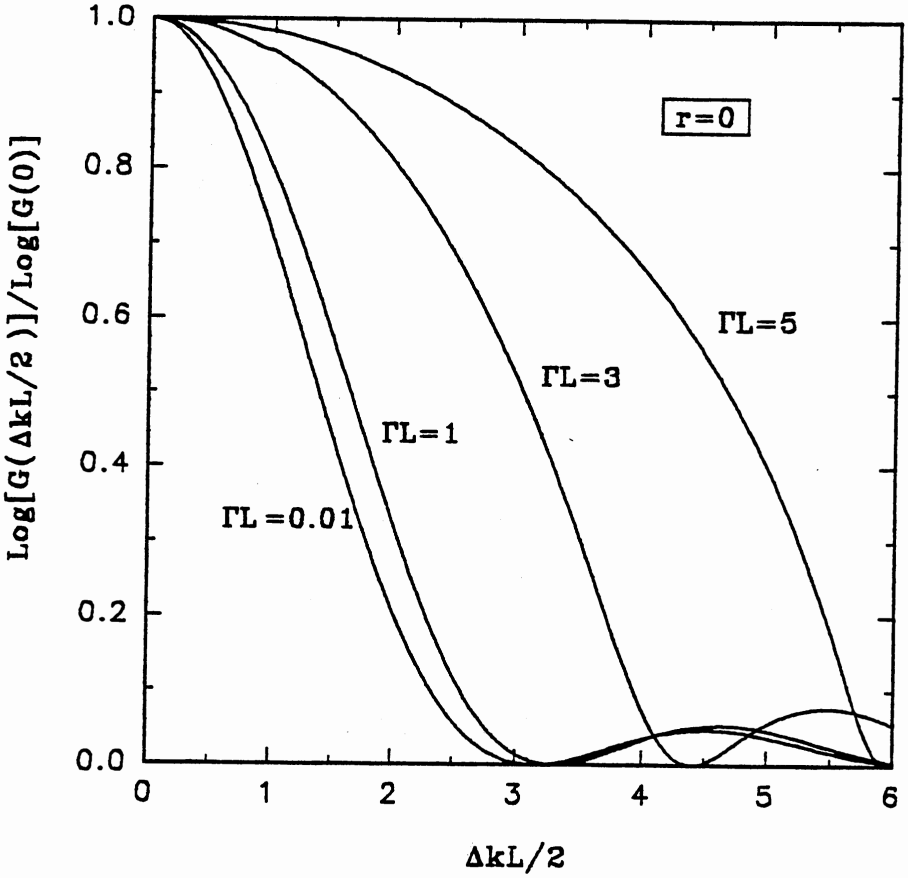

Figure 3. Logarithmic amplifier gain (r=0) as a function of momentum mismatch $\frac{1}{2}\Delta kL$ for various values of the gain constant ΓL. After Smith [26].

we find, for $r = 0$, the phase matched intensities

$$\begin{aligned} I_s^{(r=\Delta k=0)} &= I_s(0)\cosh^2(g\,L) \\ I_i^{(r=\Delta k=0)} &= \left(\tfrac{\omega_i}{\omega_s}\right) I_s(0)\,\sinh^2(g\,L). \end{aligned} \tag{108}$$

From this analysis we see that a finite gain does exist for both the signal and idler waves even when an initial idler wave does not exist.

OPO

The parametric interaction is capable of providing gain as discussed above. In order to obtain oscillation, some form of feedback is required. In OPOs, this is accomplished by enclosing the nonlinear material in an optical resonator similar to that used in a laser. Although there are a number of configurations which OPOs take, there are basically two types. In one, feedback is provided for both signal and idler. This type is called the doubly resonant oscillator (DRO). In the second class, feedback is provided for either the signal or idler but not both. This type of oscillator is referred to as a singly resonant oscillator (SRO). All of the experiments discussed in this thesis are of the DRO variety. Hence, we will only be concerned with DRO in this section.

The expression appropriate for the intensity gain of a DRO–OPO is given by Eq.100 and 101 in the case where there is the arbitrary relative phase φ and by Eqs.104 and 105 when the phase is optimized for maximum gain. In an oscillator the question arises as to what relative phase φ should be chosen in Eqs.100 and 101. We can argue that in building up from the noise, an oscillator eventually chooses the phase giving the greatest growth constant. Hence parametric growth will proceed at the optimum phase. Thus Eqs.104 and 105 are appropriate for the OPO. A plot of the general expression for the OPO gain as a function of momentum mismatch is shown in Fig.4 where we have assumed identical losses at the signal and idler, i.e. $r = 1$.

As usual, the maximum gain occurs when the phase matching condition, $\Delta k = 0$, is obeyed. The intensities of the phase-matched signal and idler field is

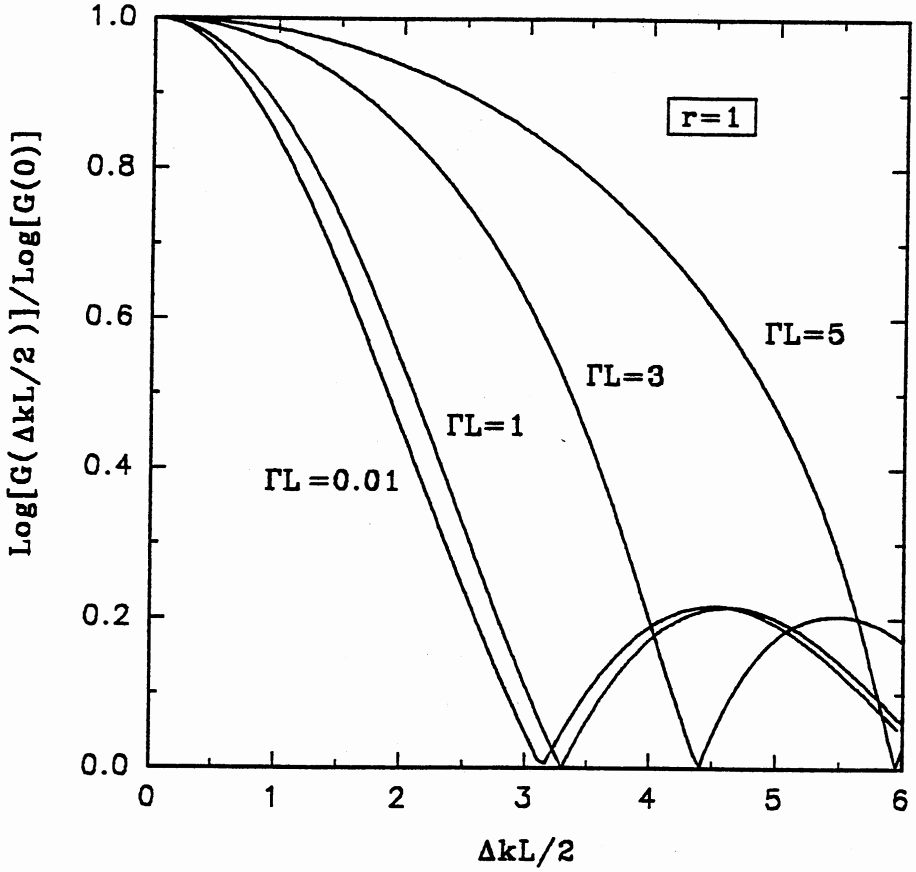

Figure 4. Logarithmic oscillator gain (r=1) as a function of momentum mismatch $\frac{1}{2}\Delta kL$ for various values of the gain constant ΓL. After Smith [26].

therefore given by

$$I_s^{(\Delta k=0)}(L) = I_s(0)\,[\cosh(g\,L) + r\sinh(g\,L)]^2 \tag{109}$$

$$I_i^{(\Delta k=0)}(L) = \left(\frac{\omega_i}{\omega_s}\right) I_s(0)\,[r\cosh(g\,L) + \sinh(g\,L)]^2\,. \tag{110}$$

For the special case of a DRO (i.e. $r = 1$) the intensities display exponential growth, i.e.

$$I_s^{(r=\Delta k=0)}(L) = I_s(0)\,e^{2gL} \tag{111}$$

$$I_s^{(r=\Delta k=0)}(L) = \left(\frac{\omega_i}{\omega_s}\right) I_s(0)\,e^{2gL}. \tag{112}$$

Threshold Conditions

The threshold condition is defined as being the condition in which the round trip gain experienced by the resonant waves equal the round trip losses. Below threshold there exists a small amount of spontaneous parametric emission. Whereas, above threshold the signal and idler fields experience a net round trip gain which can grow to magnitudes comparable to that of the pump, at which point useful output is obtained.

For the DRO, the threshold condition is found by requiring that the gains of the signal and idler compensate for each of their round trip losses; α_s and α_i, respectively. The condition can be evaluated analytically by the requirement that the round trip intensity be equivalent to the initial intensity. It is obvious from the diagram in Fig.5 shown below, that the threshold condition implies the relations

$$I_{os,i} = G_{s,i} I_{os,i} - \alpha_{s,i} G_{s,i} I_{os,i} \tag{113}$$

which require a net gain coefficient of

$$G_{s,i} = \frac{1}{1-\alpha_{s,i}}. \tag{114}$$

The optimum intensity gain for the signal and idler are derived directly from Eqs.104 and 105 to be given by

$$G_s = \frac{I_s(L)}{I_s(0)} = \left\{\sqrt{1+\left(\frac{\Gamma}{g}\right)^2 \sinh^2(g\,L)} \;+\; r\left(\frac{\Gamma}{g}\right)\sinh(g\,L)\right\}^2 \tag{115}$$

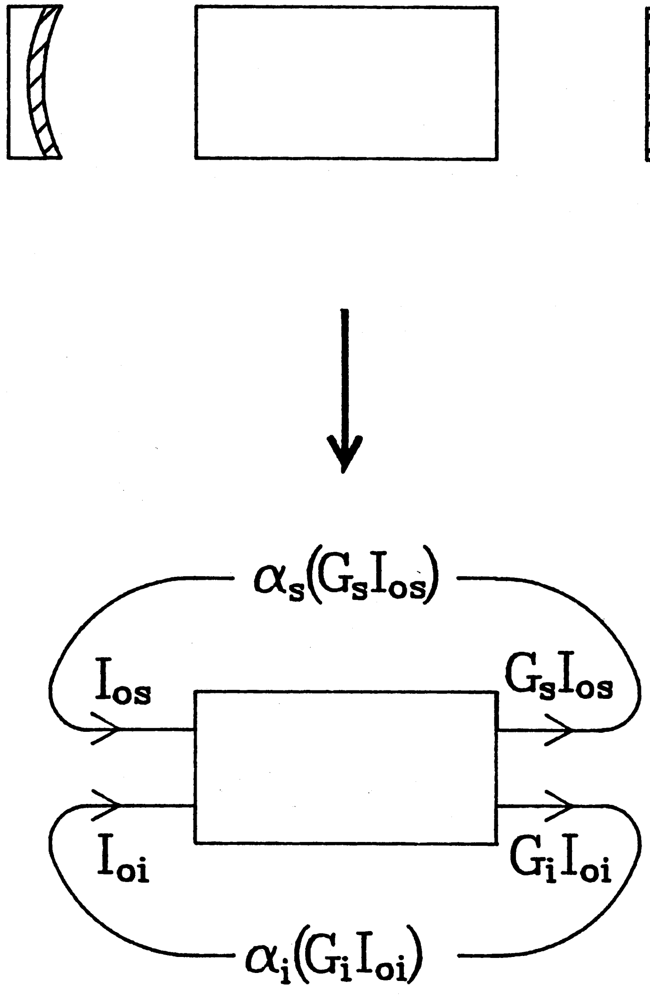

Figure 5. The threshold condition is determined by requiring that the round trip gain, G overcome the round trip loss, α such that the round trip intensity be equivalent to initial intensity.

and

$$G_i = \frac{I_i(L)}{I_i(0)} = \frac{1}{r^2}\left\{ r\sqrt{1+\left(\frac{\Gamma}{g}\right)^2 \sinh^2(g\,L)} \;+\; \left(\frac{\Gamma}{g}\right)\sinh(g\,L)\right\}^2 . \tag{116}$$

These equations can be rewritten in the form

$$\begin{aligned} \sqrt{G_s} &= \sqrt{1+x^2} + r\,x \\ \sqrt{G_i} &= \sqrt{1+x^2} + \tfrac{x}{r} \end{aligned} \tag{117}$$

where $x = (\frac{\Gamma}{g})^2 \sinh^2(g\,L) = (\Gamma L)^2 \frac{\sinh^2(gL)}{(g\,L)^2}$. Solving these equations simultaneously we find

$$\sqrt{1+x^2} = \frac{\sqrt{G_i G_s}+1}{\sqrt{G_s}+\sqrt{G_i}} \tag{118}$$

where we have cancelled out the r-dependence. Substituting Eq.118 into Eq.114 and solving for x^2 we find the threshold condition

$$(\Gamma\,L)^2\,\frac{\sinh^2(g\,L)}{(g\,L)^2} = \frac{\alpha_s\alpha_i}{\left[\sqrt{1-\alpha_i}+\sqrt{1-\alpha_s}\right]^2} . \tag{119}$$

For small gain and losses at both the signal and idler, Eq.119 becomes

$$(\Gamma\,L)^2\,\frac{\sin\left(\frac{\Delta k}{2}L\right)}{\left(\frac{\Delta k}{2}L\right)} \simeq \frac{\alpha_s\alpha_i}{4} \tag{120}$$

From this equation, it is easy to see that the minimum threshold gain is obtained when the phase-matching condition $\Delta k = 0$ is satisfied, i.e.

$$\Gamma_{\min} \simeq \frac{\alpha_s\alpha_i}{4L^2} \tag{121}$$

which is the minimum gain needed for oscillation to start (in the limit of small losses).

From this analysis we can determine the minimum pump intensity required to reach threshold. Substituting the definition of Γ, given by Eq.82, into Eq.120 and solving for $I_p^{(th)}$, we find

$$I_p^{(th)} = \frac{\alpha_i\alpha_s n_i n_s n_p \epsilon_o c^3}{8\,\omega_o^2(1-\delta^2)\,d_{eff}^2\,L^2}\left[\text{sinc}\left(\frac{\Delta k L}{2}\right)\right]^{-1} \tag{122}$$

where $\omega_o = \frac{1}{2}\omega_p$ is the degenerate operating frequency and δ is a measure of the deviation form the degenerate operating point, i.e. $\omega_s = \omega_o(1+\delta)$ and $\omega_i = \omega_o(1-\delta)$.

CHAPTER V

PHASE MATCHING THEORY

In the previous two sections, it was shown that the conversion efficiencies of both SHG and OPO could be dramatically increased if the phase-matching condition, $\Delta k = 0$, was satisfied. This section will be dedicated to developing the theoretical formalism necessary for the phase matching of three wave interactions in biaxial crystals [19,30–32]. Specific phase matching calculations will also be presented for the biaxial crystals used in this investigation, namely: KTP and KTA.

For interactions involving the coupling of three waves, the conditions of energy and momentum conservation are written as follows:

$$\omega_3 = \omega_1 + \omega_2 \tag{123}$$

and

$$k_3 = k_1 + k_2 + \Delta k. \tag{124}$$

Phase matching is achieved whenever $\Delta k = 0$. Equation 124 can be expressed in terms of the frequencies ω_i and their respective refractive indices n_i via the dispersion relation, $k = \omega/c$ to give

$$\omega_3 n_3 \, \hat{\imath}_3 = \omega_1 n_1 \, \hat{\imath}_1 + \omega_2 n_2 \, \hat{\imath}_2 \tag{125}$$

where $\hat{\imath}$ is the unit vector parallel to $\vec{k}$. The collinear phase matching condition requires all three waves to propagate along the same line, i.e. $\hat{\imath}_1 = \hat{\imath}_2 = \hat{\imath}_3$. Under this condition Eq.125 reduces to the form

$$1 = \frac{\omega_1}{\omega_3}\frac{n_1}{n_3} + \frac{\omega_2}{\omega_3}\frac{n_2}{n_3}. \tag{126}$$

Rewriting Eq.123 in a similar manner we find

$$1 = \frac{\omega_1}{\omega_3} + \frac{\omega_2}{\omega_3}. \tag{127}$$

Phase matching is customarily achieved by utilizing the birefringent and dispersive properties of anisotropic crystals. In biaxial crystals, the allowed polarization directions for a beam with arbitrary polarization, entering the crystal in an arbitrary direction is determined from the following construction.

The index of refraction of a wave traveling in a biaxial crystal, with an arbitrary direction is determined by solving for the roots of Fresnel's equation [33], given by

$$\frac{k_x^2}{\left(\frac{1}{n^2} - \frac{1}{n_x^2}\right)} + \frac{k_y^2}{\left(\frac{1}{n^2} - \frac{1}{n_y^2}\right)} + \frac{k_z^2}{\left(\frac{1}{n^2} - \frac{1}{n_z^2}\right)} = 0 \tag{128}$$

which is an equation for an ellipsoid. In this equation $k_x = k\ \sin(\theta)\ \cos(\varphi)$, $k_y = k\ \sin(\theta)\ \sin(\varphi)$, and $k_z = k\ \cos(\theta)$ are the x, y, and z components of the $\vec{k}$–vector and n_x, n_y, and n_z are the principle axes of the ellipsoid. Since Eq.128 is a quadratic equation, there exists two roots n^{e_1} and n^{e_2} which satisfy this equation. Therefore, a wave of arbitrary polarization, traveling in an arbitrary direction, will be resolved into two components; one traveling with a speed c/n^{e_1}, and another with a speed c/n^{e_2}. If the speed of these two polarization components are different then the state of the polarization is subject to change.

The roots of Eq.128 can be evaluated by rewriting Eq.128 in the form of the quadratic equations. To do this we define the variables $\xi \equiv \frac{1}{n^2}$, $a \equiv \frac{1}{n_x^2}$, $b \equiv \frac{1}{n_y^2}$, and $c \equiv \frac{1}{n_z^2}$. Upon substitution of these variables into Eq.128 we obtain,

$$\frac{k_x^2}{\xi - a} + \frac{k_y^2}{\xi - b} + \frac{k_z^2}{\xi - c} = 0 \tag{129}$$

Multiplying by $(\xi - a)(\xi - b)(\xi - c)$ and collecting terms in like powers of ξ gives

$$\xi^2 - \left[(b+c)k_x^2 + (a+c)k_y^2 + (a+b)k_z^2\right] + \left[b\,c\,k_x^2 + a\,c\,k_y^2 + a\,b\,k_z^2\right] = 0 \tag{130}$$

where we have used the relation $k_x^2 + k_y^2 + k_z^2 = 1$. Defining the constants

$$B = -\left[(b+c)k_x^2 + (a+c)k_y^2 + (a+b)k_z^2\right] \tag{131}$$

and

$$C = b\,c\,k_x^2 + a\,c\,k_y^2 + a\,b\,k_z^2 \tag{132}$$

reduces Eq.130 to the simplified relation

$$\xi^2 + B\xi + C = 0 \tag{133}$$

which has well known roots.

Relating the roots of Eq.133 back to the index of refraction we find the solutions

$$n^{e_1}(\theta,\phi) = \frac{\sqrt{2}}{\sqrt{-B - \sqrt{B^2 - 4C}}} \tag{134}$$

$$n^{e_2}(\theta,\phi) = \frac{\sqrt{2}}{\sqrt{-B + \sqrt{B^2 - 4C}}} \tag{135}$$

where we have chosen the positive roots since the negative roots obviously has no physical significance. These roots are denoted such that n^{e_1} and n^{e_2} represent the indices of refraction of the mutually perpendicular polarization components $\hat{e}_1$ and $\hat{e}_2$.

The directions of the polarization components, $\hat{e}_1$ and $\hat{e}_2$, can be found by examining the geometry of the index ellipsoid described by Eq.128. The cross-section of the ellipsoid, seen by an incident beam of arbitrary polarization, is obviously an ellipse. The semi-major and semi-minor axes of which, are collinear with the $\hat{e}_1$, and $\hat{e}_2$ basis vectors, respectively. Hence, the polarization of the incident beam will be resolved into two components: one along the semi-major axis which will propagate with an index of refraction n^{e_1}, and the other along the semi-minor axis which will propagate with an index of refraction n^{e_2}. There are two directions for which the cross-sections are circular rather than elliptical. A beam traveling in these directions will suffer no change in its state of polarization since, in this case, $n^{e_1} = n^{e_2}$. For this reason these axes are called the 'optic-axes'. The circular cross-sections of the index ellipsoid are shown as curves C_1 and C_2 in Fig.6.

The normals $\hat{N}_1$ and $\hat{N}_2$ are coplanar with the longest and shortest principle axes (n_z and n_x) of the ellipsoid and define the optic axis of the crystal. Let E be

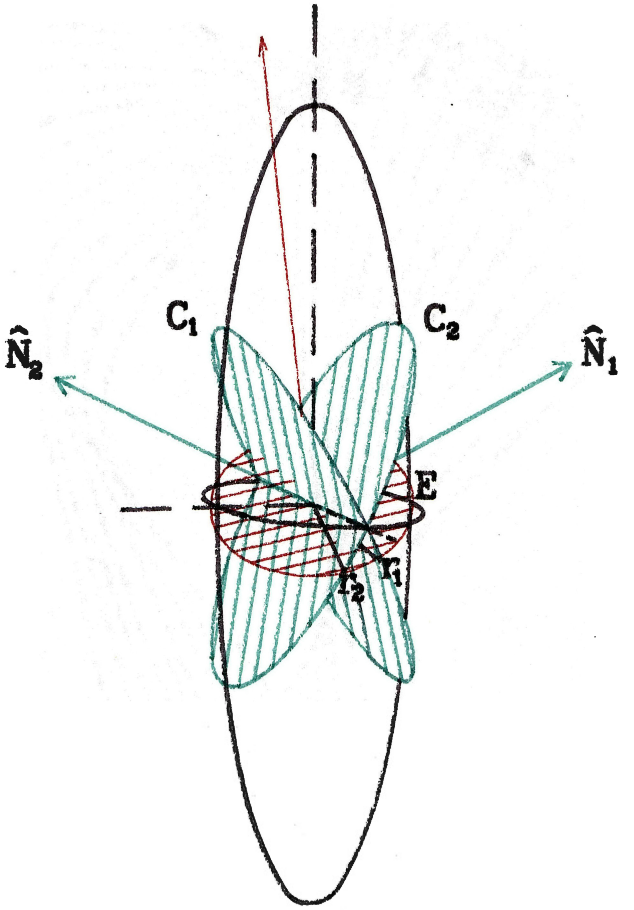

Figure 6. This figure shows the cross-sections of the biaxial index ellipsoid seen by a beam travelling in an arbitrary direction (red) and two beams travelling along the optic axes (green). The beam normals are $\vec{k}$, $\hat{N}_1$ and $\hat{N}_2$, repectively. The arbitrary polarization of the incident beam will be resolved by the set of orthogonal coordinate defined by the bisector of r_1 and r_2, the intersections of the circular sections C_1 and C_2 with the elliptical section E. After Born et al. [33]

the elliptical section through the centers at right angles to an arbitrary unit normal $\hat{k}$; the propagation vector. This plane intersects the circles C_1, C_2 in two radial vectors $\vec{r}_1$, $\vec{r}_2$ which are equal in length and must therefore make equal angles with the principle axis of E (see Fig.6). The required directions of $\hat{e}_1$ is therefore the bisector of the directions $\vec{r}_1$ and $\vec{r}_2$.

The spherical projection of this geometrical construction is shown in Fig.7. In this construction $\hat{N}_1$, $\hat{N}_2$ represent the optic axes which are located at an angle Ω to n_z in the n_z, n_x– plane. As usual, the propagation vector, $\vec{k}$ is located by the polar and azimuthal angles θ and ϕ, respectively. The spherical triangle N_1KN_2 is obtained by drawing the great circles N_1K and N_2K on the sphere. the polarization direction $\hat{e}_1$ is drawn as the perpendicular bisector of the angle N_1KN_2. The angle δ, shown as the angle between $\hat{e}_1$ and ZK at the point K, can be related to the known quantities through the following relationship [32]:

$$\cot 2\delta = \frac{\cot^2\Omega \sin^2\theta - \cos^2\theta \cos^2\phi + \sin^2\phi}{\cos\theta - \sin 2\phi}, \tag{136}$$

where Ω follows the well known relation [33]

$$\cot^2\Omega = \frac{\left[\frac{1}{n_y^2} - \frac{1}{n_z^2}\right]}{\left[\frac{1}{n_x^2} - \frac{1}{n_y^2}\right]}. \tag{137}$$

Examining the results of Eqs.134 and 135 in conjunction with the phase matching conditions of Eqs.126 and 127 we find the following two ways in which phase matching can be achieved. From Eq.127 we note that the ratios ω_1/ω_2, ω_2/ω_3 obey the following conditions

$$\frac{\omega_1}{\omega_3}, \frac{\omega_2}{\omega_3} < 1. \tag{138}$$

Therefore, in order to maintain Eq.126, one of the following conditions must be met:

$$\frac{n_1}{n_3}, \frac{n_2}{n_3} > 1 \Longrightarrow n_1,\ n_2 > n_3 \tag{139}$$

$$\frac{n_1}{n_3} < 1,\ \frac{n_2}{n_3} > 1 \Longrightarrow n_1 < n_3,\ n_2 > n_3 \tag{140}$$

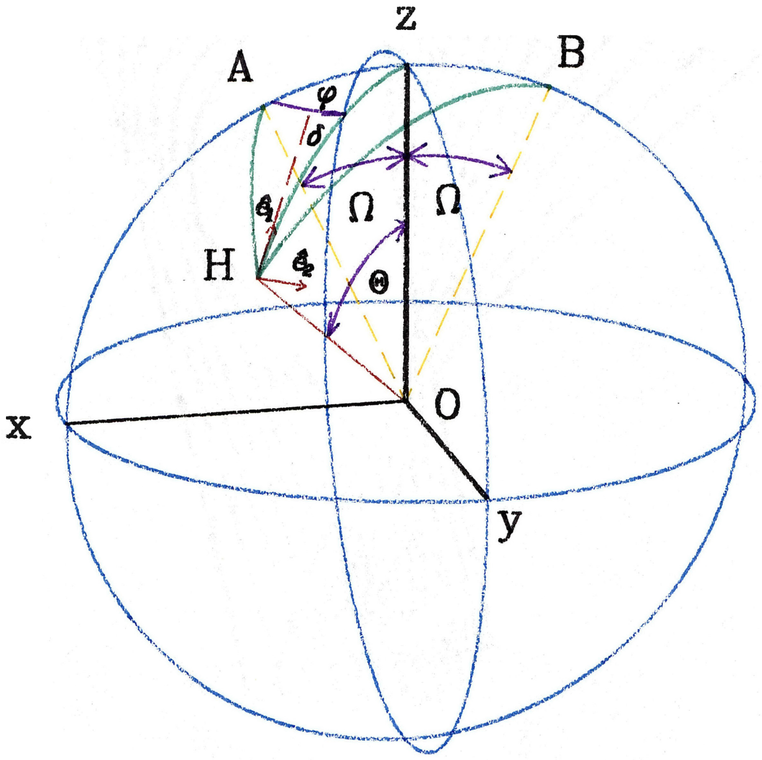

Figure 7. This figure shows the spherical projection for the geometry of an arbitrarily travelling beam, making angles θ and ϕ to the z-axis, in a biaxial crystal. The intersections of the beam and the two optic axes with the sphere are H, A and B. The polarization direction $\hat{e}_1$ makes an angle δ, with the A, B intercept. After Ito et al. [32].

TABLE I

TYPES OF PHASE MATCHING CONDITIONS

Type I	**Type IIa**	**Type IIb**
$\omega_1 : e_1\text{–ray}$	$\omega_1 : e_1\text{–ray}$	$\omega_1 : e_2\text{–ray}$
$\omega_2 : e_1\text{–ray}$	$\omega_2 : e_2\text{–ray}$	$\omega_2 : e_1\text{–ray}$
$\omega_3 : e_2\text{–ray}$	$\omega_3 : e_2\text{–ray}$	$\omega_3 : e_2\text{–ray}$
$n_3^{e_2} = \frac{\omega_1}{\omega_3} n_1^{e_1} + \frac{\omega_2}{\omega_3} n_2^{e_1}$	$n_3^{e_2} = \frac{\omega_1}{\omega_3} n_1^{e_1} + \frac{\omega_2}{\omega_3} n_2^{e_2}$	$n_3^{e_2} = \frac{\omega_1}{\omega_3} n_1^{e_2} + \frac{\omega_2}{\omega_3} n_2^{e_1}$

$$\frac{n_1}{n_3} > 1,\ \frac{n_2}{n_3} < 1 \Longrightarrow n_1 > n_3,\ n_2 < n_3. \tag{141}$$

It was defined in Eq.134 and 135 that $n^{e1} > n^{e2}$. Hence, in order to satisfy Eqs.139, 140 and 141, the following must be true

$$\begin{gathered} n_1,\ n_2 = n^{e_1}(\omega_1),\ n^{e_1}(\omega_2) \\ n_3 = n^{e_2}(\omega_3) \end{gathered} \tag{142}$$

$$\begin{gathered} n_1 = n^{e_2}(\omega_1),\ n_2 = n^{e_1}(\omega_2) \\ n_3 = n^{e_2}(\omega_3) \end{gathered} \tag{143}$$

or

$$\begin{gathered} n_1 = n^{e_1}(\omega_1),\ n_2 = n^{e_2}(\omega_2) \\ n_3 = n^{e_2}(\omega_3) \end{gathered} \tag{144}$$

These three scenarios represent ‘types’ of phase matching and are summarized in Table I.

The procedure for finding the phase matching angles is as follows. One of the three types must first be selected. This choice is arbitrary at first, since at this point, it cannot be determined which type will yield optimum phase matching (i.e. the phase matching condition that yields the highest conversion efficiency). The corresponding roots n^{e1} or n^{e2} must then be substituted into the condition chosen.

For example, under Type I phase matching conditions the following relation would result:

$$\begin{aligned} & \frac{\sqrt{2}}{\sqrt{-B(\omega_3,\theta_m,\phi_m)+\sqrt{B(\omega_3,\theta_m,\phi_m)^2-4C(\omega_3,\theta_m,\phi_m)}}} \\ = & \frac{\sqrt{2}(\omega_1/\omega_3)}{\sqrt{-B(\omega_1,\theta_m,\phi_m)+\sqrt{B(\omega_1,\theta_m,\phi_m)^2-4C(\omega_1,\theta_m,\phi_m)}}} \\ + & \frac{\sqrt{2}(\omega_2/\omega_3)}{\sqrt{-B(\omega_2,\theta_m,\phi_m)+\sqrt{B(\omega_2,\theta_m,\phi_m)^2-4C(\omega_2,\theta_m,\phi_m)}}} \end{aligned} \tag{145}$$

where θ_m and ϕ_m represent the desired solutions.

It should be obvious at this point that an analytical solution for θ_m and ϕ_m does not exist. A procedure for finding the numerical solution to equations of this form must therefore be developed to find the solutions for θ_m and ϕ_m. A computer program was written to solve these equations and has been included as the Appendix.

The frequency dependence of the index of refraction in Eq.145, enters as an implicit frequency dependence of n_x, n_y and n_z— the principal axes of the index ellipsoid. Therefore, we first must know the dispersion relations for the principle axes before we can find solutions to Eq.145. A numerical fit of the dispersion data for a particular material can be fit to Sellemier's theoretical dispersion relation[33], given to second order by

$$n_i^2(\lambda) - 1 = A_1 + \frac{A_2}{\lambda^2 - A_3^2} + A_4\lambda^2 \tag{146}$$

where $n_i = n_x$, n_y, and n_z, the principle axes.

The next step is to determine which set of solutions θ_{m_i}, ϕ_{m_i} which yield optimum phase matching. The favorable set of phase matching angles is the set that maximizes $d_{eff}(\theta_m, \phi_m)$. This is because the conversion efficiency for both SHG and OPO is proportional to $d_{eff}(\theta_m, \phi_m)$. The analytic expression for $d_{eff}(\theta, \phi)$ was shown to be given by

$$d_{eff}(\theta, \phi) = \epsilon_o a_i d_{ijk} a_j a_k \tag{147}$$

where a_i, a_j ,and a_k are direction cosines associated with various fields.

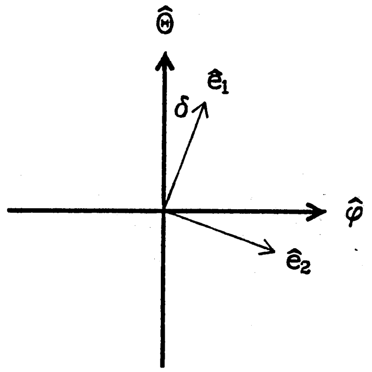

Figure 8. Polarization basis resolved in the spherical coordinate basis.

The direction cosines represent the fraction of the field E^{e_α} used by a particular component of the field, $E_j^{e_\alpha}$. As was shown in ch.III the $j^{\underline{th}}$ component of the electric field can be written as

$$E_j^{e_\alpha}(\omega_l) = a_j^{e_\alpha} E^{e_\alpha}(\omega_l) \tag{148}$$

where the superscript e_α signifies that the E_j electric field component is polarized along the $\hat{e}_\alpha$ polarized vector.

Expressions for these coefficients can be found by resolving the various components into spherical coordinates and then transforming them to the Cartesian coordinate system via a coordinate transformation. The $\hat{e}_1$ and $\hat{e}_2$ polarized waves are shown resolved by the spherical coordinate system in Fig.8. The polarization vectors are resolved into their spherical–polar components below

$$\begin{aligned} \hat{e}_1 &= \cos\delta\,\hat{\theta}\ + \sin\delta\,\hat{\phi} \\ \hat{e}_2 &= -\sin\delta\,\hat{\theta}\ + \cos\delta\,\hat{\phi}. \end{aligned} \tag{149}$$

Expanding $\hat{\theta}$ and $\hat{\phi}$, in the Cartesian basis ($\hat{x}$, $\hat{y}$, $\hat{z}$), i.e.

$$\begin{aligned} \hat{\theta} &= \cos\theta\cos\phi\,\hat{x} + \cos\theta\sin\phi\,\hat{y} - \sin\theta\,\hat{z} \\ \hat{\phi} &= -\sin\delta\,\hat{\theta} + \cos\delta\,\hat{\phi} \end{aligned} \tag{150}$$

and substituting these transformations into Eq.149 we find

$$\begin{aligned} \hat{e}_1 &= [\cos\theta\cos\phi\cos\delta - \sin\phi\sin\delta]\,\hat{x} \\ &+ [\cos\theta\sin\phi\cos\delta + \cos\phi\sin\delta]\,\hat{y} \\ &- [\sin\theta\cos\delta]\,\hat{z} \end{aligned} \tag{151}$$

and

$$\begin{aligned}\hat{e}_1 &= -\left[\cos\theta\cos\phi\sin\delta\ +\sin\phi\cos\delta\right]\hat{x} \\ &- \ \left[\cos\theta\sin\phi\sin\delta\ -\cos\phi\cos\delta\right]\hat{y} \\ &+ \ \left[\sin\theta\sin\delta\right]\hat{z}.\end{aligned} \tag{152}$$

Thus the direction cosines of the two polarization directions can be written as the column vectors

$$\left(a_j^{e1}\right) = \begin{pmatrix} \cos\theta\cos\phi\cos\delta - \sin\phi\sin\delta \\ \cos\theta\sin\phi\cos\delta + \cos\phi\sin\delta \\ -\sin\theta\cos\delta \end{pmatrix} \tag{153}$$

and

$$\left(a_j^{e2}\right) = \begin{pmatrix} -\cos\theta\cos\phi\sin\delta\ -\sin\phi\cos\delta \\ -\cos\theta\sin\phi\sin\delta\ +\cos\phi\cos\delta \\ \sin\theta\sin\delta \end{pmatrix}. \tag{154}$$

The nonlinear polarization $P_j(\omega_m)$ induced by the nonlinear interaction in the medium produces an $\hat{e}_1$ or $\hat{e}_2$ polarized wave with frequency ω_3. The magnitude of the source polarization can be expanded in the $E_i^{e\alpha}$ polarization basis as

$$P^{e1}(\omega_3) = a_j^{e1} P_j(\omega_3) \tag{155}$$

$$P^{e2}(\omega_3) = a_j^{e2} P_j(\omega_3). \tag{156}$$

The induced second order nonlinear polarizabilities in biaxial crystals are therefore given by the following equations:

Type I: (157)

$$\begin{aligned}P^{e2}_{e_1e_1}(\omega_3) &= \epsilon_o a_i^{e2} d_{ijk}(\omega_3;\omega_2,\omega_1) a_j^{e1} a_k^{e1} E^{e1}(\omega_2) E^{e1}(\omega_1) \\ &= d^I_{eff}(\theta,\phi) E^{e1}(\omega_2) E^{e1}(\omega_1);\end{aligned}$$

Type II: (158)

$$\begin{aligned}P^{e2}_{e_2e_1}(\omega_3) &= \epsilon_o a_i^{e2} d_{ijk}(\omega_3;\omega_2,\omega_1) a_j^{e2} a_k^{e1} E^{e2}(\omega_2) E^{e1}(\omega_1) \\ &= d^{II}_{eff}(\theta,\phi) E^{e2}(\omega_2) E^{e1}(\omega_1)\end{aligned}$$

where d^I_{eff} and d^{II}_{eff} express the effective second-order nonlinear coefficients for Type I and Type II processes, respectively.

TABLE II

REDUCED ELECTRO-OPTIC TENSOR

m	1	2	3	4	5	6
(jk)	11	22	33	23	13	12
				32	31	21

In the case where the crystal is transparent over a region that includes ω_3, ω_2 and ω_1, d_{ijk} is known to be independent of frequency. Hence Eqs.157 and 158 may be rewritten, neglecting frequencies as simply

$$\begin{aligned} P^{e_2}_{e_1 e_1} &= \epsilon_o \, d_{ijk} \, a_i^{e_2} a_j^{e_1} a_k^{e_1} E^{e_1} E^{e_1} \\ &= d^{I}_{eff}(\theta, \phi) E^{e_1} E^{e_1} \end{aligned} \tag{159}$$

$$\begin{aligned} P^{e_2}_{e_2 e_1} &= \epsilon_o \, d_{ijk} \, a_i^{e_2} a_j^{e_1} a_k^{e_2} E^{e_1} E^{e_2} \\ &= d^{II}_{eff}(\theta, \phi) E^{e_1} E^{e_2}. \end{aligned} \tag{160}$$

No physical significance can be attached to an exchange of the E's in Eqs.159 and 160. Hence the last two indices of d_{ijk} can be replaced by a single index m. In this reduced notation, m runs from 1 to 6 with the corresponding definitions shown in Table II below. The intrinsic permutation symmetry serves to reduce of the number of independent d_{ijk} elements from $3^3 = 27$ elements to the 18 elements.

The third rank tensor d_{ijk} can now be written as a 3x6 matrix d_{im} when these contractions are applied. Equations 159 and 160 can now be written as matrix equations in the form that follows

$$\begin{pmatrix} P_1 \\ P_2 \\ P_3 \end{pmatrix} = \epsilon_o \begin{pmatrix} d_{11} & d_{12} & d_{13} & d_{14} & d_{15} & d_{16} \\ d_{21} & d_{22} & d_{23} & d_{24} & d_{25} & d_{26} \\ d_{31} & d_{32} & d_{33} & d_{34} & d_{35} & d_{36} \end{pmatrix} \begin{pmatrix} E_1^2 \\ E_2^2 \\ E_3^2 \\ 2E_2E_3 \\ 2E_1E_3 \\ 2E_1E_2 \end{pmatrix} . \tag{161}$$

The factor of 2 in the last three terms of the column vector on the right side arise from terms such as $E_2E_3 + E_3E_2 = 2E_2E_3$, etc..

If the second-order nonlinear polarization is purely electronic in origin and the crystal is loss less throughout the range of the three interacting frequencies, then Kleinman's symmetry condition is taken into account [34]. Kleinman's symmetry condition states that all d_{ijk} tensor elements formed by freely permuting i, j, and k must all be equivalent. Kleinman's symmetry condition further reduces the number of independent elements from 18 to 10. An example of a Kleinman reduction follows:

$$d_{123} = d_{312} = d_{231} \tag{162}$$

or in reduced notation

$$d_{14} = d_{36} = d_{25} \, . \tag{163}$$

The number of independent elements of d_{im} can be reduced even further by the requirement that the third rank polarizability tensor d_{ijk} obey the intrinsic symmetry of the host material [35]. We will consider this reduction for host crystals with orthorhombic $mm2$–C_{2v} symmetry only since all the SHG and OPO crystals studied in this investigation obey this crystal symmetry.

The d_{ijk} tensor transforms according to the product basis $\psi_{ijk} = \{x_i x_j x_k\}$, where $x_1 = x$, $x_2 = y$ and $x_3 = z$. Our task now is to find all the basis functions ψ_{ijk} which are invariant under the symmetry operations of the C_{2v} group: E, C_2, σ_v^x, σ_v^y [36]. Table III below shows the result of operating each symmetry elements in the C_{2v} group on the product basis ψ_{ijk}.

TABLE III

TRANSFORMATION OF ψ_{ijk} UNDER C_{2v} SYMMETRY

d_{im} indices	d_{ijk} indices	$x_ix_jx_k$	E	C_2	σ_v^x	σ_v^y	**Invariant**
11	111	xxx	xxx	$-xxx$	xxx	$-xxx$	
12	122	xyy	xyy	$-xyy$	xyy	$-xyy$	
13	133	xzz	xzz	$-xzz$	xzz	$-xzz$	
14	123	xyz	xyz	$-xyz$	$-xyz$	$-xyz$	
15	131	xzx	xzx	xzx	xzx	xzx	√
16	122	xxy	xxy	$-xxy$	$-xxy$	xxy	
21	211	yxx	yxx	$-yxx$	$-yxx$	yxx	
22	222	yyy	yyy	$-yyy$	$-yyy$	yyy	
23	233	yzz	yzz	$-yzz$	$-yzz$	yzz	
24	223	yyz	yyz	yyz	yyz	yyz	√
25	231	yzx	yzx	yzx	$-yzx$	$-yzx$	
26	212	yxy	yxy	$-yxy$	yxy	$-yxy$	
31	311	zxx	zxx	zxx	zxx	zxx	√
32	322	zyy	zyy	zyy	zyy	zyy	√
33	333	zzz	zzz	zzz	zzz	zzz	√
34	323	zyz	zyz	$-zyz$	$-zyz$	zyz	
35	331	zzx	zzx	$-zzx$	zzx	$-zzx$	
36	312	zxy	zxy	zxy	$-zxy$	$-zxy$	

From table III we find that d_{15}, d_{24}, d_{31}, d_{32} and d_{33} are the only d_{im} elements invariant under the C_{2v} symmetry operations. The number of independent elements are further reduced from this set by applying Kleinman's permutation symmetry condition, i.e.

$$d_{15} = d_{131} = d_{311} = d_{31} \tag{164}$$

and

$$d_{24} = d_{223} = d_{322} = d_{32}. \tag{165}$$

Hence, for crystals obeying the $mm2 - C_{2v}$ symmetry, there are only three independent d_{im} elements; d_{15}, d_{24}, and d_{33}. The matrix equation for the polarization components, obeying the $mm2 - C_{2v}$ symmetry, is therefore given by

$$\begin{pmatrix} P_x(\omega_3) \\ P_y(\omega_3) \\ P_z(\omega_3) \end{pmatrix} = \epsilon_o \begin{pmatrix} 0 & 0 & 0 & 0 & d_{15} & 0 \\ 0 & 0 & 0 & d_{24} & 0 & 0 \\ d_{15} & d_{24} & d_{33} & 0 & 0 & 0 \end{pmatrix} \begin{pmatrix} E_x(\omega_1)\, E_x(\omega_2) \\ E_y(\omega_1)\, E_y(\omega_2) \\ E_z(\omega_1)\, E_z(\omega_2) \\ E_y(\omega_1)\, E_z(\omega_2) + E_z(\omega_1)\, E_y(\omega_2) \\ E_x(\omega_1)\, E_z(\omega_2) + E_z(\omega_1)\, E_x(\omega_2) \\ E_x(\omega_1)\, E_y(\omega_2) + E_y(\omega_1)\, E_x(\omega_2) \end{pmatrix}. \tag{166}$$

The effective susceptibilities $d^I_{eff}(\theta, \phi)$ and $d^{II}_{eff}(\theta, \phi)$ can be calculated using these relations for the $mm2 - C_{2v}$ point group symmetry. The expansion of Eq.159 in terms of the surviving d_{ij} elements gives for $d^I_{eff}(\theta, \phi)$,

$$\begin{aligned} \tfrac{1}{\epsilon_o} d^I_{eff} &= d_{15}\,(a_1^{e2} a_3^{e1} a_1^{e1} + a_3^{e2} a_1^{e1} a_1^{e1}) \;+\; d_{24}\,(a_2^{e2} a_3^{e1} a_2^{e1} + a_3^{e2} a_2^{e1} a_2^{e1}) \\ &+ d_{33} a_3^{e2} a_3^{e1} a_3^{e1}\,. \end{aligned} \tag{167}$$

Substituting in the direction cosines, given by Eqs.153 and 154, simplifying we find the expression

$$\begin{aligned}\tfrac{1}{\epsilon_o}d^{I}_{eff}(\theta,\phi) &= (d_{24}-d_{15})\,(3\sin^2\delta-1)\sin\theta\cos\theta\sin^2\phi\cos\delta \\ &- 3\,(d_{15}\cos^2\phi+d_{24}\sin^2\phi)\sin\theta\cos^2\theta\sin\delta\cos^2\delta \\ &+ (d_{15}\sin^2\phi+d_{24}\cos^2\phi)\sin\theta\sin\delta\,(3\sin^2\delta-2) \\ &+ d_{33}\sin^3\theta\sin\delta\cos^2\delta\,.\end{aligned} \tag{168}$$

Likewise, expanding Eq.160 in terms of the surviving d_{ij} elements gives for $d^{II}_{eff}(\theta,\phi)$,

$$\begin{aligned}\tfrac{1}{\epsilon_o}d^{II}_{eff}(\theta,\phi) &= d_{15}\,(a_1^{e2}a_3^{e1}a_1^{e2}+a_3^{e2}a_1^{e1}a_1^{e2}) \;+\; d_{24}\,(a_2^{e2}a_3^{e1}a_2^{e2}+a_3^{e2}a_2^{e1}a_2^{e1}) \\ &+ d_{33}a_3^{e2}a_3^{e1}a_3^{e2}.\end{aligned} \tag{169}$$

Again, substituting in the direction cosines and simplifying we find the expression

$$\begin{aligned}\tfrac{1}{\epsilon_o}d^{II}_{eff}(\theta,\phi) &= (d_{24}-d_{15})\,(3\cos^2\delta-1)\sin\theta\cos\theta\sin^2\phi\cos\delta \\ &- 3\,(d_{15}\cos^2\phi+d_{24}\sin^2\phi)\sin\theta\cos^2\theta\sin^2\delta\cos\delta \\ &- (d_{15}\sin^2\phi+d_{24}\cos^2\phi)\sin\theta\cos\delta\,(3\cos^2\delta-2) \\ &- d_{33}\sin^3\theta\sin^2\delta\cos\delta\,.\end{aligned} \tag{170}$$

Equations 168 and 170 constitute the central result of this discussion. These relations describe the magnitude of the coupling is between the fields for a given set of phase matching angles θ_m, ϕ_m.

As was shown previously, the intensity of the generated nonlinear field is proportional to d_{eff}. Thus, in order to determine the set of phase matching angles that yield the highest conversion efficiency we need only substitute the set of angles θ_m, ϕ_m into $d_{eff}(\theta_m\phi_m)$ and select the set of angles that maximize d_{eff}. In this way, we can select the set of optimum phase matching angles $(\theta_m, \varphi_m)|_{opt}$ and phase matching type (Type I or Type II) that maximize the conversion efficiency. From these arguments it can be seen that the calculation and selection of the optimum set of angles $(\theta_m, \varphi_m)|_{opt}$ is the single most important step taken to obtain efficient frequency conversion in nonlinear, dispersive media.

We are now in position to present some specific results of these phase matching calculations as applied to the crystal studied in this investigation.

SHG Phase Matching Angles for KTP and KTA

The crystals studied for use as efficient second harmonic generators were KTP, KTA, RTA, KCTA. However, only KTP and KTA were considered in these calculations since only these materials have known Sellemeir's coefficients. These crystals belong to the $mm2$ point group [2], i.e. they obey C_{2v} symmetry. Thus the expressions for $d^{I}_{eff}(\theta,\varphi)$ and $d^{II}_{eff}(\theta,\varphi)$ of the previous section apply to all the crystals studied. In each case, the second harmonic output of a Nd:YAG laser (λ_{ω_p}=1064nm, $\lambda_{2\omega_p}$=532nm) is the desired output. Hence these wavelengths must be used as input parameters for the computer program given in the Appendix. Since SHG is a special case of the three frequency mixing process, the variable $\omega_3 = 2\omega$, $\omega_1 = \omega_2 = \omega$ must also be set as parameters in the computer program.

KTP

The critical data required to complete the phase matching calculations are the Sellemier coefficients and the polarizability coefficients d_{15}, d_{24}, and d_{33} for each specific crystal studied. The corresponding Sellemier's equations and d_{ij} coefficients for KTP were measured and shown to be [37]

$$
\begin{aligned}
n^2_{x,KTP}(\lambda) &= 3.0129 + \tfrac{0.03807}{\lambda^2-0.04283} - 0.01664\,\lambda^2 \qquad (171)\\
n^2_{y,KTP}(\lambda) &= 3.0333 + \tfrac{0.04106}{\lambda^2-0.04946} - 0.01695\,\lambda^2\\
n^2_{z,KTP}(\lambda) &= 3.3209 + \tfrac{0.05305}{\lambda^2-0.05960} - 0.01763\,\lambda^2
\end{aligned}
$$

and [38]

.

Utilizing this data we find from Eqs.136 and 137 $\delta \simeq 2^o$. Submitting the necessary parameters to the computer program in the Appendix, we obtain the curves shown in Fig.9. From this analysis we see that KTP is both Type I and Type II phase matchable for doubling the fundamental wavelength $\lambda_{\omega_p} = 1.064\mu$m.

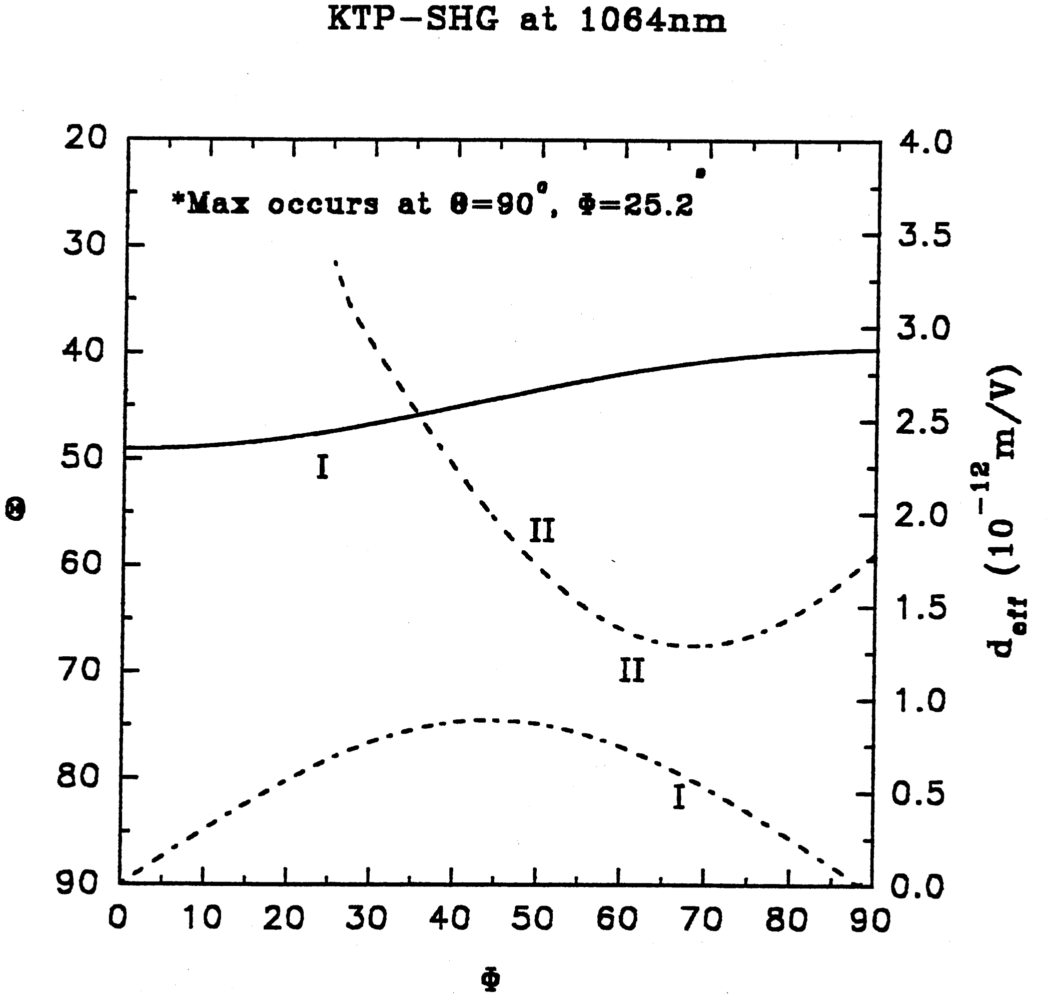

Figure 9. SHG phase matching curves of KTP for a pump wavelength of $\lambda_p = 1064$nm.

TABLE IV

ELECTRO-OPTIC COEFFICIENTS OF KTP

d_{ij} **at 1.064μm**	**(pm/V)**
d_{15}	1.91
d_{24}	3.64
d_{31}	2.54
d_{32}	4.35
d_{33}	16.9

The maximum d_{eff}, and hence maximum conversion efficiency, is satisfied for Type II phase matching at angles $(\theta_m^{II}, \phi_m^{II})\,|_{opt}= 90^o, 25.2^o$, as shown in Fig.9.

KTA

The necessary data required for KTA is not as readily available since KTA is a much newer material than KTP. Samples having a single ferroelectric domain are extremely rare. It is essential that a samples domain structure be known since phase matching calculations are based on the premise that the domain orientation correspond to the physical axes of the crystal. It has been conjectured that KTA is impossible to pole (a process used to electrostatically align the ferroelectric domains)—as a result of these difficulties crystal growers have been forced to rely on their ability to grow large, single domain crystals.

Recently, Sellemier's coefficients were measured on samples that were believed to have a single ferroelectric domain [39]. The Sellemier's fit to the indices of refraction were given by

$$
\begin{aligned}
n^2_{x,KTA}(\lambda) &= 2.1106 + \frac{1.0318}{\left[1-\left(\frac{0.2109}{\lambda}\right)^2\right]} - 0.0106\,\lambda^2 \qquad (172) \\
n^2_{y,KTA}(\lambda) &= 2.3889 + \frac{0.7790}{\left[1-\left(\frac{0.2378}{\lambda}\right)^2\right]} - 0.0150\,\lambda^2 \\
n^2_{z,KTA}(\lambda) &= 2.3472 + \frac{1.1011}{\left[1-\left(\frac{0.2402}{\lambda}\right)^2\right]} - 0.0174\,\lambda^2.
\end{aligned}
$$

However, the available data on the d_{ij} coefficients [40] is questionable [41]. In our calculations of d_{eff}, we accepted only the ratios of the d_{ij} coefficients as being correct, i.e. $d_{24}/d_{15} \simeq 1.4$. Submission of this data to the computer program in the Appendix yields the phase matching curves shown in Fig.10.

From these curves it is evident that KTA is not Type II phase matchable for the fundamental wavelength $\lambda_{\omega_p} = 1.064\mu$m. Optimum conversion efficiency is obtained with Type I phase matching in KTA at angles $(\theta^I_m,\ \phi^I_m)\ |_{opt}= 48^o,\ 45^o$. This is a rather unfortunate consequence of KTA's dispersion properties since the value of d^I_{eff}(KTA) is only 0.16 that of d^{II}_{eff}(KTP) at $\lambda_{\omega_p} = 1.064\mu$m, which would imply a conversion efficiency ratio of the same factor. KTA is therefore an inferior material as compared to KTP for doubling the $\lambda_{\omega_p} = 1.064\mu$m fundamental wavelength.

Figure 11 shows that KTA will double other fundamental wavelengths under Type II phase matching conditions. In fact, Type II phase matching in KTA is possible for fundamental wavelengths in the range 1.14μm—3.6μm, where 3.6μm is the wavelength of the first infrared absorption band edge [40]. Coincidentally, the Nd:YAG pumped F_{2-} — center laser is tunable over the range 1.1—1.25μm centered at $\lambda_{\omega_p} = 1.14\mu$m [42]. Submitting the parameters $x_1 = x_2 = 0.57\mu$m to the computer program in the Appendix we obtain the phase matching curves for the F_{2-} — center laser, shown in Fig.12. From this figure it is evident that d^{II}_{eff} is greater than d^I_{eff} over the entire range of phase matching angles, and is maximized by the angles $(\theta^{II}_m,\ \phi^{II}_m)\ |_{opt}= 84.45^o,\ 0^o$.

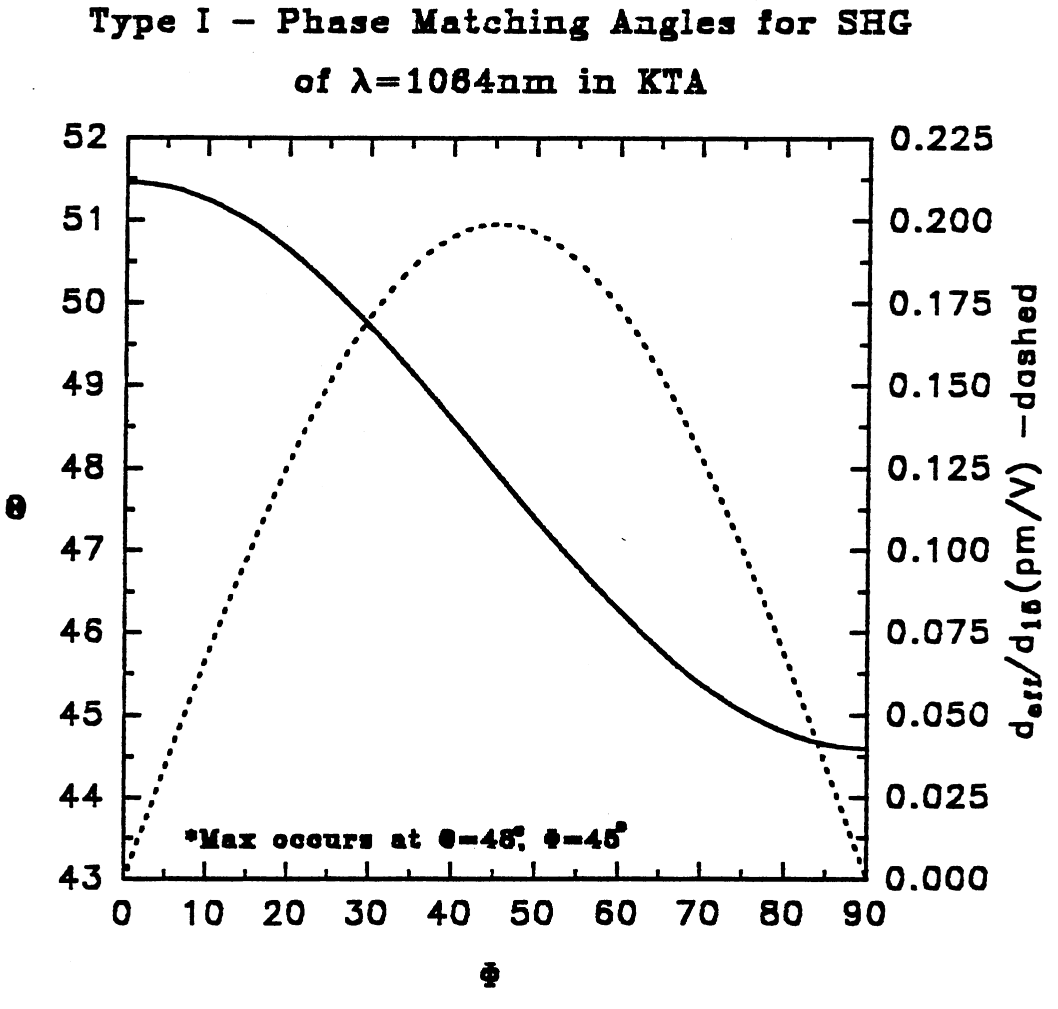

Figure 10. SHG phase matching curves of KTA for a pump wavelength of $\lambda_p = 1064\text{nm}$. KTA is not type II phase matchable.

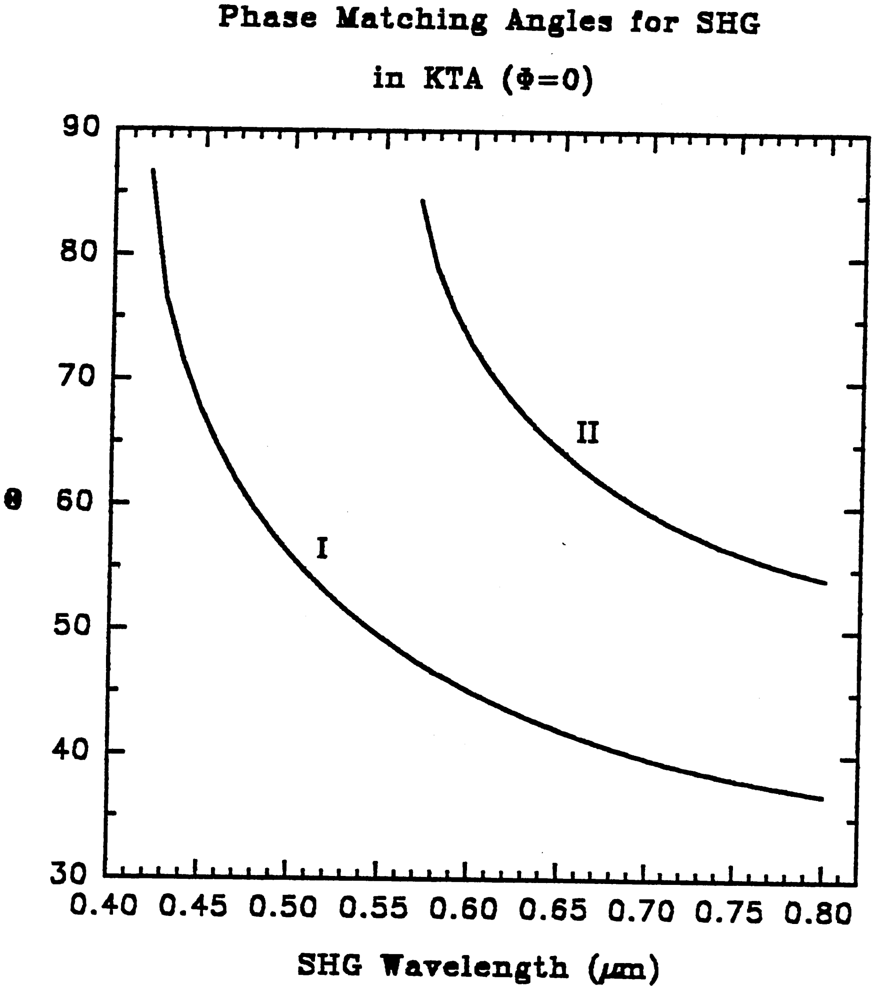

Figure 11. Possible phase matching angles with $\phi = 0°$ for various SH output wavelength.

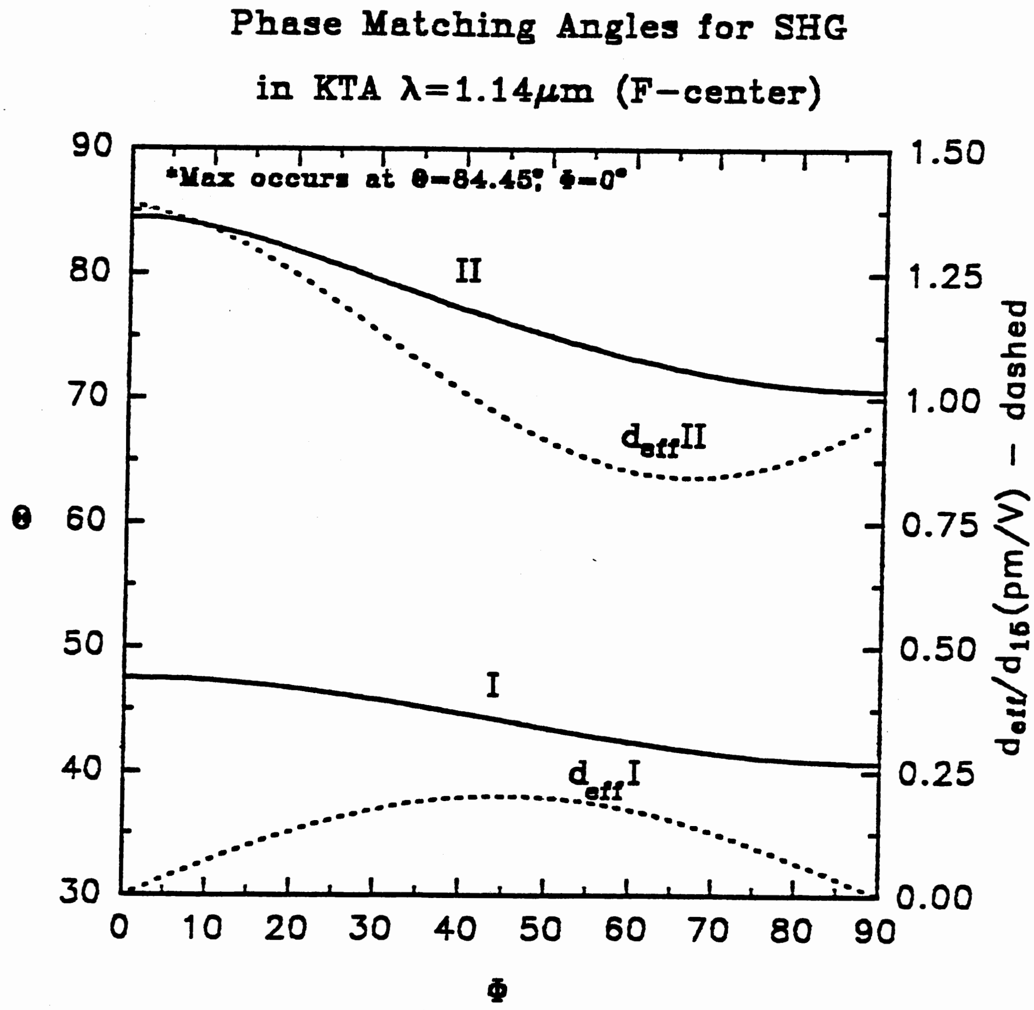

Figure 12. SHG phase matching curves of KTA for a pump wavelength of $\lambda_p = 1.140\mu m$.

OPO Phase Matching Angles for KTP and KTA

The same set of crystals studied in SHG were studied in application to OPOs (i.e. KTP and KTA). The phase matching conditions were calculated with the constraint that the degenerate point of the signal and idler occur for the pump wavelength of λ_p=750nm, i.e. $\lambda_s = \lambda_i = 1.5\mu$m. This pump wavelength was chosen for this degenerate point since λ_p=750nm is the midpoint of the Alexandrite lasers' tuning curve (720nm–800nm), and therefore delivers the maximum pump field intensity available and provides for the most stable pump laser operation. In addition, this choice allows for the maximum range of tunability.

The three frequency interactions of the OPO are subject to the constraint that, at degeneracy, $\omega_s = \omega_i = \omega_p/2$. Hence the parameters and constraints submitted to the computer program in the Appendix are $\omega_3 = \omega_p$, $\omega_1 = \omega_2 = \omega_3/2$.

KTP

The results of these calculations for KTP are shown in Fig.13. The phase matching curves shown in this figure indicate that KTP is both Type I and Type II phase matchable for the degenerate point λ_p=750nm. It is obvious from the curves that d_{eff} is maximized under Type II phase matching conditions. The optimum phase matching angles are $(\theta_m^{II}, \phi_m^{II})\,|_{opt}= 54.91^o, 0^o$.

KTA

Likewise, the necessary calculations were made for KTA, at the same degenerate point. The results of these phase matching calculations are shown in Fig.14.

As with KTP, KTA demonstrates both Type I and Type II phase matching for this degenerate point. The maximum value of d_{eff} occurs for Type II phase matching, for the phase matching angles of $(\theta_m^{II}, \phi_m^{II})\,|_{opt}= 56.28^o, 0^o$. Comparing the maximum value of d_{eff} between KTA and KTP we find for this configuration

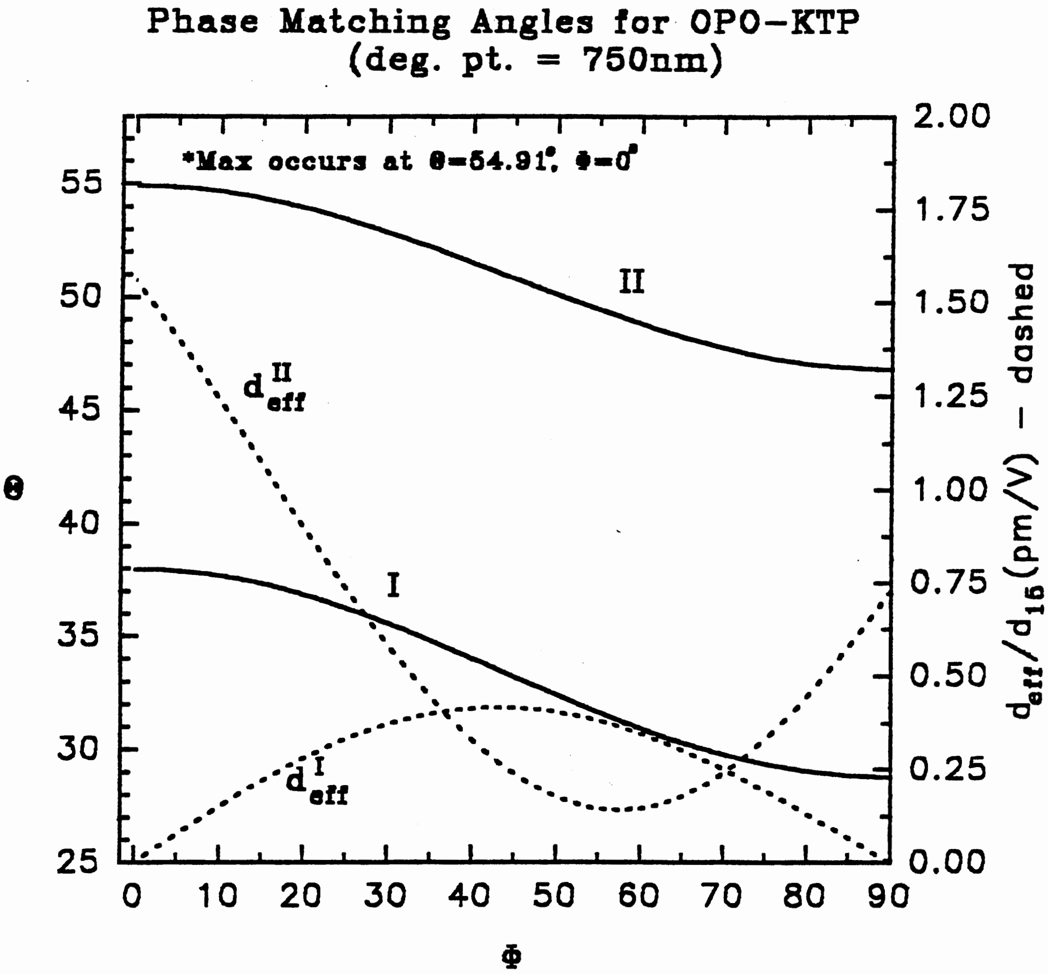

Figure 13. Phase matching curves for KTP OPO where the degenerate point of operation is $\lambda_p = 750$nm.

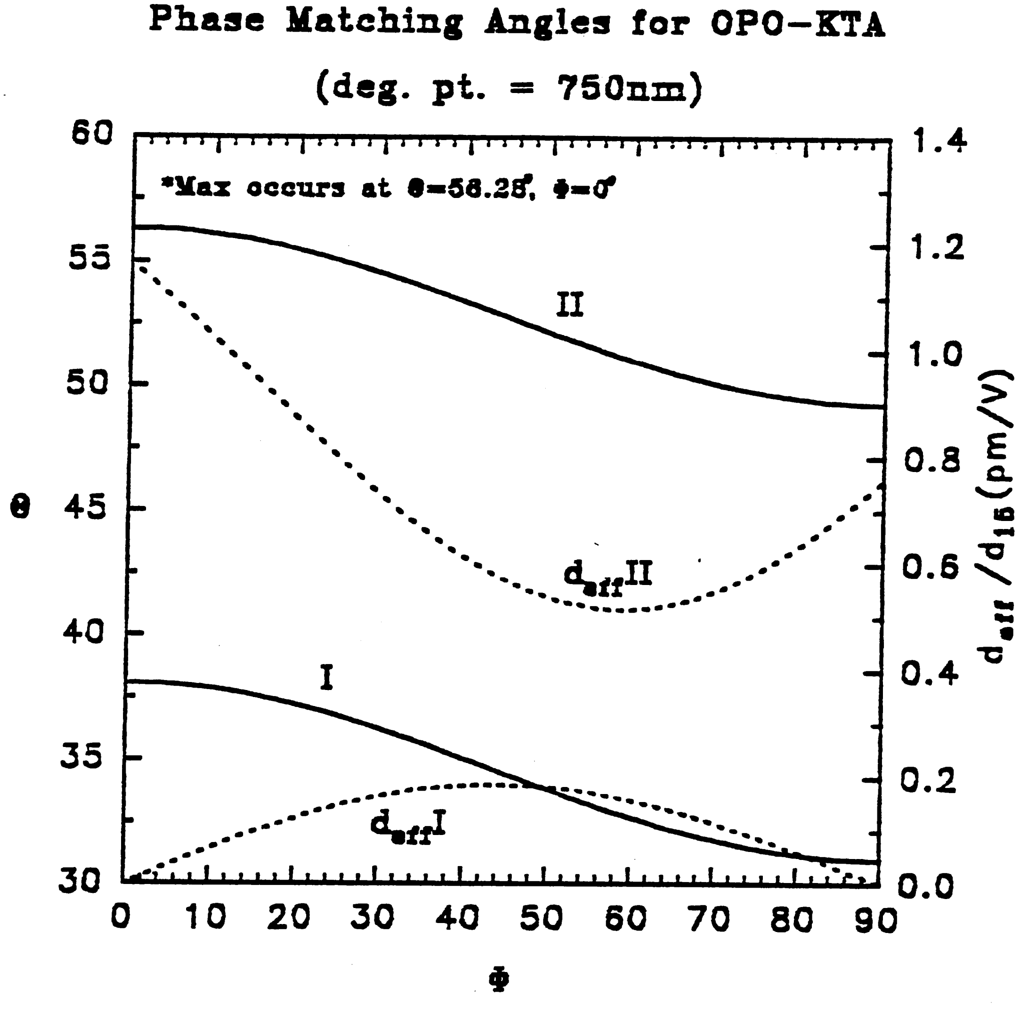

Figure 14. Phase matching curves for KTA OPO where the degenerate point of operation is λ_p = 750nm.

d^{II}_{eff}(KTA) is 1.6 times larger than d^{II}_{eff}(KTP), which implies KTA will yield a conversion efficiency 1.6 times that of KTP.

CHAPTER VI

STIMULATED RAMAN SCATTERING

Introduction

Stimulated Raman scattering (SRS) was accidentally discovered by Woodbury and Ng in 1962 [52]. In studying Q-switching of a ruby laser by a nitrobenzene Kerr cell, they detected intense infrared radiation emitted from the Kerr cell whose origin was not immediately identified. Eckhardt [53] first proposed the correct interpretation as stimulated Raman emissions from nitrobenzene. This was soon after verified experimentally by Eckhardt, et al. [54].

Subsequently, a similar effect was observed in many other liquids by Eckhardt et al. [54], Geller et al. [55], and Stoicheff [56], in several solids by Eckhardt et al. [57], and in H_2 gas by Minck et al [58]. An early theoretical treatment of SRS was given by Hellwarth [59] in 1963.

SRS can be used to shift the emission frequency of lasers to different spectral regions. SRS has been demonstrated in various gas, liquid and solid-state media [43], but most practical applications involve the use of gas cells. The advantages of solid-state Raman shifters are their intrinsically high concentration of Raman active centers and their relatively high thermal and mechanical properties. This can result in high gain, reliable, small dimension ($\sim$ 4cm) SRS shifters as opposed gas phase devices which require the use of long ($\sim$ 50cm), high pressure ($\sim$ 500psi) chambers. However, few crystals have been identified that possess narrow, isolated, intense Raman active vibronic modes necessary to produce efficient scattering [44]. Normally, these intense modes can be attributed to strong internal symmetrical vibrations within covalent ion complexes, such as $(CO_3)^{-1}$, $(NO_3)^{-1}$, and $(WO_4)^{-1}$. It was suggested earlier by Eckhardt [44] that molecular crystals containing these complexes should exhibit strong SRS. Barium nitrate is one molecular crystal that possesses these qualities.

Spontaneous Raman Spectra of $Ba(NO_3)_2$

Despite the simplicity of its chemical formula, $Ba(NO_3)_2$, its crystalline structure has been the subject of debate for many years. The controversy hinges on the existence or absence of a center of symmetry in the unit cell. The dispute involves the centric cubic space group P_a3 and the corresponding non–centric group $P2_13$. The standard tests (Neutron and x-ray diffraction, piezoelectric, and optical activity measurements) all weakly favor the centric P_a3 space group [45]. Recently however, conclusive tests were made using magnetic resonance techniques (which are invariant to an inversion operation) [45], that prove the structure belongs to the $P_a3 - T_h^6$ space group. From this information we can analyze the modes of oscillation and determine which modes will be Raman active and hence which modes are candidates for SRS.

In order to do this we must first determine the mode structure of the free NO_3^{-1} ion. Menzies [46] performed the analysis of these modes and found, out of the expectant six internal modes, four internal modes of oscillation–two of which are degenerate. These four modes of oscillation are shown in Fig.15.

A central result of symmetry in quantum mechanics is that the eigen functions of a symmetrical Hamiltonian can be labeled by the irreducible representations of the symmetry group of the Hamiltonian and that degeneracies with orders equal to the dimension of those representations would occur [36]. For a molecule with symmetry, both the kinetic and potential energies are unchanged by a symmetry operation and hence the general results apply to the normal modes of oscillation for a particular molecule. Therefore the normal modes q_k may be labeled by the irreducible representations of the symmetry group. Furthermore, for an irreducible representation $T^{(\alpha)}$ of dimension s_α there will be a set of s_α linearly independent normal coordinates all with the same energy and hence frequency.

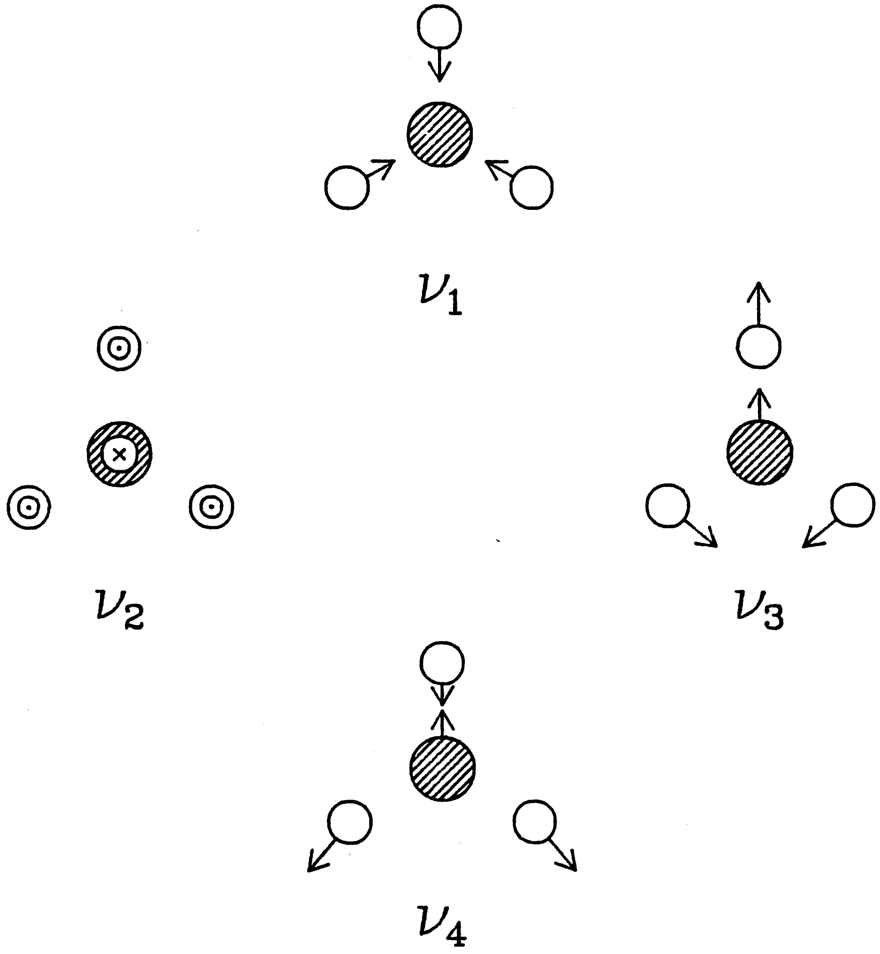

Figure 15. Free NO_3^{-1} ion normal mode vibrations: ν_1 is the totally symmetric vibration in the symmetry plane of the ion, ν_2 is the symmetric vibration perpendicular to the symmetry plane of the ion, ν_3 and ν_4 are doubly degenerate vibration in the symmetry plane of the ion.

TABLE V

CHARACTER TABLE OF THE D_{3h} SYMMETRY GROUP

D_{3h}	E	$2C_3$	$3C_2$	σ_h	$2S_3$	$3\sigma_v$		
A_1'	1	1	1	1	1	1		$\alpha_{xx}+\alpha_{yy},\alpha_{zz}$
A_2'	1	1	-1	1	1	-1	R_z	
E'	2	-1	0	2	-1	0	(T_x,T_y)	$\alpha_{xx}-\alpha_{yy},\alpha_{xy}$
A_1''	1	1	1	-1	-1	-1		
A_2''	1	1	-1	-1	-1	-1	T_z	
E''	2	-1	0	-2	1	0	(R_x,R_y)	α_{xz},α_{yz}

The NO_3^{-1} ion obeys the symmetry operations of the D_{3h} group, hence the four normal modes shown in Fig.15 can be labeled by four of the six irreducible representations of the D_{3h} group, where two of the six are doubly degenerate. The pairing of the normal modes with the irreducible representations can be determined by examining the transformation properties of each particular mode. The character table of the D_{3h} group, shown in Table V, can be used to determine this pairing.

Included in Table V are the species of translation T_x, T_y and T_z in the x, y and z directions, respectively; and rotations R_x, R_y and R_z in a right–handed system parallel to the x, y and z axes, respectively. Also, the species of the polarizability tensor elements α_{ij}, are identified.

Starting with the first mode ν_2, we immediately recognize the mode to be singly degenerate. Therefore this mode is transformed by a one–dimensional representation, i.e. an A representation. It is obvious from Fig.15 that the sign of each displacement is reversed under the operations $3C_2$, σ_m, and S_3. It follows that the only representations with negative characters for these elements is the A_2'' representation. Hence ν_1 is transformed by A_2'' and is therefore named $A_2''(\nu_1)$.

Continuing, we turn to the most obvious mode ν_1. This mode is also singly degenerate and hence transformed by an A representation. However, for this mode the sign of the displacements do not change under any of the symmetry operations, that is ν_1 is a 'totally' symmetric mode. Therefore this mode must be transformed under the A_1' representation and is hence named $A_1'(\nu_1)$.

The next two modes are less obvious to pair. Since both modes are doubly degenerate, they must be transformed by one of the E, two-dimensional representation. A key observation is that both of these modes are invariant under the σ_h operation, hence their character must be 2. The only E representation with a character of 2 is the E' representation. Therefore, both of these modes must be transformed by the E' representation and are hence named $E'(\nu_3)$ and $E'(\nu_4)$.

The spectral activity of each mode can easily be determined by examining the last two columns of Table V. A mode is infrared active if its motion causes a variation in the dipole moment of the molecule. Likewise, a mode is Raman active if it causes a variation in the optical polarizability of the molecule. It is readily apparent in Fig.15 that each mode, with the exception of $A'(\nu_1)$, has a varying molecular dipole moment. Therefore, we can predict that $A''(\nu_2)$, $E'(\nu_3)$, and $E'(\nu_4)$ are all infrared active. Observing a variation in the optical polarizability is much more difficult since the polarizability is a second rank tensor and therefore transforms as the product basis: $\{x^2, y^2, z^2, xy, xz, yz\}$. The last column of Table V conveniently summarizes the transformation properties of the polarizability tensor, α_{ij}. This column gives the species of the optical polarizability tensor transformed by each irreducible representation of the D_{3h} group. Therefore, at a glance, the spectral activity can be determined with such a table. From this analysis we conclude that $A_1'(\nu_1)$, $E'(\nu_3)$, and $E'(\nu_4)$ are all Raman active vibronic modes.

It is worth noting at this point that the strength of the Raman activity is related to whether or not the diagonal elements of the optical polarizability tensor α_{ij} are co–transformed by a representation belonging to a particular vibronic mode: If the diagonal elements of α_{ij} are co-transformed then the mode belonging to that representation will be strongly Raman active; contrarily, if only the off-diagonal elements of α_{ij} are co-transformed then the vibronic mode belonging to this representation will be weakly Raman active. Therefore, from the onset, we conclude that $A'(\nu_1)$ is the dominant Raman active mode of oscillation in the NO_3^{-1} ion.

We are now in a position to place the NO_3^{-1} ion complex into the crystal lattice of $Ba(NO_3)_2$. As might be expected, this new environment changes the symmetry properties of the vibronic modes. A consequence of the new environmental symmetry, will be the splitting of previously degenerate modes, since the crystalline structure of the host is of lesser symmetry than the ion complex. Another environmental consequence is the onset of new 'external' modes of oscillation, which are generated by oscillations amongst neighboring ionic complexes.

We will use the factor group analysis method, developed by Winston and Halford [47], to determine the normal modes in $Ba(NO_3)_2$. This method was developed to correctly determine both the set of new 'external' modes of oscillation and the set of surviving 'internal' modes of oscillation intrinsic to the new crystalline environment. Using this method, we must first determine the number of molecules per Bravis space cell [48]. Wychoff has tabulated this data for most crystals, giving a value of four molecules per Bravis cell in $Ba(NO_3)_2$ [49]. This information is essential in determining the site symmetry observed by each ion complex in the crystal. The possible site symmetries for crystals obeying a certain space group has been tabulated by Fatley et al.[48]. Here it is shown that the possible site symmetries for the $Pa3 - T_h^6$ space group are

$$Pa3 - T_h^6 : 2S_6(4); C_3(8); C_1(24)$$

where the number in parenthesis ( ) is the number of sites in the Bravis cell that observe that particular symmetry. Since there are 8 — NO_3^{-1} ion complexes in the Bravis space cell and there are 8 — C_3 symmetry sites in the $Pa3$ space group, the NO_3^{-1} ion will occupy a site with C_3 local symmetry. Likewise, since there

TABLE VI

CHARACTER TABLE OF THE C_3 SYMMETRY GROUP ($\epsilon = e^{-\frac{2\pi i}{3}}$)

C_3	E	C_3	C_3^2	D_3 Correlation
A	1	1	1	A_1', A_1''
E	1	ϵ	ϵ^*	E', E''
	1	ϵ^*	ϵ	

are 4 — Ba^+ ions per the Bravis cell, the Ba^+ ions will occupy sites with S_6 local symmetry.

By knowing the symmetry observed by the ion complexes and the intrinsic symmetry of the ion complexes, we can determine the irreducible representations which are common to both the ion complex and the local site that it occupies. This correlation will determine which modes of oscillation that survive the symmetry change of the new environment. The correlation is most easily determined by correlating the characters of the representations amongst the ion complex and local site symmetry groups.

We start by correlating the symmetry group of the NO_3^{-1} ions to its local site symmetry, i.e. D_{3h} to C_3. Table VI below shows the character table of C_3.

To obtain the species of D_{3h} that correlate with those species of C_3, we need only compare the characters of the operations common to both symmetry groups C_3 and D_{3h}. In this case, the common symmetry operations are E, C_3 and C_3^2. Since C_3 is of lesser symmetry that D_{3h}, more than just one representation of D_{3h} will correlate with a single representation of C_3. The last column in Table VI shows which of the D_{3h} representations correlate with the two representations of C_3.

The correlation of the symmetry group obeyed by the Ba^+ ion with the symmetry of its occupation site is trivial since the Ba^+ ion obeys spherical symmetry. Therefore, the symmetry obeyed by the free Ba^+ ion has a one-to-one correlation with the S_6 symmetry of the local site it will occupy.

Continuing, we now consider how well the crystal symmetry translates the local site symmetry. That is, we now have to consider the correlation between the site symmetry and the crystal symmetry. Ultimately, this will determine the fate of the original free ion vibronic modes and will determine the new modes of oscillation amongst neighboring ion complexes.

The correlation between the site symmetry and its host crystalline symmetry follows directly as before. We need only compare the characters between the common group operations of the local site symmetry group C_3 and crystal symmetry group T_h^6 shown in Table VII below.

We see from the tables that there are direct correlations between the representatives $A \rightarrow A_g, A_u$ and $E \rightarrow E_g, E_u$. These are not the only correlations however — combinations of two or more representations like $A \dot{+} E$ in C_3 directly correlate to both F_g and F_u, i.e. $A + E \rightarrow F_g, F_u$.

Continuing with the correlation between the S_6 sites symmetry seen by the Ba^+ ion, and the T_h^6 crystal symmetry we find from Tables VIII and VII a direct correlation between $A_g \rightarrow A_g$, $A_u \rightarrow A_u$, $E_g \rightarrow E_g$, $E_u \rightarrow E_u$ and correlations between the combinations $A_g \dot{+} E_g \rightarrow F_g$ and $A_u \dot{+} E_u \rightarrow F_u$.

The symmetry correlations are summarized in the correlation trees shown in Fig.16.

We have found that each A mode derived from the nitrate ion will give rise to eight vibrations (two non degenerate and two triply degenerate modes), and each of the E modes will give rise to 16 vibrations (two doubly degenerate and four triply degenerate modes).

The unperturbed (free) nitrate ion, D_{3h} symmetry, has been shown to demonstrate the following spectrum [46]: $\nu_1(A_1')$ Raman active around 1050cm^{-1}, $\nu_2(A_2'')$

TABLE VII

CHARACTER TABLE OF THE T_h^6 SYMMETRY GROUP ($\epsilon = e^{-\frac{2\pi i}{3}}$)

T_h^6	E	$4C_3$	$4C_3^2$	$3C_2$	i	$4S_6$	$4S_6^5$	$3\sigma_h$		
A_g	1	1	1	1	1	1	1	1		$\alpha_{xx} + \alpha_{yy} + \alpha_{zz}$
E_g	1	ϵ	ϵ	1	1	ϵ	ϵ^*	1		$\alpha_{xx} + \alpha_{yy} - 2\alpha_{zz}$,
	1	ϵ	ϵ	1	1	ϵ^*	ϵ	1		$\alpha_{zz} - \alpha_{yy}$
F_g	3	0	0	-1	3	0	0	-1	R_x, R_y, R_z	$\alpha_{xy}, \alpha_{xz}, \alpha_{yz}$
A_u	1	1	1	1	-1	-1	-1	-1		
E_u	1	ϵ	ϵ^*	1	-1	$-\epsilon^*$	$-\epsilon^*$	-1		
	1	ϵ^*	ϵ	1	-1	ϵ^*	$-\epsilon$	-1		
F_u	3	0	0	-1	-3	0	0	1	T_x, T_y, T_z	

TABLE VIII

CHARACTER TABLE OF THE S_6 SYMMETRY GROUP ($\epsilon = e^{-\frac{2\pi i}{3}}$)

S^6	E	C_3	C_3^2	i	S_6^5	S_6		
A_g	1	1	1	1	1	1	R_z	$\alpha_{xx} + \alpha_{yy}, \alpha_{zz}$
E_g	1	ϵ	ϵ^*	1	ϵ	ϵ^*	R_x, R_y	$\alpha_{xx} - \alpha_{yy}$,
	1	ϵ^*	ϵ	1	ϵ^*	ϵ		α_{xz}, α_{yz}
A_u	1	1	1	-1	-1	-1	T_z	
E_u	1	ϵ	ϵ^*	-1	$-\epsilon$	$-\epsilon^*$	T_x, T_y	
	1	ϵ^*	ϵ	-1	$-\epsilon^*$	$-\epsilon$		

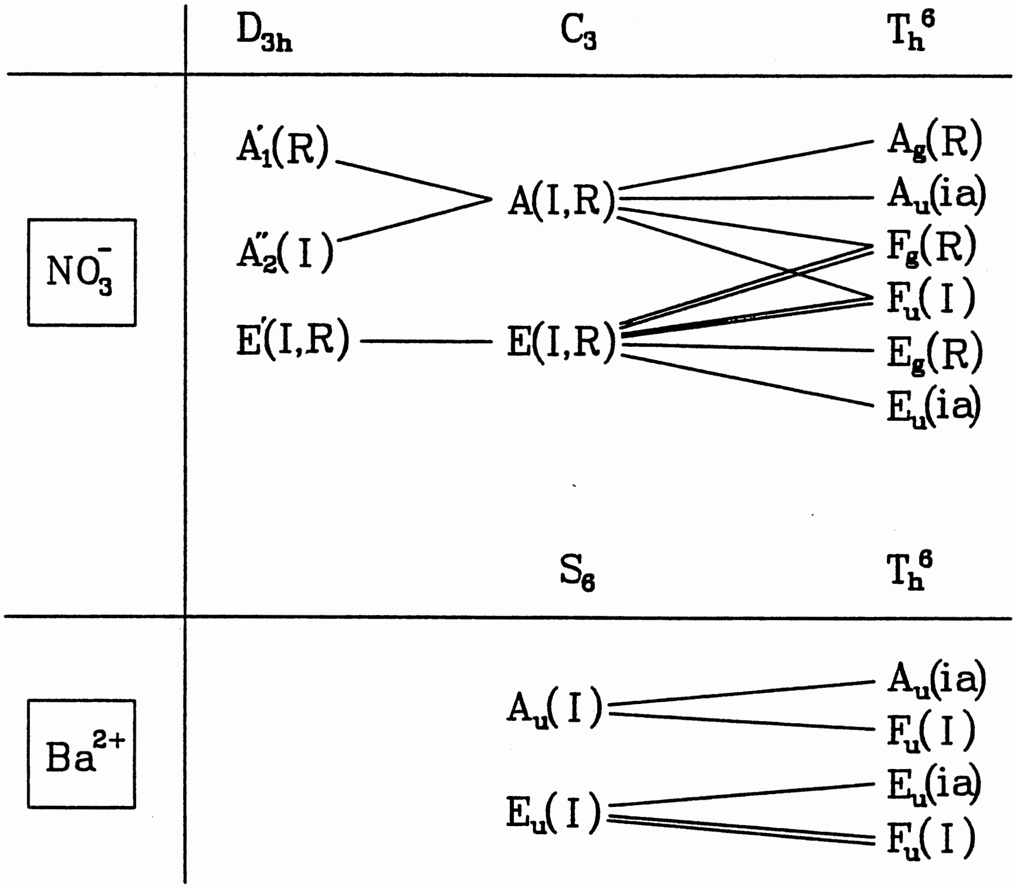

Figure 16. Correlation tree: This tree shows the correlation between the irreducible representations of the free ion symmetry groups to those of the crystal symmetry group, via the irreducible representations of the site symmety groups.

infrared active around 825cm^{-1}, $\nu_3(E')$ and $\nu_4(E')$ both Raman and infrared active around 1380 and 720cm^{-1}, respectively. From the factor group analysis above, it can be seen that for the cubic Ba(NO$_3$)$_2$ crystals: (a) ν_1 should split into two Raman active modes and a non–coincident infrared band; (b) ν_2 should have a single infrared band and two non–coincident Raman modes; and (c) both ν_3 and ν_4 should split into three Raman active and two non–coincident infrared bands.

The frequencies and relative intensities obtained from infrared and Raman studies [50] are collected in Table IX together with the tentative factor group assignment.

The spontaneous Raman spectra of Ba(NO$_3$)$_2$ is shown in Fig.17. Here it is evident that the sharp, intense, totally symmetric $\nu_1(A_g) = 1047.8\text{cm}^{-1}$ mode dominates all other modes. That is it is both intense and has an extremely narrow line width($< 1.5\text{cm}^{-1}$), which is precisely the characteristic spectra desired to obtain efficient SRS [44]. We would expect much the same behavior out of isomorphic crystals such as; Ca(NO$_3$)$_2$, Sr(NO$_3$)$_2$ and Pb(NO$_3$)$_2$.

SRS Theory

The effect described corresponds to the Raman effect, where a quantum of the pumping laser energy $\hbar\omega_p$ is absorbed stimulating a quantum of energy $\hbar\omega$ to be emitted. If the energy of the emitted photon is $\hbar\omega < \hbar\omega_p$, the output radiation is said to be Stokes radiation. Contrarily, if $\hbar\omega > \hbar\omega_p$, the output radiation is said to be anti-Stokes radiation. For these processes to occur, the energy difference $\hbar\omega_\nu$ must be accepted or released from the host medium. As will be seen, this energy is taken from (or added to) an optical phonon mode of the host medium.

The interaction between an incident 'pump' beam and optical phonon in a Raman active media has been studied classically [14,60], semi classically (where the active-medium excitations are considered to be quantitized) [60,61], and quantum mechanically [14]. We present the classical derivation of the equations that couple pump and Stokes waves to give a simple physical picture of this phenomena

TABLE IX

INFRARED AND RAMAN SPECTRA OF $Ba(NO_3)_2$

$Ba(NO_3)_2$		Factor Group	Free-ion D_{3h}
Infrared	Raman	Assign.	Vibration
	83(0.9)	F_g	
	133(0.6)	E_g	
		F_g	
	144(0.6)	E_g	
731(1.2)		F_u	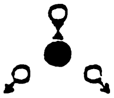
	730.5(0.03)	E_g	
	732.0(0.05)	+	
	733.4(?)	$2F_g$	
817(1.0)		F_u	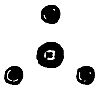
	821(0.001)	$A_g + F_g$	
1047(0.03)		F_u	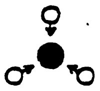
		F_g	
	1048(1.0)	A_g	
1345(1.5)		F_u	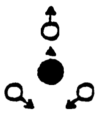
	1357(0.03)	E_g	
	1388(0.04)	F_g	
	1405(0.06)	F_g	
1415(0.9)		F_u	
1462(0.06)	1463(w)		
	1634(0.006)		
	1638(0.004)		
1780(0.02)			

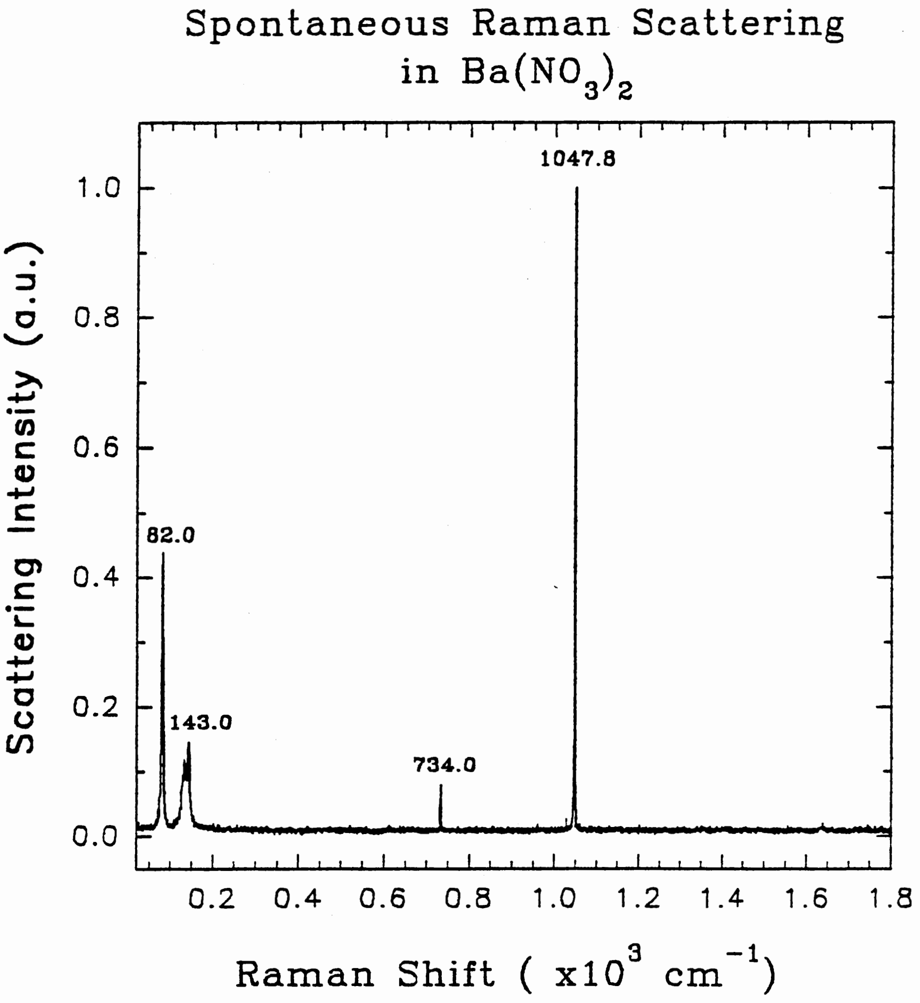

Figure 17. Spontaneous Raman spectra of $Ba(NO_3)_2$. The sharp, intense mode at $1047.8cm^{-1}$ is the totally symmetric mode of vibration responsible for the majority of the Raman shifting. This spectra was measued at the OSU micro-Raman facility by Patricia Watson and Dr. J. Wicksted.

responsible for energy transfer between pump and Stokes beams and to maintain the analogy with the description of SHG and OPO presented earlier.

A Raman active medium is able to couple frequencies that differ by the frequency of the molecular vibration. As shown in Fig.18 below, which corresponds to the more familiar quantum mechanical interpretation of Raman scattering in which the energy absorbed (or released) by the molecule is the difference in energy between the absorbed pump (emitted anti-Stokes) photon and the emitted Stokes (absorbed pump) photons.

The polarization of the medium can be calculated from the molecular polarizability α:

$$\vec{P} = \rho_n \alpha \vec{E} \tag{173}$$

where ρ_n is the density of the molecules. It is not difficult to see that in the presence of intra–molecular vibrations, the polarizability α will be a function of the inter–atomic distances in the vibrating molecule. Assuming these vibrations to be a small perturbation on α, we can approximate the functional form as a Taylor series expansion about the equilibrium position, i.e.

$$\alpha = \alpha_o + \left(\frac{\partial \alpha}{\partial q}\right)_o q + ..., \tag{174}$$

where q is the generalized coordinate attached to the molecular vibration. The first term in Eq.174 gives the linear polarization and the second gives the lowest order correction term responsible for coupling energy between electromagnetic waves and molecular vibrations and also among electromagnetic waves of different frequency.

The molecules can be considered to behave like damped harmonic oscillators with fundamental frequency ω_ν and damping constant Γ. The vibrational wave, build-up out of the individual molecular vibrations, is described by the wave equation

$$\frac{\partial^2 q}{\partial t^2} + v_\nu^2 \nabla^2 q + \omega_\nu^2 q + 2\Gamma \frac{\partial q}{\partial t} = \frac{F}{m} \tag{175}$$

where m is the reduced mass of a molecule participating in the creation of the vibronic mode and v_ν is the group velocity of the vibrational wave. The force F

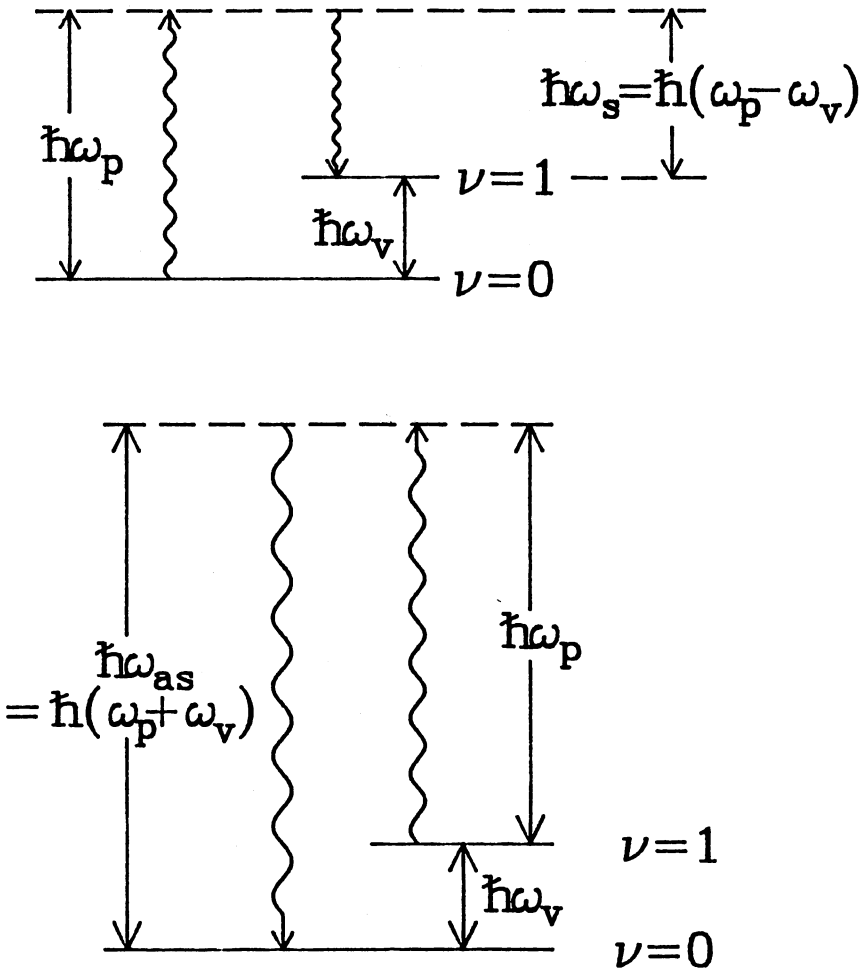

Figure 18. In the case of Stokes radiation a photon of energy $\hbar\omega_p$ is absorbed by an atomic system raising the system to a higher state of energy. The system then interacts with its environment, relaxing down to the ground state with the rease of a phonon of energy $\hbar\omega_v$ and a photon of energy $\hbar(\omega_p - \omega_v)$.

is due to the electric field acting on the molecular dipole moment $\vec{p}$. Using the definition of polarizability $\vec{p} = \alpha\vec{E}$ and Eq.173, we obtain

$$\begin{aligned} \vec{F} &= \tfrac{\partial}{\partial q}\left(\vec{p}\cdot\vec{E}\right) \\ &= \left(\vec{E}\cdot\vec{E}\right)\tfrac{\partial}{\partial q}\left[\alpha_o + \left(\tfrac{\partial\alpha}{\partial q}\right)_o \alpha + ...\right] \\ &\simeq \left(\tfrac{\partial\alpha}{\partial q}\right)_o \left(\vec{E}\cdot\vec{E}\right). \end{aligned} \tag{176}$$

Now if we consider the total field as being composed of the two co–propagating pump and Stokes waves with frequencies differing by the vibrational frequency of the Raman active medium, then we obtain for the electric field

$$\vec{E} = \frac{1}{2}\left[E_p(z,t)e^{i(k_p z-\omega_p t)} + E_s(z,t)e^{i(k_s z-\omega_s t)}\right]\hat{e}_x \tag{177}$$

where $E_p(z,t)$ and $E_s(z,t)$ are the complex amplitudes of the pump and Stokes waves, respectively, and $\hat{e}_x$ is a unit vector in the x direction. We have assumed that the waves have the same liner polarization. We have not included higher order Stokes or anti–Stokes components because their effects can often be considered separately.

The electric field components of Eq.177 produce a beat wave at the molecular vibration frequency ω_ν, with a wave vector of magnitude $k_\nu = k_p - k_s$. This beat wave acts to excite the Raman active vibronic modes in the molecules. These vibrations of the molecules build up into a collective vibration wave described by Eq.175 which has an assumed solution

$$q = \frac{1}{2}q_\nu(z,t)\,e^{i(k_\nu z-\omega_\nu t)} + c.c. \tag{178}$$

where

$$\begin{aligned} k_\nu &= k_p - k_s \\ \omega_\nu &= \omega_p - \omega_s \end{aligned} \tag{179}$$

and $q_\nu(z,t)$ is the complex amplitude of the collective vibration wave. In the quantum-mechanical treatment, the vibration wave is quantitized and it can be described by using the concept of an optical phonon that has a wave vector $\vec{k}_\nu$.

The polarization of the medium can be found by substituting Eqs.174, 177 and 178 into Eq.173, i.e.

$$\vec{P} \simeq \frac{\rho_n}{2}\left[\alpha_o + \left(\frac{\partial\alpha}{\partial q}\right)_o q\right]\left[E_p e^{i\varphi_p} + E_p^* e^{-i\varphi_p} + E_s e^{i\varphi_s} + E_s^* e^{-i\varphi_s}\right] \tag{180}$$

where

$$\varphi_j = k_j z - \omega_j t.$$

Expanding Eq.180 and keeping only the terms containing the phase of the pump and first Stokes fields we find the driving polarization to be

$$\begin{aligned} \vec{P} &\simeq \tfrac{\rho_n}{2}\left[\alpha_o E_p + q_\nu E_s\left(\tfrac{\partial\alpha}{\partial q}\right)_o\right] e^{i\varphi_p} + c.c. \\ &+ \tfrac{\rho_n}{2}\left[\alpha_o E_s + q_\nu^* E_p\left(\tfrac{\partial\alpha}{\partial q}\right)_o\right] e^{i\varphi_s} + c.c. \end{aligned} \tag{181}$$

This polarization can now be substituted into Eq.47 as the source term. This results in a set of coupled partial differential equations

$$\frac{\partial E_p}{\partial z} + \frac{1}{v_p}\frac{\partial E_p}{\partial t} = i\,\frac{v_p\omega_p}{v_s\omega_s}\,\kappa_1 q_\nu E_s. \tag{182}$$

$$\frac{\partial E_s}{\partial z} + \frac{1}{v_s}\frac{\partial E_s}{\partial t} = i\,\kappa_1 q_\nu^* E_p \tag{183}$$

where

$$\kappa_1 = \frac{\mu_o \rho_n v_s \omega_s}{4}\left(\frac{\partial\alpha}{\partial q}\right)_o. \tag{184}$$

and where v_p and v_s are the phase velocities of the pump and the Stokes waves, respectively. Note that the slowly varying amplitude approximation was used when deriving Eq.47. In this approximation, it is assumed that the relative change of amplitude during one optical oscillation period is vanishingly small.

Equations 182 and 183 are strictly valid only for a non-dispersive medium or for truly monochromatic (unphysical) waves because it is assumed implicitly in the derivation of Eq.47 that the permittivity ϵ not be a function of the wavelength. However, it is a very good approximation for most cases in practice. With an accurate, more elaborate derivation that takes finite line widths of the pump and the Stokes waves, the phase velocities ν_p and ν_s on the left-hand sides of Eqs.182 and 183 are replaced by the group velocities u_p and u_s respectively [21].

Using Eqs.177 and 178, the equation for the vibration-wave amplitude can be derived from Eq.175 by applying again the slowly varying amplitude approximation:

$$\frac{dq_\nu}{dt} - v_\nu \frac{dq_\nu}{dz} + \Gamma q_\nu = i\,\kappa_2\,E_p\,E_s^* \tag{185}$$

where

$$\kappa_2 = \frac{1}{2m\omega_\nu}\left(\frac{\partial\alpha}{\partial q_o}\right). \tag{186}$$

We now have obtained a set of three coupled partial differential equations constituted by Eqs.182, 183 and 185. These equations can be reduced to a set of coupled ordinary differential equations by making the transformation into the retarded coordinate system. This system of coordinates is defined stationary in the frame of the travelling waves. If we assume the medium to be dispersionless over the range of frequencies ω_p to ω_s then $v = v_p = v_s$. Here we will note that v_ν is ordinarily small compared to v_p, v_s (typical values are $v_\nu \sim 10^{-10}c$). The transformation is therefore defined by

$$\begin{aligned} z' &= z \\ t' &= t - \tfrac{z}{v} \end{aligned} \tag{187}$$

which along with the approximation that $v_\nu \ll v_p$, v_s leads to the set of coupled equations:

$$\frac{dq_\nu}{dt'} + \Gamma q_\nu = i\,\kappa_2\,E_s^*\,E_p(t'), \tag{188}$$

$$\frac{\partial E_p}{\partial z'} = i\frac{\omega_p}{\omega_s}\,\kappa_1\,q_\nu\,E_s(t'), \tag{189}$$

$$\frac{\partial E_s}{\partial z'} = i\,\kappa_1\,q_\nu^*\,E_p(t'). \tag{190}$$

Steady–State

The set of equations 188, 189 and 190 can readily be solved in the steady-state limit. The steady–state is obtained when the excitation pulse duration τ_p is much larger than the damping or dephasing time of the optical phonon wave $\tau_\nu = \Gamma^{-1}$, i.e. in the limit that $\tau_p \gg \tau_\nu$. In this limit, Eq.188 becomes

$$q_{\nu_{ss}} = i\frac{\kappa_2 E_p E_s^*}{\Gamma}. \tag{191}$$

Substituting Eq.191 into Eqs.189 and 190, we find in the steady-state,

$$\frac{\partial E_{p_{ss}}}{\partial z'} = -\frac{\omega_p}{\omega_s}\frac{\kappa_1\kappa_2\left|E_s\right|^2 E_p}{\Gamma} \tag{192}$$

$$\frac{\partial E_{s_{ss}}}{\partial z'} = \frac{\kappa_1\kappa_2\left|E_p\right|^2 E_s}{\Gamma}. \tag{193}$$

Having eliminated the vibrational wave coordinate from these equations, we can write the right–hand sides of Eqs.192 and 193 in terms of the third order nonlinear polarizations

$$P_{p_{ss}} = \epsilon_o\, \chi^{(3)}_{Raman}(\omega_p; -\omega_s, \omega_s, \omega_p)\ \left|E_s\right|^2\ E_p \tag{194}$$

where

$$\chi^{(3)}_{Raman}(\omega_p; -\omega_s, \omega_s, \omega_p) = i\,\frac{\rho_n}{4\epsilon_o m\omega_p}\frac{v_s}{v_p}\left(\frac{\partial\alpha}{\partial q}\right)^2_o\frac{1}{\Gamma} \tag{195}$$

and

$$P_{s_{ss}} = \epsilon_o\, \chi^{(3)}_{Raman}(\omega_s; -\omega_p, \omega_p, \omega_s)\ \left|E_p\right|^2\ E_s \tag{196}$$

where

$$\chi^{(3)}_{Raman}(\omega_s; -\omega_p, \omega_p, \omega_s) \ = -\ i\,\frac{\rho_n}{4\epsilon_o m\omega_\nu}\left(\frac{\partial\alpha}{\partial q}\right)^2_o\frac{1}{\Gamma}. \tag{197}$$

Therefore, SRS is, in essence, a $\chi^{(3)}$ effect, i.e. resulting from a third order nonlinear polarization.

Equations 192 and 193 can be solved by utilizing the definitions of the pump and Stokes beam intensities

$$I_p = \frac{v\epsilon_o}{2}\left|E_p\right|^2,\ I_s = \frac{v\epsilon_o}{2}\left|E_s\right|^2. \tag{198}$$

Substituting 198 into 192 and 193 we find, using $\frac{\partial I_p}{\partial z} = v\epsilon_o E_p^*\frac{dE_p}{dz}$ and $\frac{\partial I_s}{\partial z} = v\epsilon_o E_s^*\frac{dE_s}{dz}$, the equations

$$\frac{dI_{p_{ss}}}{dz'} = -\left(\frac{\omega_p}{\omega_s}\right)\gamma_{ss}I_{s_{ss}}I_{p_{ss}} \tag{199}$$

and

$$\frac{dI_{s_{ss}}}{dz'} = \gamma_{ss}I_{p_{ss}}I_{s_{ss}} \tag{200}$$

where

$$\gamma_{ss} = \frac{\rho_n\omega_s}{v^2\epsilon_o\epsilon\Gamma\omega_\nu m}\left(\frac{\partial\alpha}{\partial q}\right)^2_o. \tag{201}$$

Equation 201 relates the steady-state gain coefficient γ_{ss} to quantities like the derivative of the polarizability with respect to the generalized coordinate, $\left(\frac{\partial\alpha}{\partial q}\right)_o$, which are not easily measured. The steady-state gain coefficient γ_{ss} can, however, be calculated using the spontaneous Raman scattering cross-section $\left(\frac{\partial\sigma}{\partial\Omega}\right)$, which can be measured directly.

Utilizing Bose-Einstein statistics, the probability of stimulated Raman scattering, w_{st}, to a Stokes mode in which there are already ξ photons is $\xi + 1$ times higher than spontaneous scattering, w_{sp}, to that same mode [62], i.e.

$$w_{st} = (\xi + 1)w_{sp}. \tag{202}$$

From Fig.19 we see that the spontaneously scattered power of dW_{sp} from an infinitesimal volume of scatter dV into a solid angle $\Delta\Omega$, can be calculated from the formula

$$dW_{sp} = I_p\rho_n\left(\frac{\partial\sigma}{\partial\Omega}\right)dV\,\Delta\Omega. \tag{203}$$

Using $dV = Adz$ and $W_p = I_pA$, we get a differential equation for spontaneously scattered power

$$\frac{dW_{sp}}{dz} = W_p\rho_n\left(\frac{\partial\sigma}{\partial\Omega}\right)\Delta\Omega\,. \tag{204}$$

Calculating the average number of photons per mode ξ, in solid angle $\Delta\Omega$, we can now get an equation for the stimulated scattered power W_{st}. Assuming that the line shape of the Raman scatterer, as a function of frequency, is a top-hat profile, we get an expression for ξ

$$\xi = \frac{I_s\lambda_s^2}{\Delta\Omega\,h\nu_s\Delta\nu_R} \tag{205}$$

where ν_s is the Stokes beam frequency. The mode density of one polarization only is taken into account because of the assumption that Raman scattering can couple only waves of the same polarization.

For large Stokes population, i.e. $\xi \gg 1$, we find from Eqs.202, 204 and 205 the differential equation

$$\frac{dW_{sp}}{dz} = \frac{\rho_n\lambda_s^2}{h\nu_s\Delta\nu_R}\left(\frac{\partial\sigma}{\partial\Omega}\right)I_sW_p. \tag{206}$$

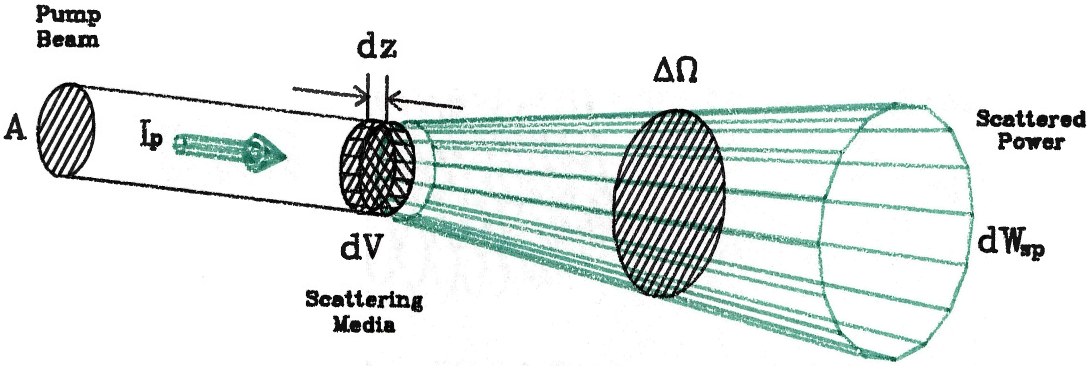

Figure 19. Geometry for spontaneous Raman scattering: A pump beam with cross-sectional area A interacts with a differential scattering volume $dV = A\,dz$ to scatter the differential power dW_{sp} into a solid angle of $\Delta\Omega$.

This expression gives the total stimulated scattered power integrated over all wavelengths under the assumption of the top–hat line shape profile. When the effects of other line shapes are taken into account, the factor $\frac{1}{\Delta\nu_R}$ in Eq.205 must be replaced by the normalized line-shape function $s(\nu)$.

Comparing Eqs.199 and 206 gives the expression

$$\gamma(\nu) = \frac{\rho_n \lambda_s^2}{h\nu_s} s(\nu) \left(\frac{\partial\sigma}{\partial\Omega}\right). \tag{207}$$

In the case of a Lorentzian line shape profile

$$s(\nu) = \left(\frac{2}{\pi}\right) \frac{\Delta\nu_R}{\Delta\nu_R^2 + (\nu - \nu_s)^2} \tag{208}$$

the peak value of the line shape function is $\frac{2}{\pi\Delta\nu_R}$, where $\Delta\nu_R$ is the full width at half-maximum.

The differential equations 199 and 200 describe the amplification of the Stokes beam and the depletion of the pump beam as they co-propagate in the steady-state regime. The first integral for these coupled equations can be found by considering that in Raman scattering the number of photons is conserved. That is the quantity

$$I_o = I_p(z') + \frac{\omega_p}{\omega_s} I_s(z') \tag{209}$$

must remain constant. This can be verified by differentiating Eq.209 to find

$$\frac{dI_{p_{ss}}}{dz'} = -\frac{\omega_p}{\omega_s}\frac{dI_{s_{ss}}}{dz'}. \tag{210}$$

Upon comparison of Eq.210 with Eqs.199 and 200, we find an identity.

Utilizing Eq.209 we find, using Eqs.199 and 200

$$\begin{aligned} \frac{1}{I_{s_{ss}}}\frac{dI_{s_{ss}}}{dz'} - \frac{1}{I_{p_{ss}}}\frac{dI_{p_{ss}}}{dz'} &= \gamma_{ss}\left(I_{p_{ss}} + \frac{\omega_p}{\omega_s} I_{s_{ss}}\right) \\ &= \gamma_{ss} I_o \end{aligned} \tag{211}$$

which can be integrated to give

$$\frac{I_s(z')I_p(0)}{I_s(0)} = I_p(z')\, e^{\gamma_{ss} I_o z'}. \tag{212}$$

Eliminating $I_{p_{ss}}(z')$ in favor of $I_{s_{ss}}(z')$ and using Eq.209, we find the steady-state growth in the $1^{\underline{st}}$ Stokes intensity to be

$$I_{s_{ss}}(z') = I_o \, \frac{\left(\frac{I_{s_{ss}}(0)}{I_{p_{ss}}(0)}\right) \, e^{\gamma_{ss} I_o z'}}{1 + \frac{\omega_p}{\omega_s}\left(\frac{I_{s_{ss}}(0)}{I_{p_{ss}}(0)}\right) \, e^{\gamma_{ss} I_o z'}} . \tag{213}$$

It must be emphasized that because the pump and Stokes beam are co-propagating, the relative timing of the beams does not change and so each individual time element of the Stokes pulse has a fixed corresponding element of the pump pulse that determines its amplification.

The energy conservation efficiency is defined as

$$\eta = \frac{I_s(L) - I_s(0)}{I_p(0)} , \tag{214}$$

where L is the length of the amplifying medium. Figure 20 shows a plot of η evaluated from Eq.212 as a function of $\gamma_{ss} I_o L$. We used three values of the Stokes beam initial intensity and applied the good approximation that $\omega_p/\omega_s \simeq 1$. As can be seen from Eq.212, the Stokes beam grows exponentially when the intensity is small compared with the pump beam and then saturates with larger intensities.

Transient

In order to determine the transient behavior of SRS, the first term (the transient) in Eq.188 must remain. The simultaneous solution of Eqs.188, 189, and 190 require more advanced methods than was used for the steady–state solution.

We start by differentiating Eq.188 with respect to z' to obtain

$$\frac{\partial^2 q_\nu}{\partial z' \partial t'} + \Gamma \frac{\partial q_\nu}{\partial z'} = i \, \kappa_2 E_p(t') \frac{\partial E_s^*}{\partial z'} . \tag{215}$$

Substituting Eq.190 in for $\partial E_s^* / \partial z'$, we find

$$\frac{\partial^2 q_\nu}{\partial z' \partial t'} + \Gamma \frac{\partial q_\nu}{\partial z'} - \kappa_1 \, \kappa_2 \left| E_p(t') \right|^2 q_\nu = 0 . \tag{216}$$

Likewise, differentiating $E_s / E_p(t')$ with respect to t' in Eq.190, we find

$$\frac{\partial^2}{\partial t' \partial z'} \left(\frac{E_s}{E_p(t')} \right) = i \, \kappa_1 \frac{\partial q_\nu^*}{\partial t'} . \tag{217}$$

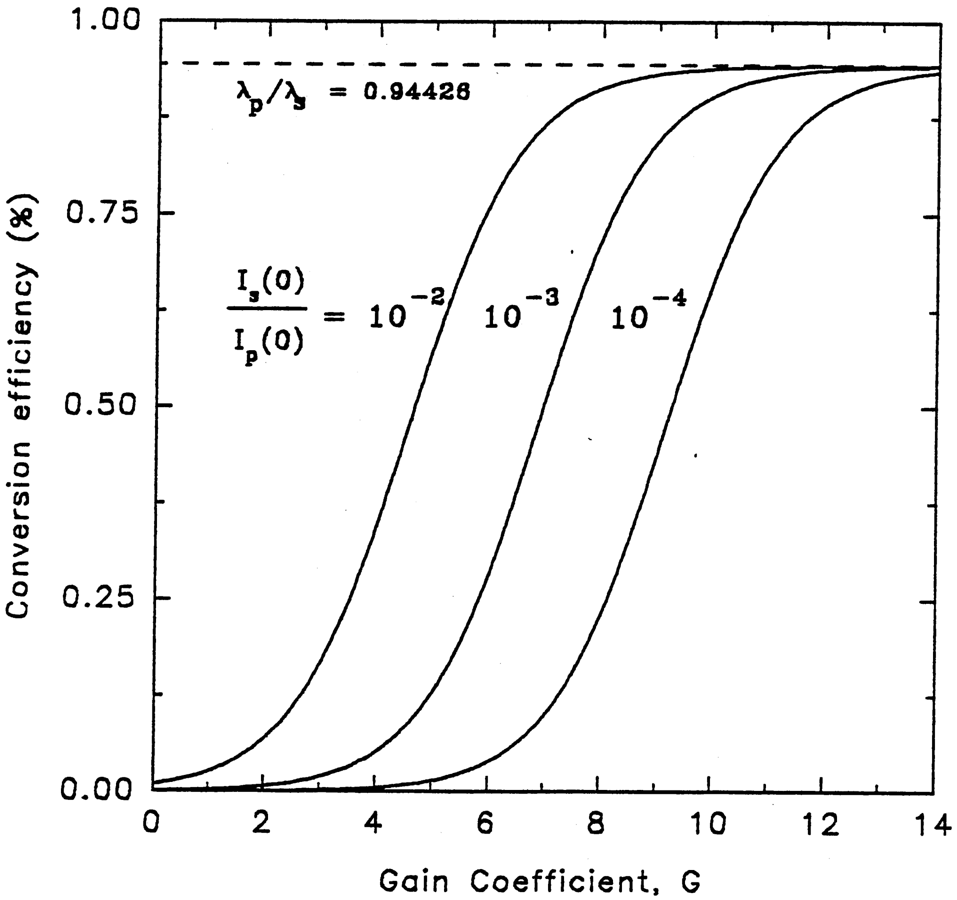

Figure 20. SRS conversion efficiency for various values of $\frac{I_s(0)}{I_p(0)}$, the ratio of the incident Stokes to pump intensity, as predicted by Eq.212.

Substituting Eq.188 in for $\partial q_v^*/\partial t'$ we find

$$\frac{\partial^2}{\partial t'\partial z'}\left(\frac{E_s}{E_p(t')}\right)+\Gamma\frac{\partial}{\partial z'}\left(\frac{E_s}{E_p(t')}\right)-\kappa_1\kappa_2\left|E_p(t')\right|^2\left(\frac{E_s}{E_p(t')}\right)=0. \tag{218}$$

Equations 216 and 218 are both of the same form obeying the same second-order hyperbolic partial differential equation,

$$\frac{\partial^2 F}{\partial t'\partial z'}+\Gamma\frac{\partial F}{\partial z'}-\kappa_1\kappa_2\left|E_p(t')\right|^2 F=0 \tag{219}$$

where F stands for either q_ν or $E_s/E_p(t')$. With the substitution of $F=U\,e^{-\Gamma t'}$, this equation takes the reduced form

$$\frac{\partial^2 U}{\partial t'\partial z'}-\kappa_1\kappa_2\left|E_p(t')\right|^2 U=0. \tag{220}$$

This equation can be further reduced to an equation with constant coefficients by a transformation into a new variable τ defined by

$$\tau=\int_{-\infty}^{t'}\left|E_p(t'')\right|^2 dt'' \tag{221}$$

or

$$\frac{d\tau}{dt'}=\left|E_p(t')\right|^2.$$

It can be seen that τ is a measure of the accumulation of energy in the laser pulse up to time t'. Utilizing this transformation we find

$$\frac{\partial^2 U}{\partial z'\partial t'}\left(\frac{d\tau}{dt'}\right)-\kappa_1\kappa_2\left(\frac{d\tau}{dt'}\right)U=0,$$

or

$$\frac{\partial^2 U}{\partial z'\partial \tau}-\kappa_1\kappa_2 U=0 \tag{222}$$

which is in the form of a standard hyperbolic equation.

Equation 222 may be solved for arbitrary initial conditions using Riemann's method as follows [65].

The solution of a second-order hyperbolic-type equation

$$\mathcal{L}=\frac{\partial^2 U}{\partial z'\partial \tau}+aU=0, \tag{223}$$

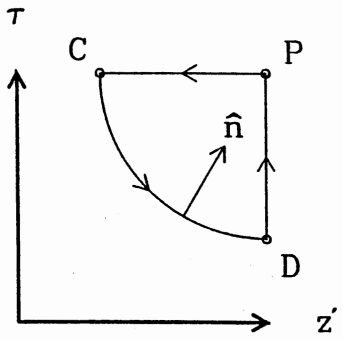

Figure 21. General form of the contour of Riemann's integration. After Wang [64].

with constant coefficient $a = -\kappa_1\kappa_2$ can be obtained by using the adjoint equation

$$\mathcal{M} = \frac{\partial^2 V}{\partial z' \partial \tau} + aV = 0. \tag{224}$$

Consider the region $\mathcal{S}$ in which $\mathcal{L}(U) = 0$ and $\mathcal{M}(V) = 0$. We have

$$\begin{aligned} \iint_S \left[V\mathcal{L}(U) - U\mathcal{M}(V)\right] dz'd\tau &= \iint_S \left[V\tfrac{\partial^2 U}{\partial z'\partial \tau} - U\tfrac{\partial^2 V}{\partial z'\partial \tau}\right] dz'd\tau \\ &= \tfrac{1}{2}\iint_S \left[\tfrac{\partial}{\partial z'}\left(V\tfrac{\partial U}{\partial \tau} - U\tfrac{\partial V}{\partial \tau}\right)\right] dz'd\tau \\ &\quad + \tfrac{1}{2}\iint_S \left[\tfrac{\partial}{\partial \tau}\left(V\tfrac{\partial U}{\partial z'} - U\tfrac{\partial V}{\partial z'}\right)\right] dz'd\tau \\ &= \iint_S \left(\tfrac{\partial A}{\partial z'} + \tfrac{\partial B}{\partial \tau}\right) dz'd\tau \end{aligned}$$

or

$$\iint_{S} \left[V\mathcal{L}(U) - U\mathcal{M}(V)\right] dz'd\tau = \oint_C \left(Ad\tau + Bdz'\right) \tag{225}$$

where

$$\begin{aligned} A &= \tfrac{1}{2}\left(V\tfrac{\partial U}{\partial \tau} - U\tfrac{\partial V}{\partial \tau}\right) \\ B &= \tfrac{1}{2}\left(V\tfrac{\partial U}{\partial z'} - U\tfrac{\partial V}{\partial z'}\right). \end{aligned} \tag{226}$$

Taking $\mathcal{S}$ to be an area $PCDP$ with $PC \parallel z'$ axis and $PD \parallel \tau$ axis as shown in Fig.21, then the integral in Eq.225 becomes

$$\oint \left(Ad\tau - Bdz'\right) = \int_D^P Ad\tau - \int_p^C Bdz' + \int_C^D \left(Ad\tau - Bdz'\right) = 0. \tag{227}$$

Evaluating these integrals separately, we find

$$\int_p^C Bdz' = \frac{1}{2}(VU)_C - \frac{1}{2}(VU)_P - \int_P^C U\frac{\partial V}{\partial z'}dz' \tag{228}$$

and

$$\int_D^P A d\tau = -\frac{1}{2}(VU)_D + \frac{1}{2}(VU)_P + \int_P^D U\frac{\partial V}{\partial \tau} d\tau \tag{229}$$

Using these results, Eq.227 becomes

$$\begin{aligned}(VU)_P \; = \; & \tfrac{1}{2}(VU)_C + \tfrac{1}{2}(VU)_D - \textstyle\int_C^D \left(Ad\tau - Bdz'\right) \\ & - \textstyle\int_P^C U\frac{\partial V}{\partial z'}dz' - \int_P^D U\frac{\partial V}{\partial \tau}d\tau.\end{aligned} \tag{230}$$

If we choose a solution of the adjoint Eq.224 which satisfies the boundary conditions,

$$\begin{aligned} V_P \; &= \; 1 \\ \tfrac{\partial V}{\partial z'} \; &= \; 0 \;\; \text{along } PC, \\ \tfrac{\partial V}{\partial \tau} \; &= \; 0 \;\; \text{along } PD, \end{aligned} \tag{231}$$

then we have the solution of Eq.223 as, given by

$$U_P = \frac{1}{2}(VU)_C + \frac{1}{2}(VU)_D - \int_C^D \left(Ad\tau - Bdz'\right) \tag{232}$$

which can also be written as

$$U_P = \frac{1}{2}(VU)_C + \frac{1}{2}(VU)_D - \int_C^D \left(V\, D_n U - U\, D_n V\right) ds, \tag{233}$$

with

$$D_n = \frac{1}{2}\cos(\hat{n}, z')\frac{\partial}{\partial \tau} + \frac{1}{2}\cos(\hat{n}, \tau)\frac{\partial}{\partial z'} \, ,$$

where ds is the differential along the curve CD, and $\hat{n}$ is the inner normal to the curve.

The curve CD must therefore be chosen according to the available boundary conditions of Eq.223. The function of V which satisfies Eqs.225 and 231 is called Riemann's function.

The Riemann's function is found by taking, as the special solution for Eq.223, the Bessel function of imaginary argument, i.e.

$$V(z', \tau) \equiv I_o\left\{2\sqrt{\kappa_1 \kappa_2 \tau\, z'}\right\} \, . \tag{234}$$

We can now customize the path CD to fit the situation at hand by choosing the path as shown in Fig.22. The reason for choosing this path will become obvious

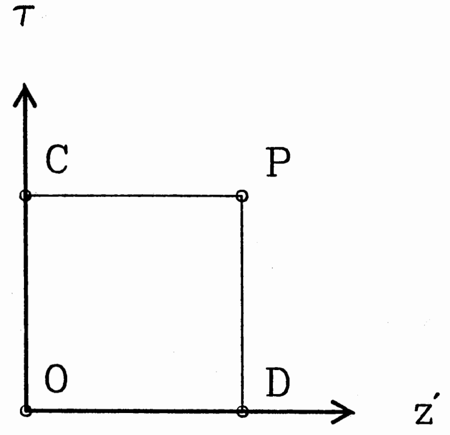

Figure 22. Contour for Riemann integration.

in the development of the solution.

The last term in Eq.233 must now be broken up into two integrals: one along path CD and the other along OD. The factor D_n and differential line element ds for both paths are given by

$$\begin{aligned} CO : D_n &= \tfrac{1}{2}\tfrac{\partial}{\partial \tau}\,,\ ds = -d\tau \\ OD : D_n &= \tfrac{1}{2}\tfrac{\partial}{\partial z'}\,,\ ds = dz'. \end{aligned} \tag{235}$$

Substituting these into the last term in Eq.233 we find

$$\begin{aligned} \textstyle\int_C^D (V\,D_nU - U\,D_nV)\,ds = {} & -\tfrac{1}{2}\,(VU)_O + \tfrac{1}{2}\,(UV)_D \\ & + \textstyle\int_C^O U\,\frac{\partial V}{\partial \tau}\,d\tau + \int_O^D V\,\frac{\partial U}{\partial z'}\,dz'\,. \end{aligned} \tag{236}$$

Substituting Eq.236 back into Eq.233, we find the solution

$$U_P = (VU)_C + \int_C^O U\frac{\partial V}{\partial \tau}d\tau + \int_O^D V\frac{\partial U}{\partial z'}dz'\,. \tag{237}$$

The points P, C, O and D correspond to the coordinates (z', τ), $(0, \tau)$, $(0,0)$ and $(z', 0)$, respectively. Therefore Eq.237 can be written in terms of the coordinates z' and τ as

$$\begin{aligned} U(z', \tau) &= V(0,\tau)U(0,\tau) + \textstyle\int_\tau^0 U(0,\tau')\frac{\partial V(0,\tau')}{\partial \tau'}d\tau' \\ &+ \textstyle\int_0^{z'} V(z'',0)\frac{\partial U(z'',0)}{\partial z''}dz''. \end{aligned} \tag{238}$$

From Eq.234 and the properties of the zero$^{\underline{th}}$ order Bessel function, we note that

$$V(0,\tau) = V(z'',0) = 1\,. \tag{239}$$

Applying the initial condition that no vibrational excitation exist at the beginning of the laser pulse, we find

$$\lim_{t' \to \infty} \left\{ \frac{\partial E_s}{\partial z'} = q_\nu(z') \right\} = 0 \tag{240}$$

therefore $U(z', 0) = 0$.

Substituting Eqs.239 and 240 into Eq.238, we find the simplified expression

$$U(z', \tau) = U(0, \tau) + \int_\tau^0 U(0, \tau') \frac{\partial V(0, \tau')}{\partial \tau'} d\tau'. \tag{241}$$

Changing the variable of integration from τ back to t', using Eq.221, and substituting in for U in relation to F, we find for the two values of F the integral equations

$$\begin{aligned} E_s(z, t') &= E_s(0, t') + \\ &E_p(t') \int_{-\infty}^{t'} e^{-\Gamma(t'-t'')} E_p^*(t'') E_s(0, t'') \frac{I_1\left\{2\sqrt{\kappa_1 \kappa_2\, z' \left[\tau(t') - \tau(t'')\right]}\right\}}{\sqrt{\tau(t') - \tau(t'')}} dt'' \end{aligned} \tag{242}$$

and

$$q_\nu^* = i\,\kappa_1 \int_{-\infty}^{t'} e^{-\Gamma(t'-t'')} E_p^*(t'') E_s(0, t'') I_o \left\{2\sqrt{\kappa_1 \kappa_2\, z' \left[\tau(t') - \tau(t'')\right]}\right\} dt'' \tag{243}$$

where we have used the recursion relation, $I_o' = I_1$.

We will first examine the Raman amplitude $E_s(z, t')$ in Eq.242 of a fixed point z for the case where the laser–pulse width τ_p is shorter than $\tau_\nu = \Gamma^{-1}$. The first term is the input value and can be neglected in the high-gain region. The second term contains the integral and represents the increment in the Stokes amplitude. Now, the integral is zero at the front edge of the laser and rapidly increases while the main part of the laser pulse is passing through the medium. In the tail of the laser pulse, the integral varies much more slowly and gradually decreases as $e^{-\Gamma t'}$ as shown in Fig.23. Except for the initial stages at the beginning of the laser pulse, the amplitude of the molecular vibrations q_ν is given by the integral in Eq.243, and behaves in a similar manner. Therefore, both the vibration q_ν and the Stokes pulse E_s amplitudes rise rapidly when the laser is about at its peak. The peak of the

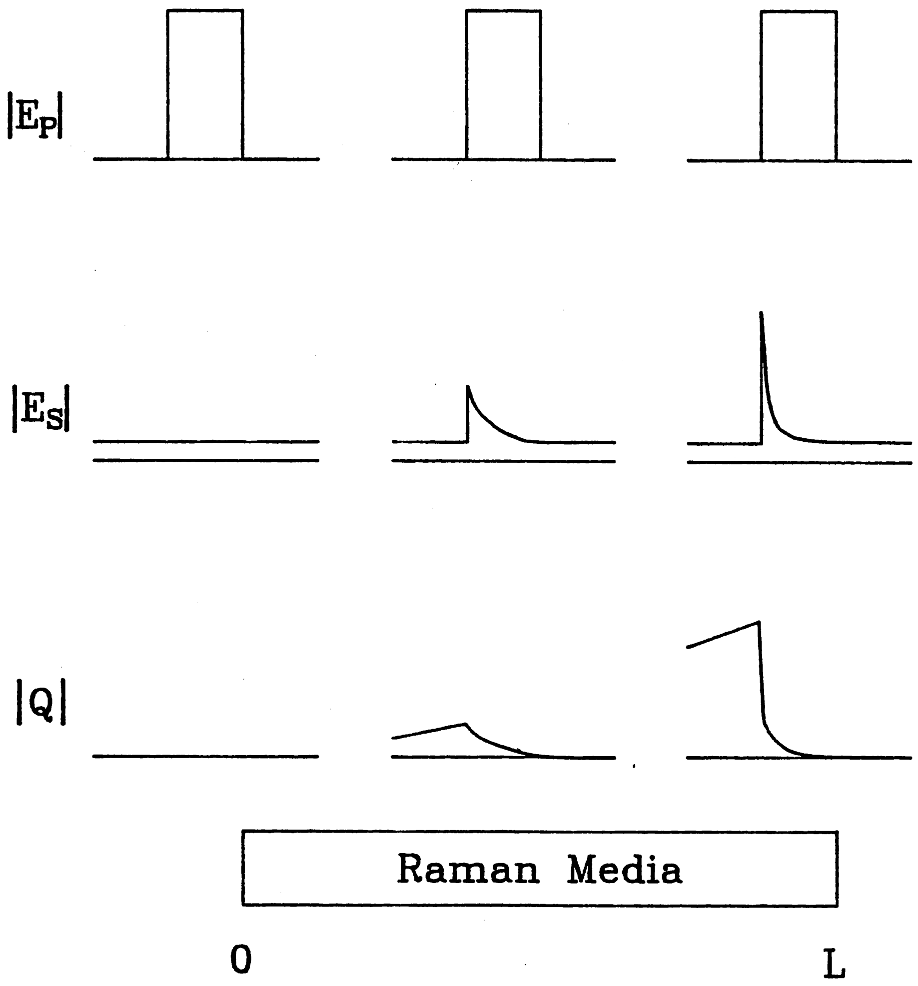

Figure 23. Schematic diagram of the growth and decay of transient SRS field amplitudes. The The first column shows a top-hat pump field amplitude incident the Raman media. The Stokes field amplitude is shown to have a non-zero initial value. The second column shows the intial transient response of the Stokes and phonon field to the pumping field. The transient growth of the Stokes field is much more rapid then the growth of the phonon field since it is proportional the magnitude of the pump field, and hence displays an instantaneous response to the pumping field; whereas the phonon field relies on the history of the pump field, and therefore grows at a much more gradual pace. The third column shows the rapid decay of the Stokes and phonon fields after the pump starts to exit the Raman media. After Carmen et al. [66].

Raman pulse always comes after the peak of the laser. The vibrational excitation then decays as $e^{-\Gamma t'}$. Since the Stokes amplitude in Eq.242 has an additional dependence on $E_p(t')$, it drops off, closely following the laser-pulse shape in the tail.

Carmen, et al. [66] obtained numerical solutions of Eqs.242 and 243 for several different pulse width and pulse shapes. The central result we wish to extract from their work is the relationship between the transient gain coefficient G_T and the steady-state gain coefficient G_{ss} for a temporally Gaussian laser-pulse shape. The gain coefficient is defined by the relation

$$I_s(L) = I_s(0)\, e^{G} \tag{244}$$

where G is the gain coefficient and I_s is the Stokes intensity. The steady-state gain coefficient is therefore found from Eq.212 to be given by

$$G_{ss} = \gamma_{ss} I_o L. \tag{245}$$

Figure 24 shows the resulting relationship between the transient gain coefficient G_T and the steady–state gain coefficient G_{ss} for Gaussian laser input pulses. It is apparent that for $\tau_p \leq \tau_v$, G_T is smaller that G_{ss}. Hence we should expect a lower conversion efficiency for transient SRS as opposed to SRS in the steady–state regime.

Threshold Conditions

The transient and steady-state threshold intensities can be easily measured and compared to the theory previously developed. However in order to apply the previous relationships we must first define some conventions and make the necessary assumptions to render the solution tractable. We start by identifying that the transient Stokes intensity can be written as

$$I_s(L) = I_s(0)\, e^{G_T},$$

where G_T is determined by the numerical solutions of Carmen et al..

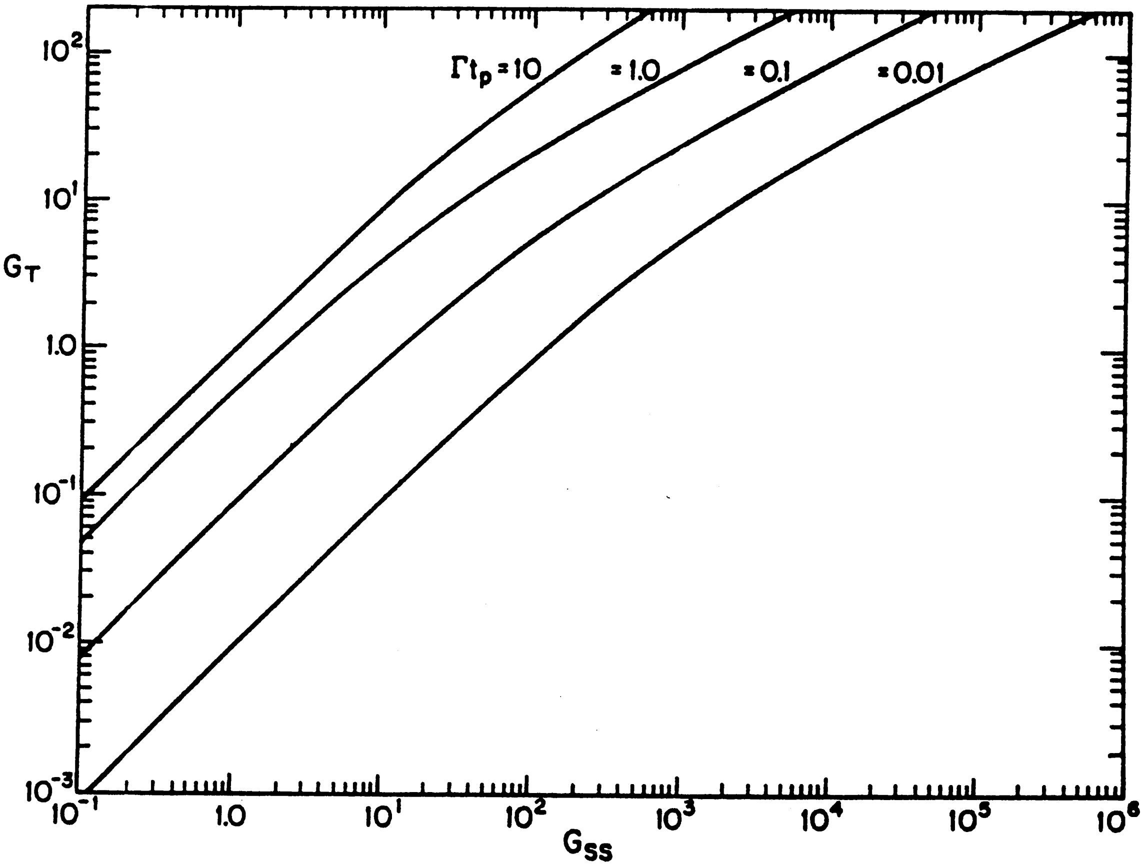

Figure 24. The transient Raman gain coefficient for Gaussian laser input pulses with the same total energy, but different pulse widths. The steady-state gain coefficient G_{ss} corresponds to the constant intensity laser output equal to the maximum laser pulse energy. After Carmen et al. [66].

The threshold condition for both steady–state SRS has been defined as being the point at which 1% of the pump intensity has been converted to Stokes intensity. In order to determine the threshold gain coefficient G_{ss}^{th}, we will examine the derivative of the amplified spontaneous Raman scattered intensity I_s as follows

$$\frac{dI_s}{dz} = \left(\frac{dI_s}{dz}\right)_{sp} + \left(\frac{dI_s}{dz}\right)_{st} \tag{246}$$

where the first term is the spontaneous and the second the stimulated scattering term. The stimulated scattering term is given by Eq.200 and the spontaneous scattering term can be found from Eq.204:

$$\left(\frac{dI_s}{dz}\right)_{sp} = I_p\rho_n \left(\frac{\partial\sigma}{\partial\Omega}\right) \Delta\Omega, \tag{247}$$

where $\Delta\Omega$ is the solid angle of scattering for the photons that stay in the medium throughout the entire amplification length.

Applying Eqs.200, 207, and 247 leads to

$$\frac{dI_s}{dz} = \gamma(\nu)\, I_p \left[\frac{h\nu_s}{\lambda_s^2}\Delta\nu_R\Delta\Omega + I_s\right] \tag{248}$$

where we have replaced the line-shape function $s(\nu)$ by $\frac{1}{\Delta\nu_R}$, assuming a top–hat profile. Because the second term on the right-hand side of Eq.248 is going to be much larger than the first term after a certain interaction length, the solution can be approximated by the exponential function solution of Eq.200, where we can use

$$I_s(0) = \frac{h\nu_s}{\lambda_s^2}\Delta\nu_R\Delta\Omega \tag{249}$$

as the Stokes input intensity. Based on the relation between the probability of spontaneous scattering and stimulated scattering, i.e. $w_{st} = (\xi + 1)\, w_{sp}$, it is easy to see that $I_s(0)$ is actually the intensity of a beam in which all the modes have only one photon.

Substituting Eq.249 into Eq.248 and solving for $I_s(z)$ we find, in the high gain limit

$$I_s(L) = I_s(0)\, e^{G_{ss}}, \tag{250}$$

where $G_{ss} \equiv \gamma_{ss} I_p L$, is the steady-state gain coefficient. The threshold condition can now be found by evaluating Eq.250 for $I_s(L) = 0.01\, I_p(0)$; that is, for the case where 1% of the pump intensity is converted to Stokes intensity. Utilizing Eq.249 to eliminate $I_s(0)$ and evaluating Eq.250 at the threshold condition, we find the steady-state gain coefficient to be

$$G_{ss}^{th} = \ln\left[\frac{(0.01)\, I_p(0)\, \lambda_s^2}{h\, \nu_s\, \Delta\nu_R\, \Delta\Omega}\right] . \tag{251}$$

The transient threshold gain coefficient G_{tr}^{th} can be determined from the value obtained for G_{ss}^{th} by utilizing the numerical solutions that compare G_{ss} to G_{tr}. We will define the factor F as being the factor by which the peak pump intensity must be increased under, transient conditions, as compared to the steady-state [67]. This factor, F, can be calculated given the value of the ratio, $\frac{\tau_p}{\tau_\nu}$, and the value of G_{ss}^{th}.

Higher Order Stokes and Anti–Stokes Components

Up to this point we have only discussed the generation of Stokes radiation. Higher order Stokes and anti-Stokes component output is common in SRS and has been observed and explained in the past [68–71]. We will now address the generation of anti-Stokes, higher order Stokes, and higher order anti-Stokes radiation.

Anti-stokes radiation can be generated parametrically through the coupling of the pump and Stokes radiation. The nonlinear polarization responsible for this coupling is given by

$$P_{as}^{(3)} = \chi_{as}^{(3)}(\omega_{as}\,; \omega_p, \omega_p, -\omega_s)\, E_p E_p E_s^*\, e^{i\left(2\vec{k}_p - \vec{k}_s - \vec{k}_{as}\right)\cdot\vec{r}} \tag{252}$$

where

$$\begin{aligned} \omega_{as} &= \omega_p + \omega_\nu, \\ \vec{k}_{as} &= 2\vec{k}_p - \vec{k}_s. \end{aligned} \tag{253}$$

Similarly higher order Stokes and anti-Stokes can be generated successively through an appropriate third order nonlinear polarization. For example, the second Stokes field, E_{s_2}, can be generated in two ways, i.e.

$$\begin{aligned} P_{s_2}^{(3)} &= \chi_{\alpha s_2}^{(3)}(\omega_{s_2};\omega_{s_1},\omega_{s_1},-\omega_p)\, E_{s_1}E_{s_1}E_p^*\, e^{i\left(2\vec{k}_{s_1}-\vec{k}_p-\vec{k}_{s_2}\right)\cdot\vec{r}} \\ &+ \chi_{\beta s_2}^{(3)}(\omega_{s_2};\omega_p,\omega_{s_1},-\omega_{as_1})\, E_pE_{s_1}E_{as_1}^*\, e^{i\left(\vec{k}_p+\vec{k}_{s_1}-\vec{k}_{as_1}-\vec{k}_{s_2}\right)\cdot\vec{r}} \end{aligned} \tag{254}$$

where

$$\begin{aligned} \omega_{s_2} &= \omega_p - 2\omega_\nu, \\ \vec{k}_{s_2} &= 2\vec{k}_{s_1} - \vec{k}_p, \\ \vec{k}_{s_2} &= \vec{k}_p + \vec{k}_{s_1} - \vec{k}_{as_1}. \end{aligned} \tag{255}$$

The generation of second Stokes is clearly a higher order effect since $P_{s_1}^{(3)}$ and $P_{as_1}^{(3)}$ are proportional to $|E_p|^2$.

When the first Stokes E_{s_1} becomes intense enough E_{s_2} can also be generated through the process.

$$\begin{aligned} P_{s_2}^{(3)} &= \chi_{\gamma s_2}^{(3)}(\omega_{s_2};\omega_{s_1},-\omega_{s_1},\omega_{s_2})\, |E_{s_1}|^2 E_{s_2} \\ &+ \chi_{\delta s_2}^{(3)}(\omega_{s_2};\omega_{s_1},\omega_{s_1},-\omega_{as_2})\, E_{s_1}^2 E_{as_2}^*, \end{aligned} \tag{256}$$

where E_{as_2} is the second anti-Stokes. This process is identical to the SRS of the pump into first Stokes described in Eq.196. Cascading processes, such as this, can continue indefinitely, allowing for the creation of higher and higher orders of Stokes and anti-Stokes radiation. Obviously this cascading process is limited by the initial pump intensity and the efficiency of the first, second, etc., order SRS (since each of the new pumping field intensities must be larger than the threshold intensity for the next higher order SRS process).

The amount of higher order radiation present from cascading is small compared to that from the four-photon processes described in Eqs.252 and 254. The reason is two-fold: First, the driving polarization in both is proportional to the original pump and second, there exists very definite angles at which the polarization is maximized — that is, these processes can be phase matched.

Phase matching in the four-photon processes is achieved by requiring

$$2\vec{k}_p - \vec{k}_{s_1} - \vec{k}_{as_1} = 0 \tag{257}$$

for anti-Stokes generation and

$$2\vec{k}_{s_1} - \vec{k}_p - \vec{k}_{s_2} = 0 \tag{258}$$

or

$$\vec{k}_p + \vec{k}_{s_1} - \vec{k}_{as_1} - \vec{k}_{s_2} = 0$$

for second Stokes generation. The triangles formed by the phase matched wave vectors in the processes are shown in Fig.25.

The general form of the phase matching conditions is given by the relations

$$\vec{k}_o + \vec{k}_{n-1} = \vec{k}_{-1} + \vec{k}_n \tag{259}$$

and

$$\vec{k}_o + \vec{k}_{-1} = \vec{k}_{n-1} + \vec{k}_{-n} \tag{260}$$

where $\vec{k}_o$, $\vec{k}_{-1}$, $\vec{k}_n$, and $\vec{k}_{-n}$ are, respectively, the pump, first Stokes, and the $n^{\underline{th}}$ order anti-Stokes and Stokes waves. These phase matching processes should lead to intense cones of higher order Stokes and anti-Stokes radiation, all centered symmetrically around the pump beam.

The theoretical values for the angles of the $n^{\underline{th}}$ order anti–Stokes and Stokes emission can be found from Eqs.259 and 260 to be given by [69]

$$\theta_{\pm n} = \beta_{\pm n} \pm \sqrt{\beta^2_{\pm n} + \delta_{\pm n} - \gamma_{\pm n}}\ , \tag{261}$$

where

$$\beta_{\pm n} = \frac{k_{n-1}\theta_{n-1}}{k_{-1} \pm k_{\pm n}}\ ,$$

$$\delta_{\pm n} = \left(\frac{2k_{-1}}{\pm k_{\pm n}}\right)\left[\frac{\pm k_{\pm n} + k_{-1} \mp k_o - k_{n-1}}{k_{-1} \pm k_{\pm n}}\right]$$

and

$$\gamma_{\pm n} = \frac{(k_{n-1} - k_{-1})\,\beta_{\pm n}\theta_{n-1}}{k_r}\ .$$

The corresponding angles of first-order Stokes absorption are

$$\theta^{(\pm n)}_{-1} = \frac{k_{n-1}\theta_{n-1} \mp k_{\pm n}\theta_n}{k_{-1}}. \tag{262}$$

These values hold true if the index of refraction seen by each constituent field component is not changed by the presence of intense radiation, i.e. self-focusing. If the medium, happens to displays self-focusing, then the values of k_o, k_{-1}, k_n,

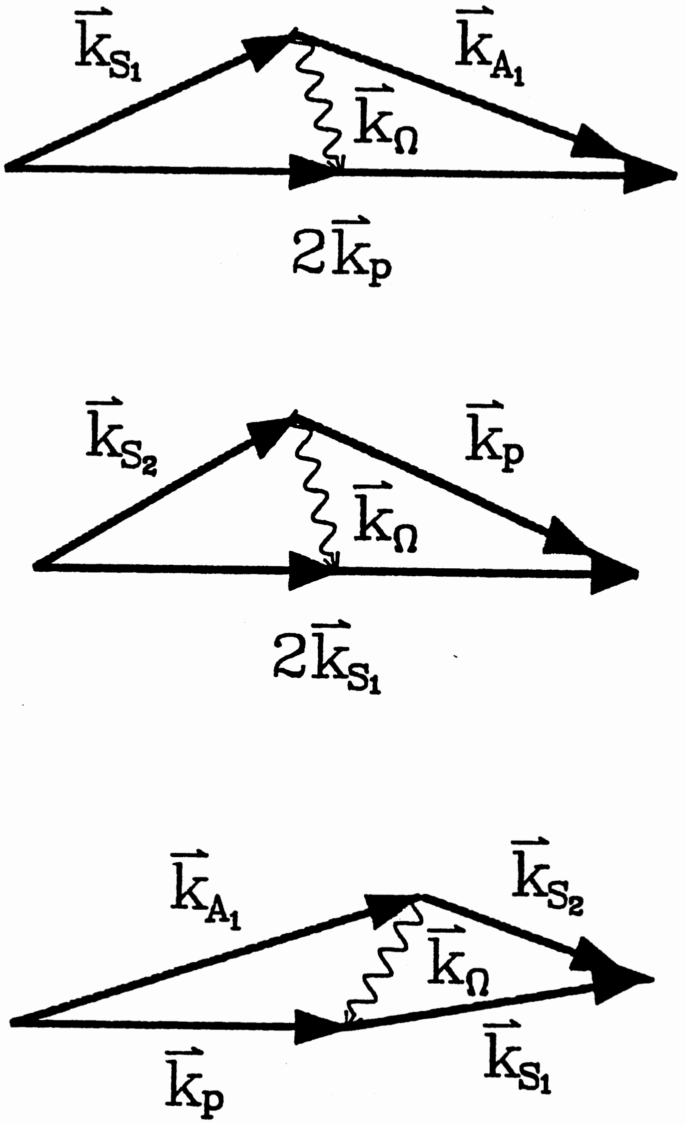

Figure 25. Schematic diagrams for the phase match four-photon processes described by Eqs. 257 and 258.

and k_{-n} are all subject to change. The phase matching conditions, under these circumstances, become rather unpredictable. Radiation that obeys phase matching under these intensity dependent conditions, i.e. radiation whose parameters do not obey Eq.261, is called *Class II* – type radiation. Conversely, radiation whose parameters obey Eq.261 is deemed *Class I* – type radiation.

CHAPTER VII

SHG: EXPERIMENTAL

The crystals under investigation belong to a family of new nonlinear optical materials namely: KTP, KTA, RTA, KRTA, and KCTA where KTP has been used as a standard sample. At the time these experiments were performed, only the refractive index data of KTP was known. Therefore, it was not possible to calculate the proper orientation angles, i.e. phase matching angles, for KTA, RTA, KRTA and KCTA. The essential goal of these experiments was to gather precursory phase matching information for these materials. The primary measurement was to measure the intensity output of the second harmonic against a known phase mismatch. The phase mismatch was manifest as either an angle of incidence variation or a variation in the temperature of the material.

Figure 26 illustrates the basic experimental set-up used for these initial investigations. The pump source used in these investigations was a Q-switched Nd:YAG laser with a pulse width of 10ns, operated at 10Hz over the range of energies 0-150mJ/pulse. A half wave plate was used to rotate the incident polarization into a state which maximized the output, i.e. into a state in which either Type I or Type II phase match was obeyed (c.f. ch.V). The crystals were mounted on a rotation stage with minimum resolution of 0.03^o. The SH output was separated from the fundamental by placing a 45^o 'p'-polarized dichroic mirror in the path of the output beam. The SH output was then monitored and referenced against the input fundamental beam.

Intensity versus angular phase mismatch measurements for the various crystals are shown in the figures below. Figure 27 shows the behavior for the Type I and Type II phase matched KTP reference crystals. Both of these curves bear a

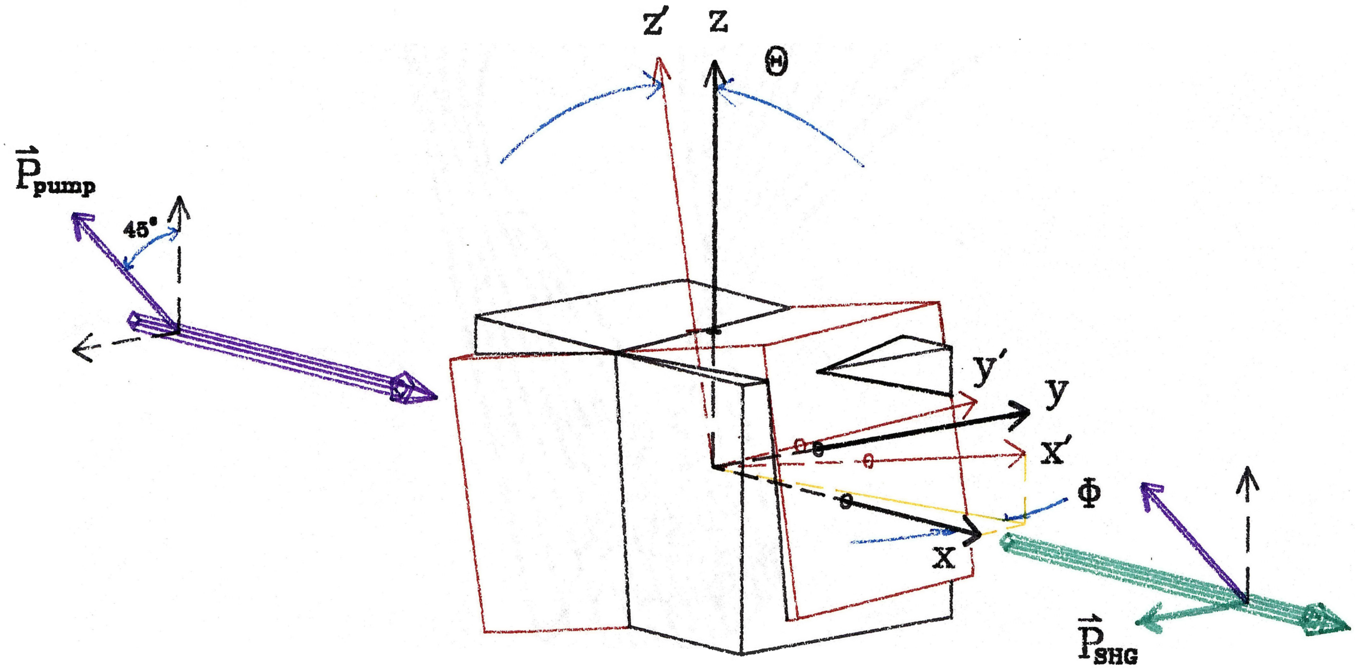

Figure 26. Experimental configuration: The pump beam (shown in purple) will have an incident polarization appropriate for the type of phase matching desired. The polarization state of the pump shown in the figure is appropriate for type II phase matching. The generated second harmonic (SH) is shown as the green beam. The polarization state of the beam shown is likewise, appropriate for type II phase matching. The primed coordinates are fixed with the rotated crystal axes.

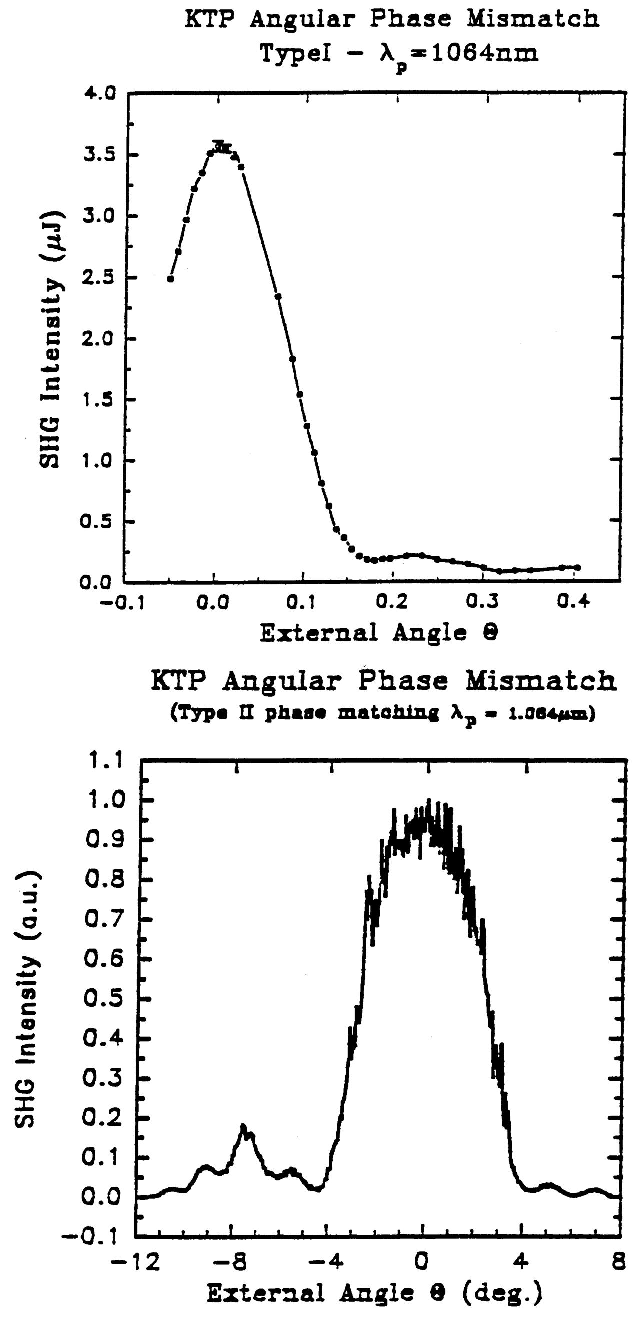

Figure 27. SHG output intensity versus angular phase mismatch in KTP for (a) Type I and (b) Type II phase matching conditions.

resemblance to the sinc^2 dependence predicted by Eq.65, which is the small conversion efficiency expression for the intensity. The angular dependence for Type I phase matching displays a much broader angle of acceptance than anticipated by the theory. The broadening of the angular acceptance can be attributed to the locus of phase matching points located around the chosen Type I phase matching angle. Figure 9 in section V shows this locus of phase matched points around the chosen Type I phase matching angle of $(\theta_m^I, \phi_m^I) \mid_{opt}= 84^o, 45^o$. It is evident form this figure that small angular deviations about the phase matching point, simply results in a new phase matching condition being met, i.e. the new orientation is still phase matched. The convolution of the phase matching locus with the anticipated sinc^2 dependence is needed to correctly describe the angular dependence of the Type I phase matched SH intensity of $\lambda_p = 1064$nm in KTP.

Figures 28 and 29 show the angular dependence of the SH intensity in KTA and RTA, respectively. No angular dependence of the SHG in KCTA was observed which implies that either the sample was characteristically multidomain or KCTA cannot be phase matched for SHG of $\lambda_p = 1064$nm. The angular dependence of the SH intensity observed in both KTA and RTA remotely resembles the anticipated sinc^2 dependence (KTA more so than RTA). In each case, the angle of acceptance is very small (<.1 rad) which implies that both crystals contained a macrodomain which obeyed stringent phase matching conditions. These materials, therefore, hold promise for further study.

Conversion efficiencies were measured for the same set of crystals. Figure 30 shows the slope efficiency curve for the reference sample (Type I phase matched KTP) measured at the phase matching angle (i.e. $\Delta kL = 0$). The theoretical functional dependence of the conversion efficiency at $\Delta k = 0$ was shown in chapter III to be given by Eq.62, i.e.

$$I_{SH}(L) = I_p(L) \tanh^2(\Gamma L). \tag{263}$$

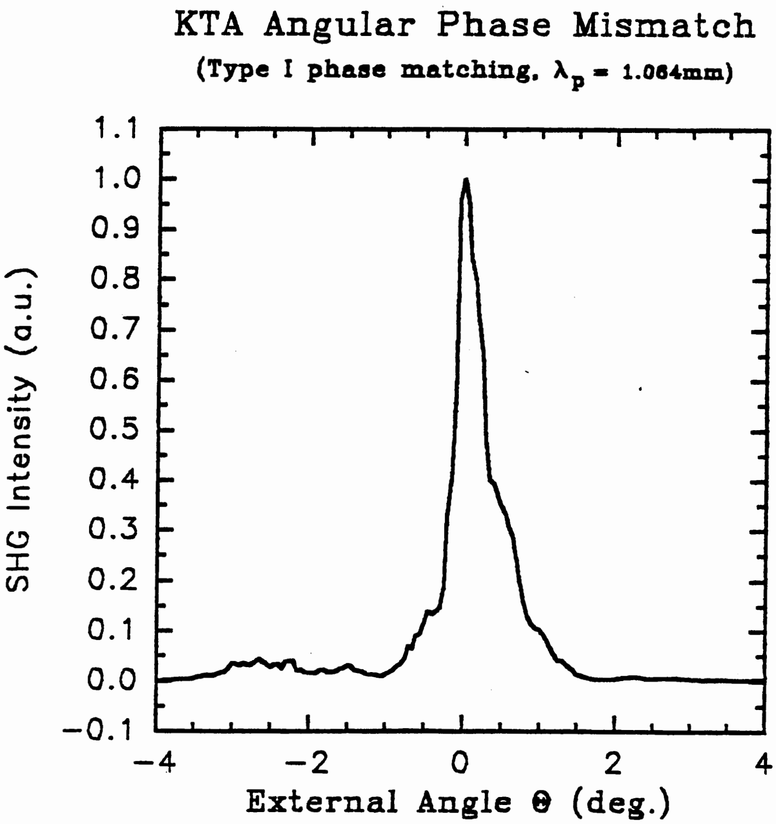

Figure 28. SH output intensity versus angular phase mismatch in KTA for Type I phase matching conditions.

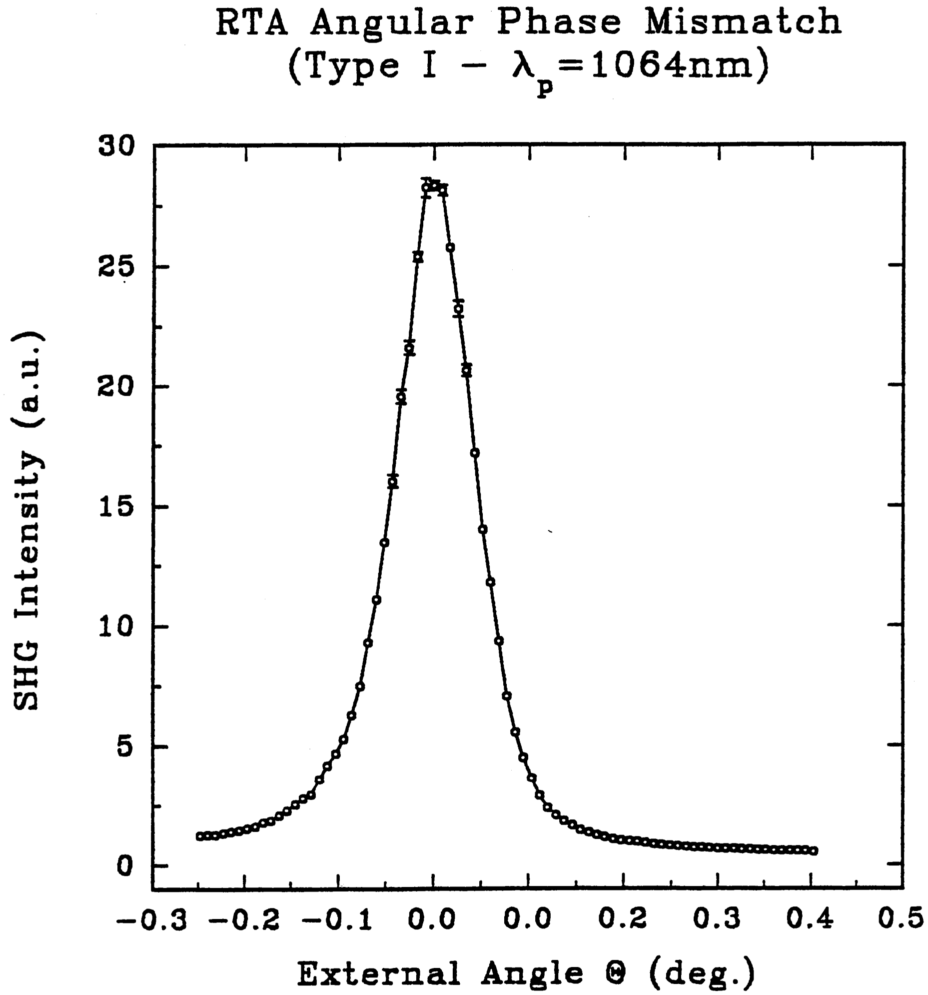

Figure 29. SH output intensity versus angular phase mismatch in RTA for Type I phase matching conditions.

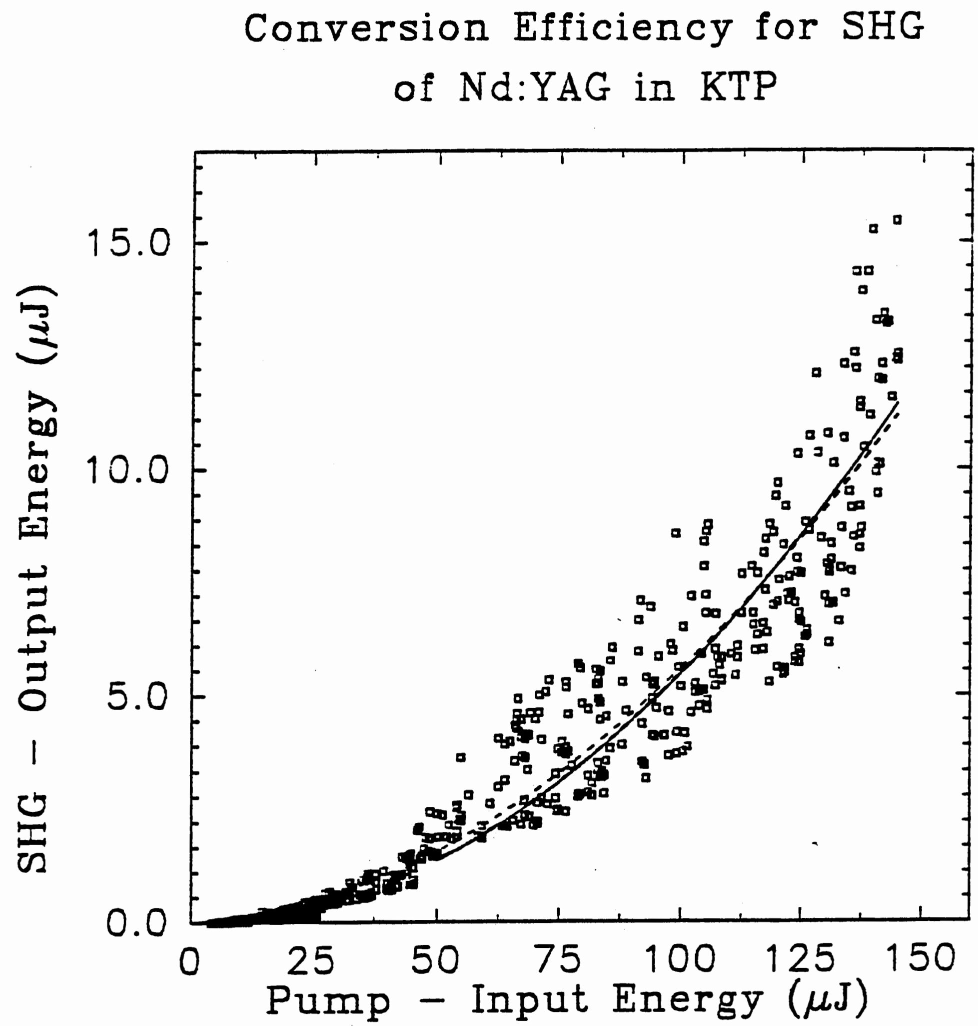

Figure 30. SHG conversion efficiency of $\lambda = 1064\text{nm}$ fundamental pump wavelength in KTP under Type I phase matching conditions. The solid line represents the theoretical fit to Eq.62, whereas the dashed line allows for an additional polynomial correction.

The solid line in Fig.30 represents the theoretical fit of Eq.263 to the data. The gain coefficient is defined to be $G = \Gamma L$, where Γ is given by

$$\begin{aligned} \Gamma &= \kappa_\omega \left|E_p(0)\right| \\ &= \tfrac{\mu_o c \omega}{2n(\omega)} d_{eff} \left|E_p(0)\right|. \end{aligned} \tag{264}$$

Substituting in the relationship between the electric field magnitude and the field intensity, i.e. $I = \frac{nc\epsilon_o}{2}|E|^2$, we find

$$\Gamma = \frac{\omega \sqrt{d_{eff} I_p(0)}}{(nc\epsilon_o)^{\frac{3}{2}}}. \tag{265}$$

Hence, the gain is proportional to the square root of the incident intensity (or energy since $U = \frac{\pi w_o^2}{2} I$ for Gaussian beams). From the fit we found a value for the SH gain coefficient of Type I phase matched KTP to be

$$G^I_{KTP} \simeq 0.06\, U_p \tag{266}$$

where U_p is the energy of the input pump pulse.

Likewise, the conversion efficiency for KTA was measured and is shown as Figure 31. The curves theoretical fit to Eq.263 is shown as the solid line. These fits yielded a gain coefficient of

$$G^I_{KTA} \simeq 0.0002\, U_p. \tag{267}$$

From this data, it is evident that the conditions under which these efficiencies were measured were far from ideal. Under optimum conditions, the theoretical values for the ratios of the gain coefficient between KTP and KTA calculated from Eq.265 is subsequently given by

$$\frac{G^{(I,II)}_{KTA}}{G^{(I,II)}_{KTP}} = \frac{n_{KTP}(\omega)\, d^{(I,II)}_{eff}(KTA)}{n_{KTA}(\omega)\, d^{(I,II)}_{eff}(KTP)}. \tag{268}$$

Evaluating this ratio using the results summarized in Figs. 9 and 10, and the currently available values for the d_{ij} coefficients [40,38] we find

$$\frac{G^{(I)}_{KTA}}{G^{(I)}_{KTP}} \simeq 0.3,$$

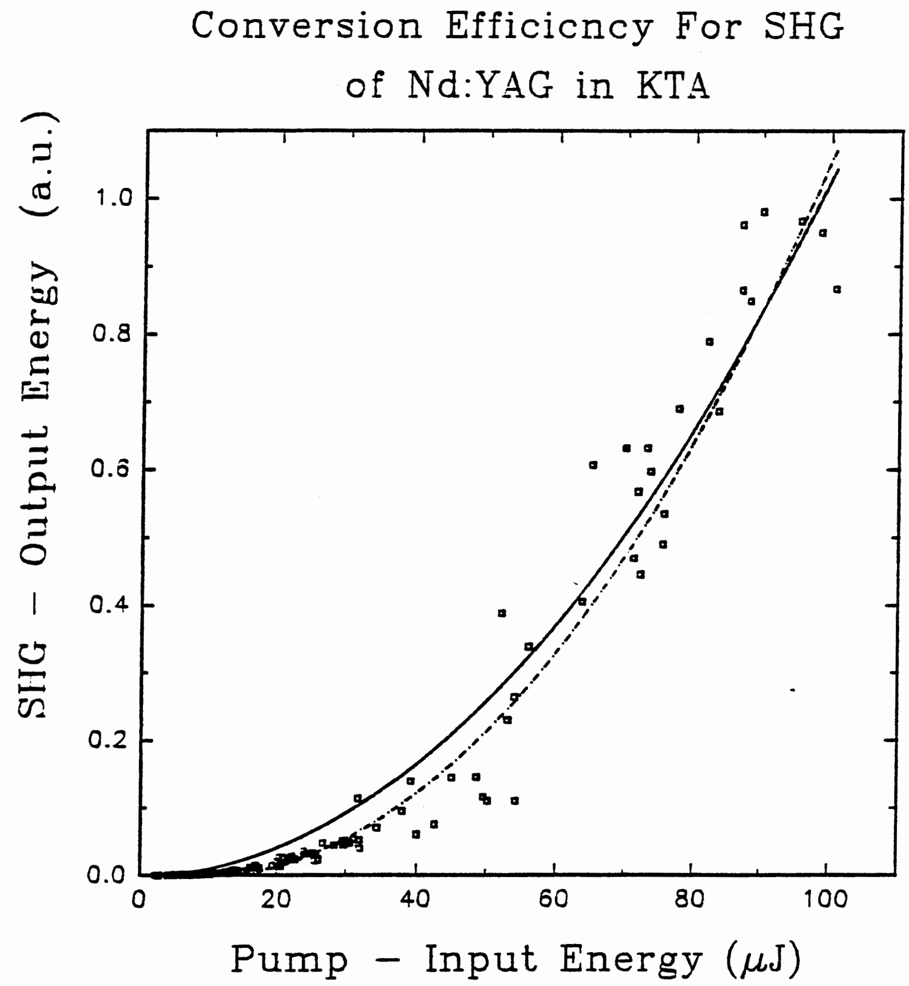

Figure 31. SHG conversion efficiency of $\lambda = 1064$nm fundamental pump wavelength in KTA under Type I phase matching conditions. The solid line represents the theoretical fit to Eq.62, whereas the dashed line allows for an additional polynomial correction.

which is an order of magnitude larger than the ratio obtained experimentally.

The data presented for these new materials show the basic trends anticipated from the theory. We have demonstrated the need for further optimization of the phase matching parameters. Current knowledge of the refractive index data for KTA has provided us with the information necessary to complete this optimization. As was shown in Fig. 11, Type II phase matching in KTA cannot be achieved for fundamental pump beams with wavelengths less than 1.14 μm. Generally, $d^{II}_{eff} > d^{I}_{eff}$, hence Type II phase matching generally results in higher conversion efficiencies. Therefore, future research on KTA will be focused on obtaining Type II phase matched SHG for the 1.1 to 1.25μm output radiation of a Nd:YAG pumped F_{2-}—center laser. Refractive index measurements are currently being performed on RTA, KTA, KCTA. These measurements will allow us to predict the optimum phase matching conditions for these materials.

CHAPTER VIII

OPO: EXPERIMENTAL

In this section we will discuss the experimental procedures and results obtained in the investigation of KTP and KTA OPOs. The initial investigation of the KTP OPO was performed by Jani et al. [72]. The results of these initial investigations are included here for the purpose of comparing KTA to a known standard and to add continuity.

Most of the previous investigations related to optical parametric oscillators (OPOs) have either utilized the variation of the input angle or the temperature to manipulate the phase matching conditions and, hence, the oscillation wavelengths of the signal and idler waves. These two methods are the so-called angle and temperature tuning methods. In this investigation we have taken a different approach. We obtain continuously tunable signal and idler fields by continuously tuning the pump frequency.

The output wavelengths of the signal and idler waves are determined by simultaneously satisfying the energy conservation condition, viz.

$$\frac{1}{\lambda_p} = \frac{1}{\lambda_s} + \frac{1}{\lambda_i} \tag{269}$$

and the phase matching conditions discussed in chapter V. Additional computational blocks have been added to the phase matching computer program in the appendix to calculate the tuning curves of the signal and idler with respect to the tuned pump beam.

The pumping source used was a Light Age alexandrite laser, continuously tunable from 720–800nm. Our results demonstrate extendibility of the tuning range of this laser to wavelengths between 1.40 to 1.63μm for the KTP crystal and a disjointed combined range between 1.43 and 1.71μm for two KTA crystals (hereafter referred to as crystal No. 1 and No. 2).

The phase matching curves for KTP and KTA were calculated and shown as Figs. 13 and 14 of section V. From these curves it is evident that the optimum phase matching type for both KTP and KTA is Type II . The optimum cut angles for KTP and KTA is thus $(\theta_m^{KTP}, \phi_m^{KTP}) \mid_{opt} = 54.91^o, 0^o$ and $(\theta_m^{KTA}, \phi_m^{KTA}) \mid_{opt} = 56.28^o, 0^o$, respectively. In spite of these calculations, the actual cut of both the KTP and KTA crystals was $(\theta_m, \phi_m) \mid_{act} = 54^o, 0^o$. The origin of the discrepancy between the theoretical and actual angle for the KTP is unknown to the author of this thesis. However, the discrepancy between the optimum theoretical angles and angles for which the KTA crystals were cut, is known to be due to the untimely knowledge of both the correct refractive index data [39] and the multidomain structure of the crystals under study. The interaction length of the KTP and KTA crystals were 10.5 and 7.0mm, respectively. The end faces of both crystals were polished flat and parallel but were not anti-reflection coated.

In our investigations we used a doubly resonant oscillator (DRO) configuration. This was done mainly because the DRO displays a lower threshold of operation then does the SRO configuration (c.f. ch.IV). The optical cavity shown in Fig. 32 consisted of a flat mirror that was highly reflecting between 1.3 and 1.8 μm and highly transmitting between 700 and 800nm. The output coupler consisted of a 2m radius of curvature, 98% reflecting mirror over the same range as the high reflector. The cavity length was 4.3cm. The crystals were mounted on a rotation stage with the y-axis in the horizontal plane. The cavity was longitudinally pumped with an alexandrite pump pulse which was polarized along the y-axis of the crystal. This mounting configuration was constructed to assure that the pump beam be an ordinary ray as was specified in the phase matching calculation discussed in section V, i.e. o=o+e.

The pump laser was operated at 10Hz with an output consisting of a series of 300nm wide pulses randomly located within 60μs window. The pump-beam diameter incident the crystal was measured to be 1.82mm (e^{-1} intensity radius). The

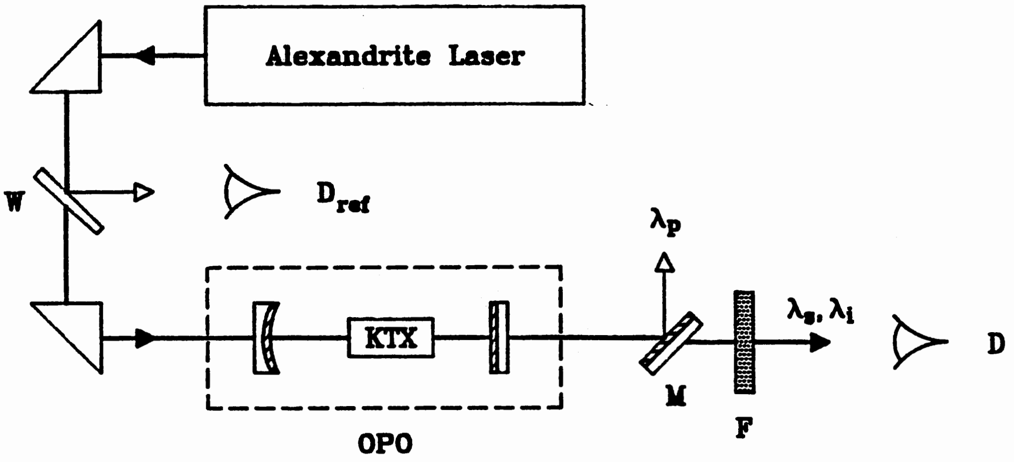

Figure 32. OPO experimental configuration: The Alexandrite pumping laser is referenced of a wedge (W), rather than a slide, to prevent beam phase front distortion from occuring as a result of thin film interference. The optical cavity consists of a 2m HR (highly reflecting) mirror, and a flat (OC) output coupler, separated by 4.3cm. The dichoric mirror (M) and Si-filter (F) were used the filter out the unconverted pump beam. The 'X' in KTX is either 'P' or an 'A'.

output of the cavity consisting of the signal and idler wavelengths was monitored with an InSb detector after passing through a dichroic separator which was highly reflective over the range 700–800nm and highly transmitting over the range 1.3–1.8μm, and a 0.25m Spex monochromator with a 600 grooves/mm grating blazed at 1.25μm.

The theoretically predicted tuning curves for the signal and idler fields are shown in Fig. 33. The resulting tuning curve for the KTP crystal is shown in Fig. 34. It can be seen from this figure that for a pump wavelength of 766nm, the signal and idler wavelengths are approximately degenerate which is not the anticipated 750nm degenerated point. The idler output varies from 1.527 to 1.540μm, whereas the signal varies from 1.40 to 1.62μm, as the pump wavelength varies from 732 to 788 nm. As anticipated, the output signal wave is polarized along the y–axis of the crystal (o-ray) whereas the idler wave is polarized in the x-z plane (e-ray). The solid curves in the figure represent the theoretical tuning curves found by calculating the phase matching angles rendering a degenerate point at λ_p= 766nm, and then requiring that energy conservation hold, i.e. Eq.269.

Utilizing the phase matching computer program in the appendix, the phase matching curves for degenerate operation at $\lambda_p = 766$nm were found and are shown in Fig. 35. From these curves the optimum phase matching angle can be seen to be θ_m^{II}, $\phi_m^{IIt} = (54.33^o, 0^o)\,|_{opt}$ which is consistent with the angles of the actual cut.

The theoretically anticipated tuning curve for KTA phase matched for degeneracy at $\lambda_p = 0.75\mu$m is shown in Fig. 36. The measured tuning curves obtained for both the KTA samples are shown in Fig. 37.

Unlike KTP, the KTA samples did not display degenerate points within the tuning range of the Alexandrite laser. This is partly due to the fact that the particular ferroelectric domains responsible for generating the parametric oscillation were not oriented at the appropriate phase-matching angle needed to obtain degenerate operation and partly due to the untimely knowledge of the index of refraction necessary to calculate the optimum angle.

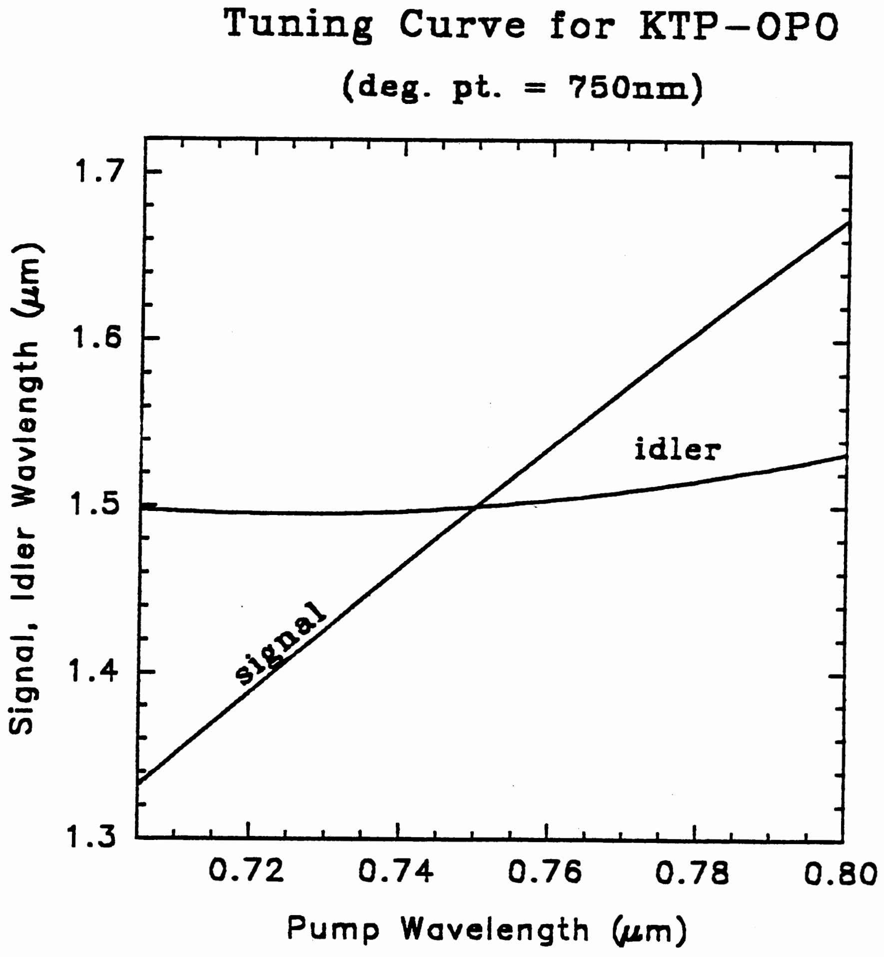

Figure 33. Theoretical tuning curve for KTP OPO operated for the degenerate pump wavelength of $\lambda_p = 750\text{nm}$.

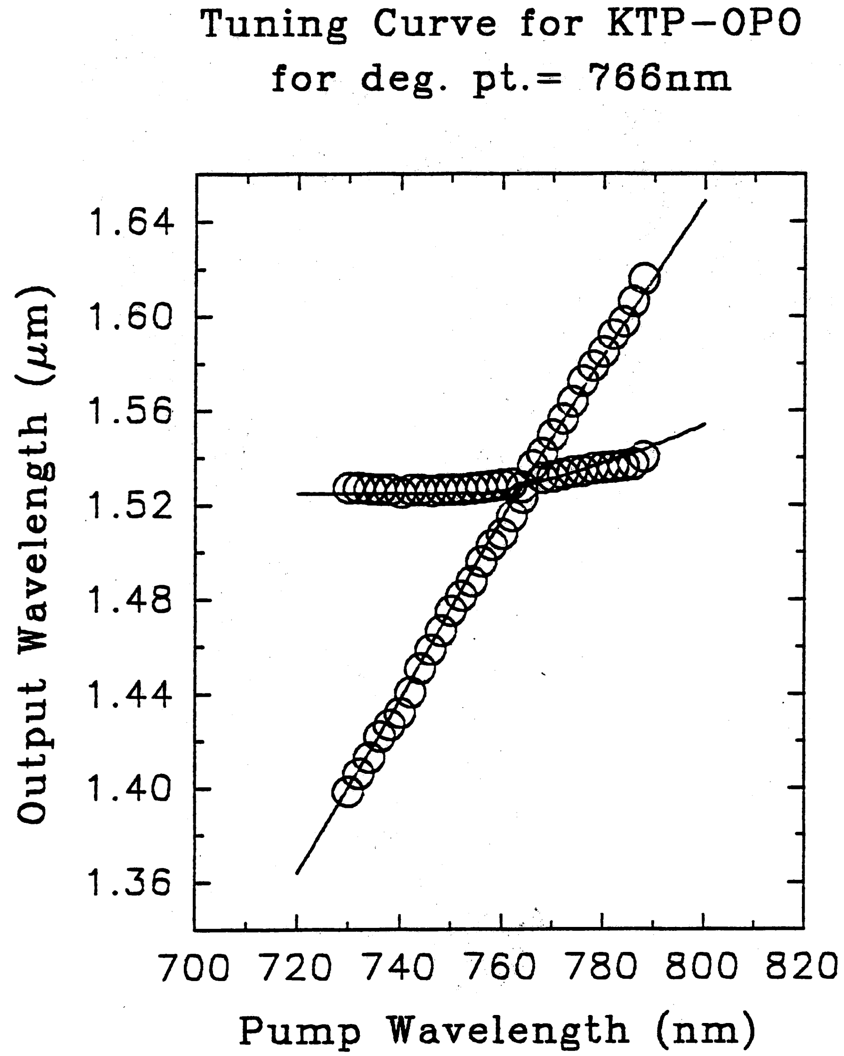

Figure 34. Experimentally obtained tuning curve for KTP OPO. The degenerate point was found to correspond to a pump wavelength of λ_p = 766nm rather than the desired pump wavelength of λ_p = 750nm. The theoretical tuning curves for the degenerate pump wavelength of λ_p = 766nm is shown as the solid line.

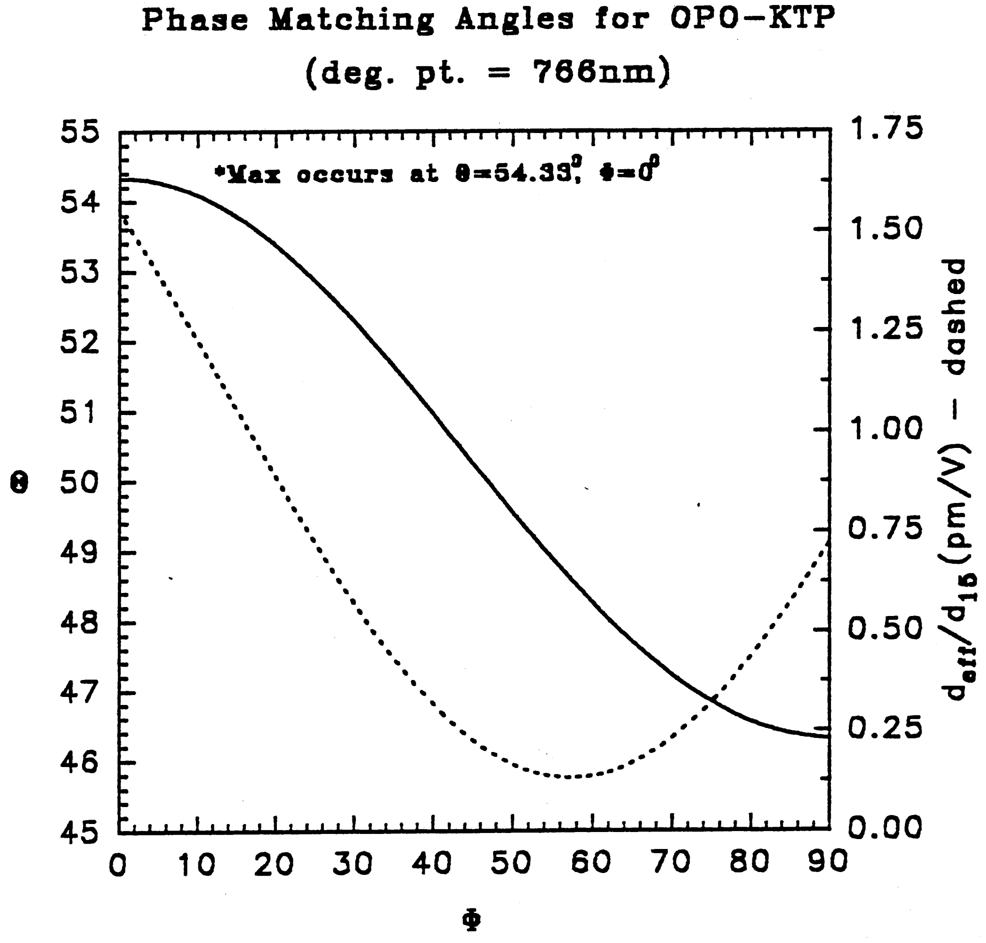

Figure 35. Type II phase matching curves for KTP OPO for the degenerate pump wavelength of $\lambda_p = 766$nm.

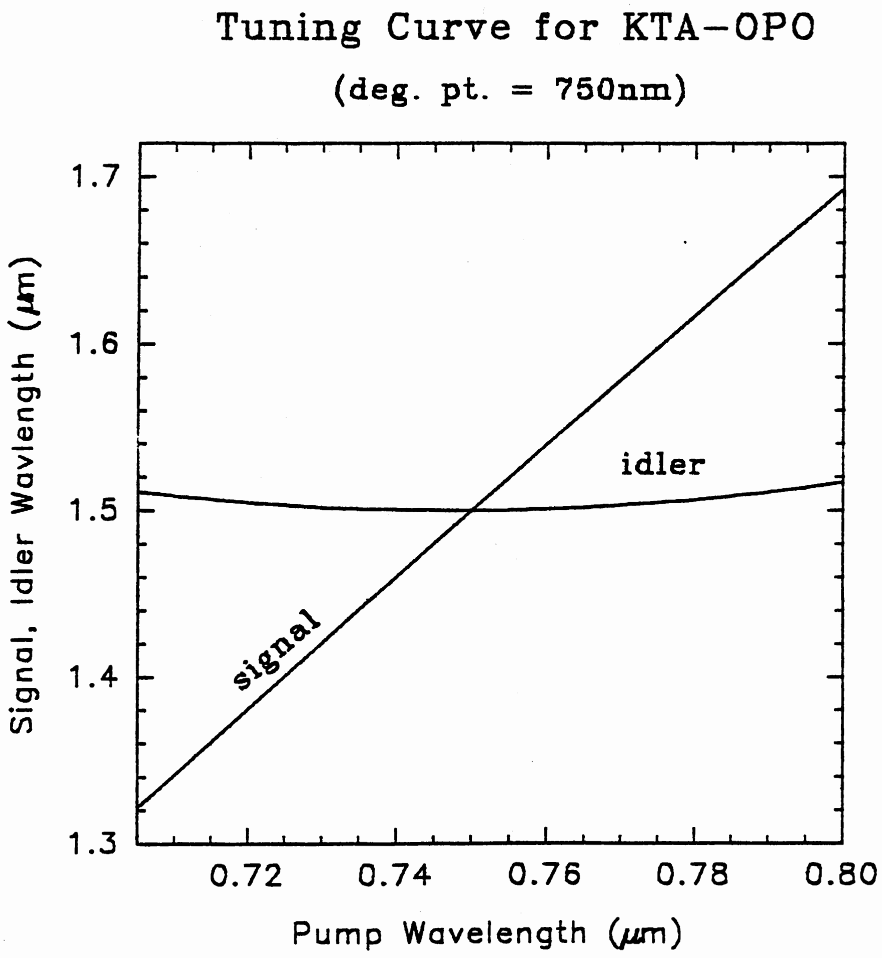

Figure 36. Theoretical tuning curve for KTA OPO operated for the degenerate pump wavelength of $\lambda_p = 750$nm.

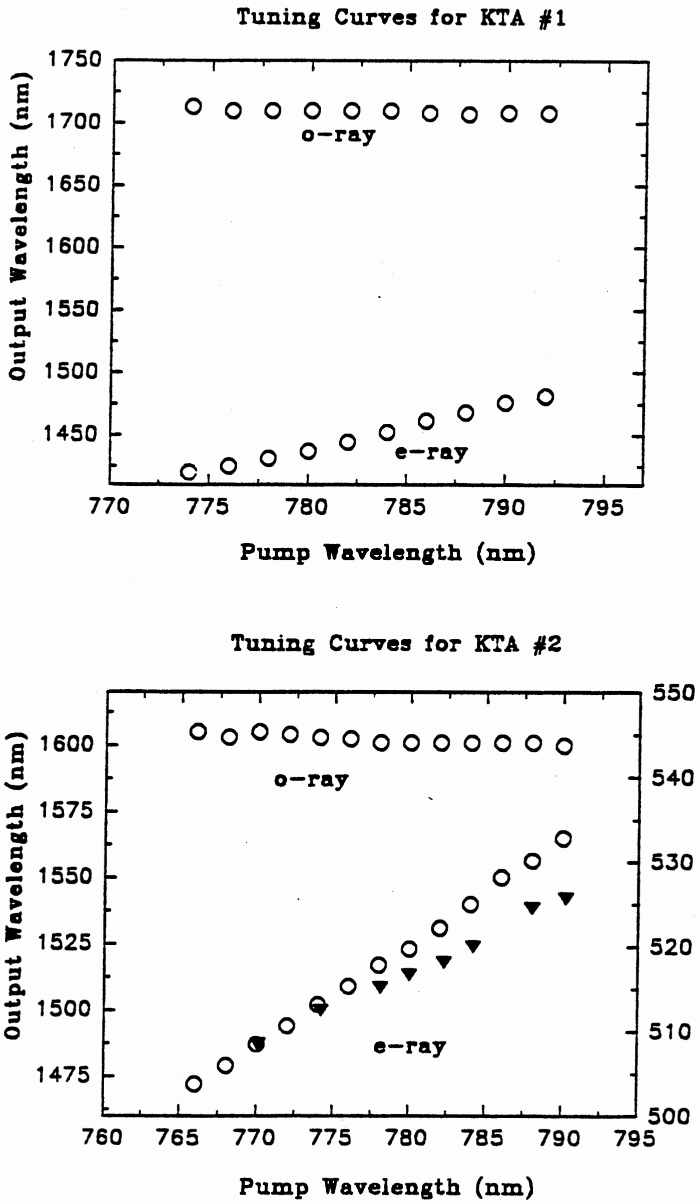

Figure 37. Experimentally obtained tuning curves for KTA OPO. (a) resulting tuning curves for crystal No.1 and (b) for crystal No.2. The filled triangles in (b) represent the observed green output results for the sum frequency mixing of the pump and signal fields.

Both crystals were cut for the same angle, however they displayed different tuning curves. Which leads to the conclusion that each of the two KTA samples must have independent domain structure. Of the two crystals, crystal No. 2 came the closest to having a degenerate point within the active tuning range. Interpolation of the two curves yields an approximate degenerate point around 802nm. This would imply, through a similar calculation as before, that the crystal was actually cut at angles $(\theta_m^{II}, \phi_m^{II})\ |_{act}= 54.09^o, 0^o$ with respect to the active domain. These angles are consistent with the known values.

Also present in the output radiation, with crystal No. 2 in the cavity, was an intense extraneous green emission. The radiation was found to be simultaneous and co–linear with the signal and idler beams. Detuning of the cavity resulted in the elimination of the green emission, thus indicating that this green emission was produced by a frequency mixing process between the infrared and pump beams simultaneously present in the cavity. The green output wavelengths were monitored and are shown as a function of the pump wavelength in Fig. 37 as filled triangles. The values of the observed green wavelengths λ_g, satisfy the energy conservation condition for sum frequency mixing between the pump wavelength λ_p and the signal wavelength λ_s, i.e.

$$\frac{1}{\lambda_g} = \frac{1}{\lambda_p} + \frac{1}{\lambda_s}. \tag{270}$$

The polarization state of this emission was measured to be in the horizontal plane and hence is an ordinary ray. As was mentioned previously, the polarization state of the pump and signal were ordinary and extraordinary, respectively. Therefore the observed frequency mixing process was a result of a Type II phase matching process, i.e. o=o+e. By utilizing measured values of the green emission along with the pump and signal wavelengths, we were able to calculate the possible phase matching angles for this process. The phase matching curve for this mixing process is shown Fig. 38. This graph provides us with evidence that crystal No. 2 was truly multi-domain, since the cut angle of the crystal is out of the range of

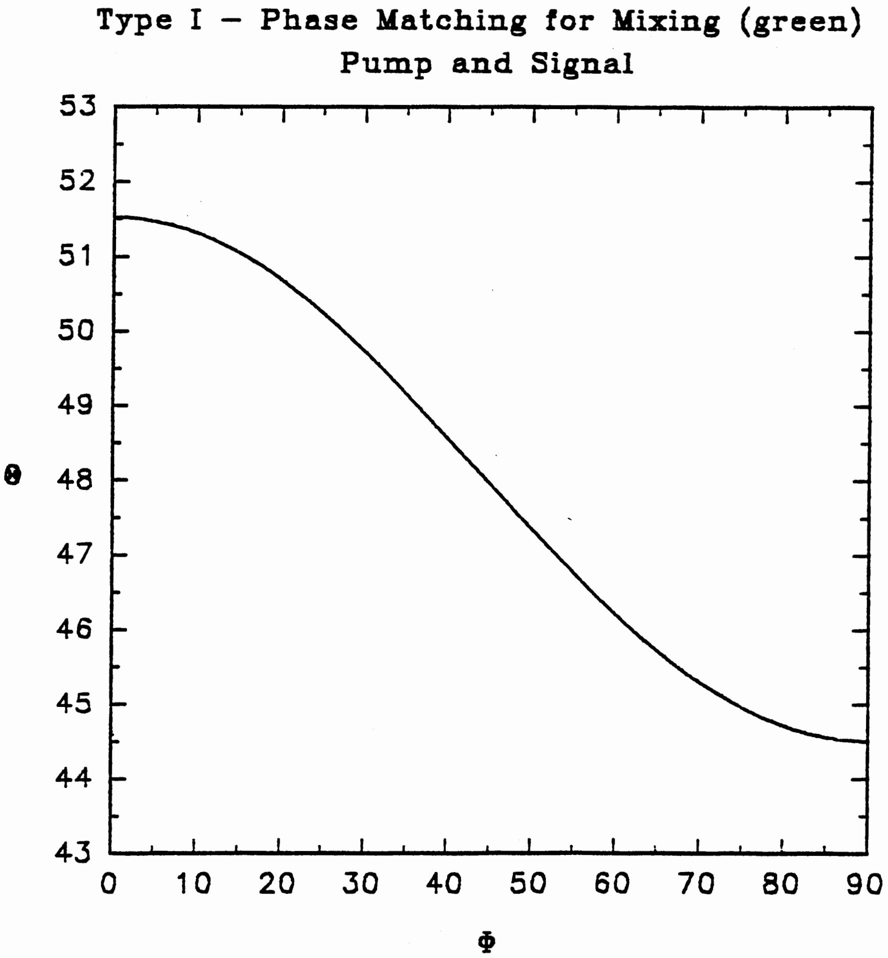

Figure 38. Phase matching curves for sum frequency mixing of the pump and signal fields in a KTA OPO.

angles of the possible phase matched values, i.e. frequency mixing occurred in a separate domain.

The conversion efficiencies and threshold pump intensities were measured, and are shown in Figs. 39 and 40, for pump wavelengths of 766 and 778nm in KTP and KTA, respectively. The total output energy in each case has been corrected for the amount of incident energy coupled into the cavity mode. This factor can be estimated by calculating the amount of pump energy contained in the overlap of the pump beam and the cavity mode volume.

The beam waist of the fundamental cavity mode is calculated in the standard way, i.e. for a hemisphereical cavity the beam waist of the cavity is given by [73],

$$w\,(L) = \sqrt{\frac{\lambda}{\pi}}\left(\frac{L\,R}{1 - L/R}\right)^{1/4} \tag{271}$$

where L is the length of the cavity and R is the radius of curvature of the curve mirror. Substituting in the cavity length, radius of curvature and degenerate wavelength we find the beam waist to be $w_o \simeq 0.39$mm.

The beam waist of the pump beam was measured to be 1.82mm, which is nearly six times the beam waist of the cavity. Consequently, the mode of the cavity was grossly over filled which resulted in very poor coupling. The advantage of overfilling the mode was that the system became less sensitive to misalignment, thus assuring more stable operation.

For a Gaussian spatial beam profile the amount of energy contained within a radius r is given by

$$U(r) = \beta \iint E(r)^* E(r)\, dA \tag{272}$$

where, $E(r) = E_o\, e^{-(r/w_o)^2}$ and $dA = rdrd\phi$. The total energy contained in a pulse is therefore:

$$\begin{aligned} U_T &= \beta\, |E_o|^2 \int_0^{2\pi}\int_0^{\infty} e^{-\frac{2r^2}{w_o^2}} r dr d\phi \\ &= 2\pi\beta\, |E_o|^2\, \frac{w_o^2}{4}. \end{aligned} \tag{273}$$

The amount of energy coupled into the cavity mode is likewise:

$$\begin{aligned} U(w_{mode}) &= \beta \int_0^{2\pi}\int_0^{w_{mode}} e^{-\frac{2r^2}{w_o^2}} r dr d\phi \\ &= U_T\left[1 - e^{-2\left(\frac{w_{mode}}{w_o}\right)^2}\right]. \end{aligned} \tag{274}$$

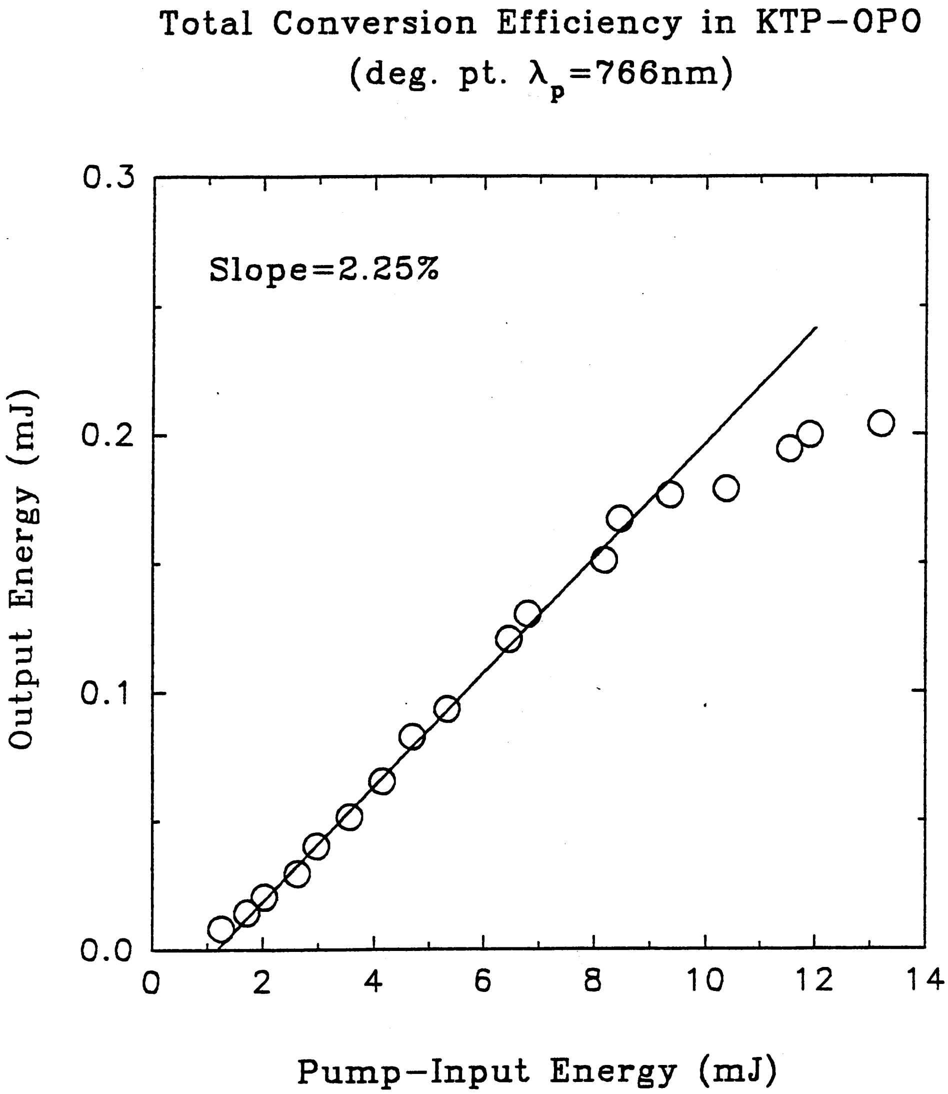

Figure 39. Total conversion efficiency of the KTP OPO. The input energy has been corrected to account for the poor input coupling of the pump with the cavity mode. The solid line corresponds to the theoretical fit to Eq.276.

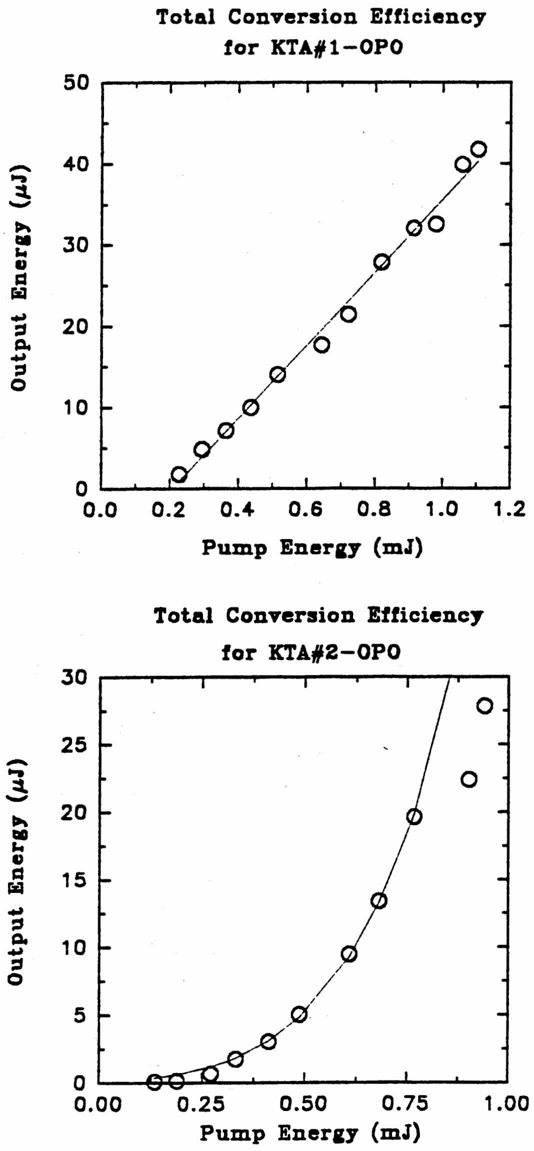

Figure 40. Total conversion efficiencies of the KTA OPO for (a) crsytal No.1 and (b) crystal No.2. The input energy in each has been corrected to account for the poor input coupling of the pump with the cavity mode. The solid lines correspond to the theoretical fit to Eq.276.

Hence, the fraction of energy coupled into the mode is:

$$\begin{aligned}\frac{U_{mode}}{U_T} &= 1 - e^{-2\left(\frac{w_{mode}}{w_o}\right)^2} \\ &= 0.092.\end{aligned} \tag{275}$$

That is, only 9.2% of the total incident pump energy was actually coupled in to the mode of the cavity.

The conversion efficiency curves in Figs. 39 and 40 have been fit to the theoretical expression for the conversion efficiency given by Eqs.111 and 112, i.e.

$$\begin{aligned}\frac{I_s^{(r=1,\Delta k=0)}(L)+I_i^{(r=1,\Delta k=0)}(L)}{I_s(0)+\left(\frac{\omega_i}{\omega_s}\right)I_s(0)} &= e^{2\Gamma L} \\ &= e^{G}.\end{aligned} \tag{276}$$

From these fits we found the experimentally achieved gain coefficients, $G_{KTP} \simeq 1.96\sqrt{U_p}$ and $G_{KTA} \simeq 7.92\sqrt{U_p}$. Recalling the definition of Γ, given by Eq.82, i.e.

$$\begin{aligned}\Gamma^2 &= \frac{2\omega_i\omega_s d_{eff}^2 I_p}{n_i n_s n_p \epsilon_o c^3} \\ &= \frac{8\pi^2(1-\delta^2)d_{eff}^2 I_p}{n_i n_s n_p \epsilon_o c \lambda_o^2}\end{aligned} \tag{277}$$

where we have define δ as a measure of the deviation from degeneracy, i.e. $\omega_i = \omega_o(1+\delta)$ and $\omega_s = \omega_o(1-\delta)$. For Gaussian pulses $U_p = \frac{\pi w_o^2}{2} I_p$, hence:

$$\Gamma^2 = \frac{16\pi(1-\delta^2)d_{eff}^2\, U_p}{n_i n_s n_p \epsilon_o c \lambda_o^2}. \tag{278}$$

Substituting into Eq.278 the measured parameters we find the theoretical values for the gain coefficient G, to be $G_{KTP}^{th} \simeq 2.06\ \sqrt{U_p}$ and $G_{KTA}^{th} \simeq 9.38\ \sqrt{U_p}$ which are in excellent agreement with the gains found for the fit data.

The measured threshold intensities can also be compared the theoretically predicted values by recalling Eq.122 of chapter IV, i.e.

$$I_p^{(th)} = \frac{\alpha_i \alpha_s n_i n_s n_p \epsilon_o \lambda_o^2 c}{8(1-\delta^2) d_{eff}^2\, L^2}\left[\mathrm{sinc}\left(\frac{\Delta k\, L}{2}\right)\right]^{-1}, \tag{279}$$

where α_s and α_i are the roundtrip power losses for the signal and idler waves, respectively. Assuming perfect phase matching, i.e. $\Delta k = 0$, with roundtrip power losses of 2% (since the output coupler was 98% reflective) for both signal and idler, we find, upon substitution of $U_p = \frac{\pi w_o^2}{2} I_p$ into Eq.279, the predicted threshold energies

$$\begin{aligned} U_p^{(th)}(\mathrm{KTP}) &\simeq 0.28 \text{ mJ} \\ U_p^{(th)}(\mathrm{KTA}) &\simeq 0.27 \text{ mJ} \end{aligned} \tag{280}$$

which are in relative agreement with the experimentally found threshold energies of 0.20mJ and 0.25mJ, respectively. The theoretical threshold energies were calculated on the premise that only the first fundamental mode of the cavity was oscillating, which was obviously not the case since the pump beam was large enough to excite multiple mode in the cavity. Each transverse mode of the cavity will have a unique gain and hence build–up time. We can argue that the superposition of all the high gain transverse mode oscillating in the cavity aids to lower the threshold intensity.

CHAPTER IX

SRS: EXPERIMENTAL

We performed experiments utilizing $Ba(NO_3)_2$ in both a single pass configuration and in an intra-cavity configuration. The single pass configuration lends itself to the efficient generation of several Stokes and anti-Stokes components of the pumping laser field. Since these components are generated from a scattering process there output is highly divergent. The intra-cavity configuration generates a single Stokes or anti-Stokes component, depending on the output coupling. The oscillating Raman shifted components in this configuration will assume a spatial mode structure defined by the optical cavity. This will assure that the output have a divergence defined by a cavity mode and therefore will resemble the output of a laser.

Single Pass Conversion

The second harmonic output of a mode locked Nd:YAG laser was used as a pump source in our experiment as shown in Fig. 41 . The output energy and pulse duration of the pump laser was measured to be 2 mJ/pulse and 22±2 ps, respectively. A setup composed of a 60° glass prism, aperture and energy meter was used to measure the absolute SRS efficiency. Additionally, a system composed of a monochromator, photomultiplier tube and digital oscilloscope was used to measure SRS efficiency from a single laser pulse.

The barium nitrate samples were cut along the [110] crystallographic axis. These samples were 50 and 40 mm long with apertures 9x9 and 12x12 mm, respectively. $Ba(NO_3)_2$ crystals are transparent in the spectral region from 340 to 1800nm as shown in Fig.42 .

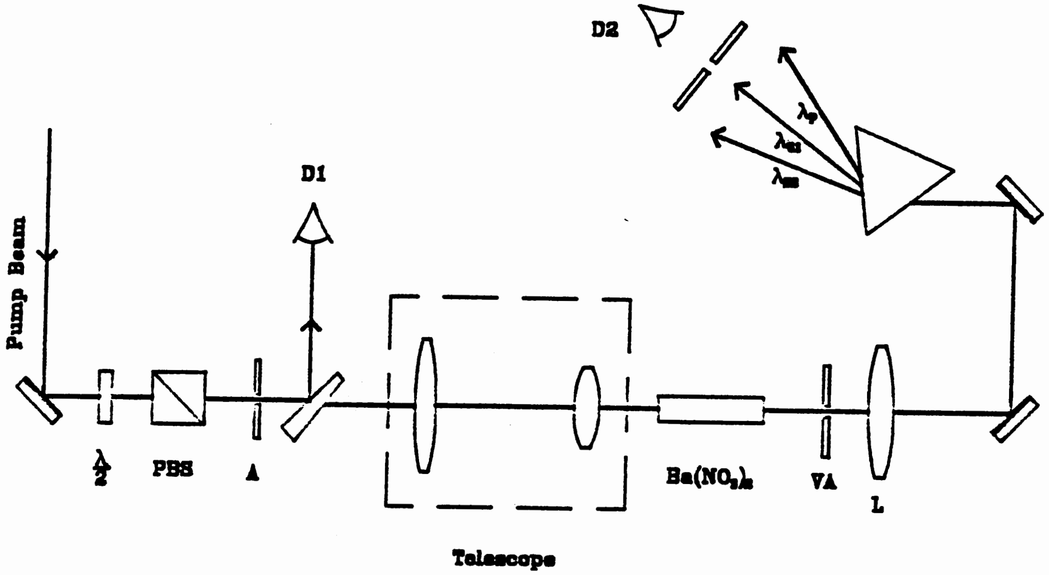

Figure 41. Experimental Setup: The half wave plate ($\frac{\lambda}{2}$) and polarizing beam splitter (PBS) were used as a variable attenuator. The photodiode (D1) was used to monitor the pump energy and the variable aperture (VA) was used to analzse the angular distribution of the scattered light. The Lens (L) collimated the scattered light and the detector (D2), which was either a photomultiplier or energy meter, was used to monitor the scattered light.

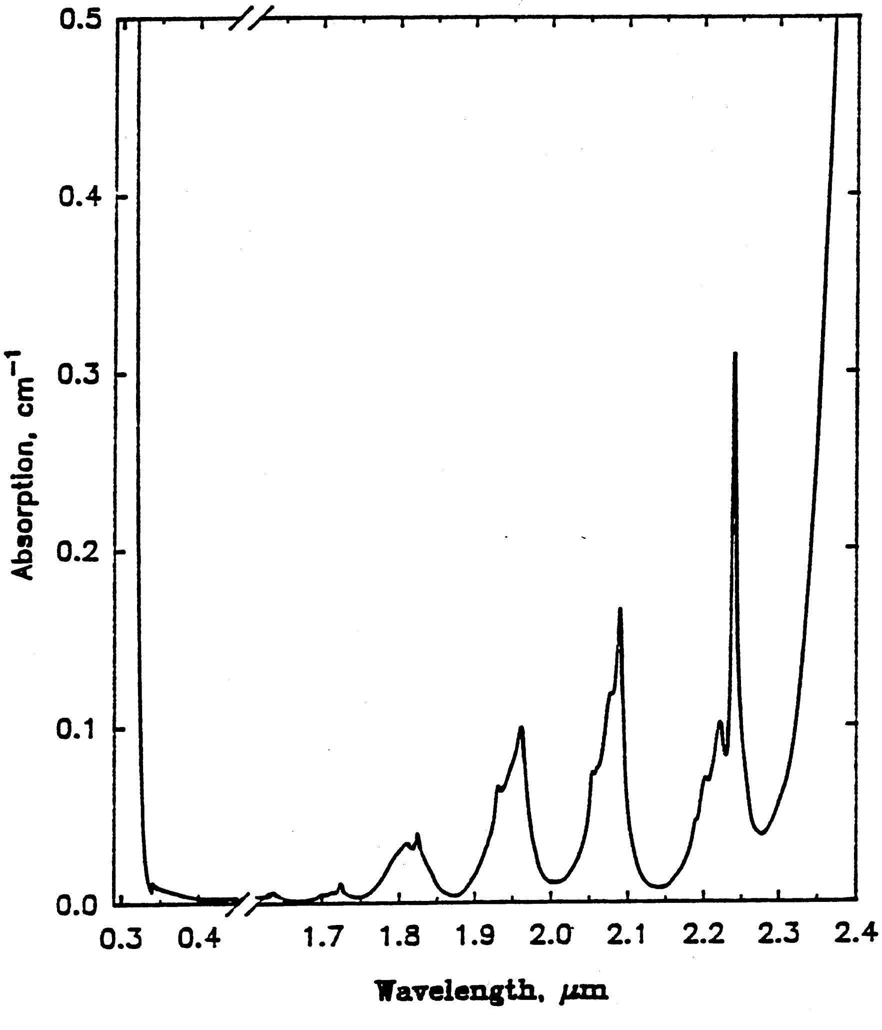

Figure 42. Absorption spectrum of $Ba(NO_3)_2$.

In the forward scattered radiation direction, the first (563 nm), second (599 nm) and third (639 nm) Stokes, and first anti-Stokes (504 nm) components of the 532 nm pump beam were present. Figure 43 shows the forward scattered (inside 1.5° solid angle) first Stokes efficiency on the input pump intensity for crystals of lengths 50 and 40mm. The threshold intensities were measured to be 1.1 and 1.45GW/cm^2, respectively. These are in good agreement with the exponential dependence of the SRS intensities with varying crystal lengths, as predicted by Eq.250, where G_{ss} is replaced by G_{tr}.

The threshold gain obtained from our experimental data and steady state Raman gain g_{ss} obtained from Karpukhin et al. [74], gives $G_{tr}^{(thr)}$=260±30. We will now compare this value to the theoretical value. In order to find this coefficient we must first calculate the predicted steady state gain coefficient G_{ss}, given by Eq.251. Scattering $\lambda_p = 532$nm at the threshold intensity of $I_p(0) = 1$GW/cm^2, with a Raman linewidth of $\Delta\nu_R \simeq 10^9$Hz and Stokes component $\lambda_s = 563$nm, scattered into a solid angle $\Delta\Omega = 10^{-3}$sr, we find using Eq.251 the steady state threshold gain coefficient to be $G_{ss}^{(th)} \simeq 25$.

In order to reach threshold in the transient regime the pump intensity would have to be raised by a factor of F. This factor is determined by the numerical solutions shown in Fig. 24 of section VI. Figure 44 shows the calculated value of F versus (τ_v/τ_p) for a Gaussian shaped pump pulse, where τ_p is the FWHM of the pump pulse, τ_v is the phonon dephasing time and $G_{ss}^{(th)} = 25$. In our experiments the measured values of τ_p and τ_v are 22±2 and 25±2 ps, respectively, hence the ratio $\tau_v/\tau_p = 1.1$. From Fig. 44 we find for this ratio $F \simeq 10$. We therefore expect the transient threshold gain to be on the order of $G_{tr}^{(th)} \simeq 250$, which is in agreement with the aforementioned experimentally measured value of 260±30.

Figure 45 shows the overall efficiency of the first and second Stokes SRS in the 50mm long $Ba(NO_3)_2$ crystal. It can be seen that a first Stokes efficiency of 25% and second Stokes efficiency of 5% can be obtained for an input pump intensity of 2 GW/cm^2. A further increase of the pump intensity leads to saturation of the SRS efficiencies.

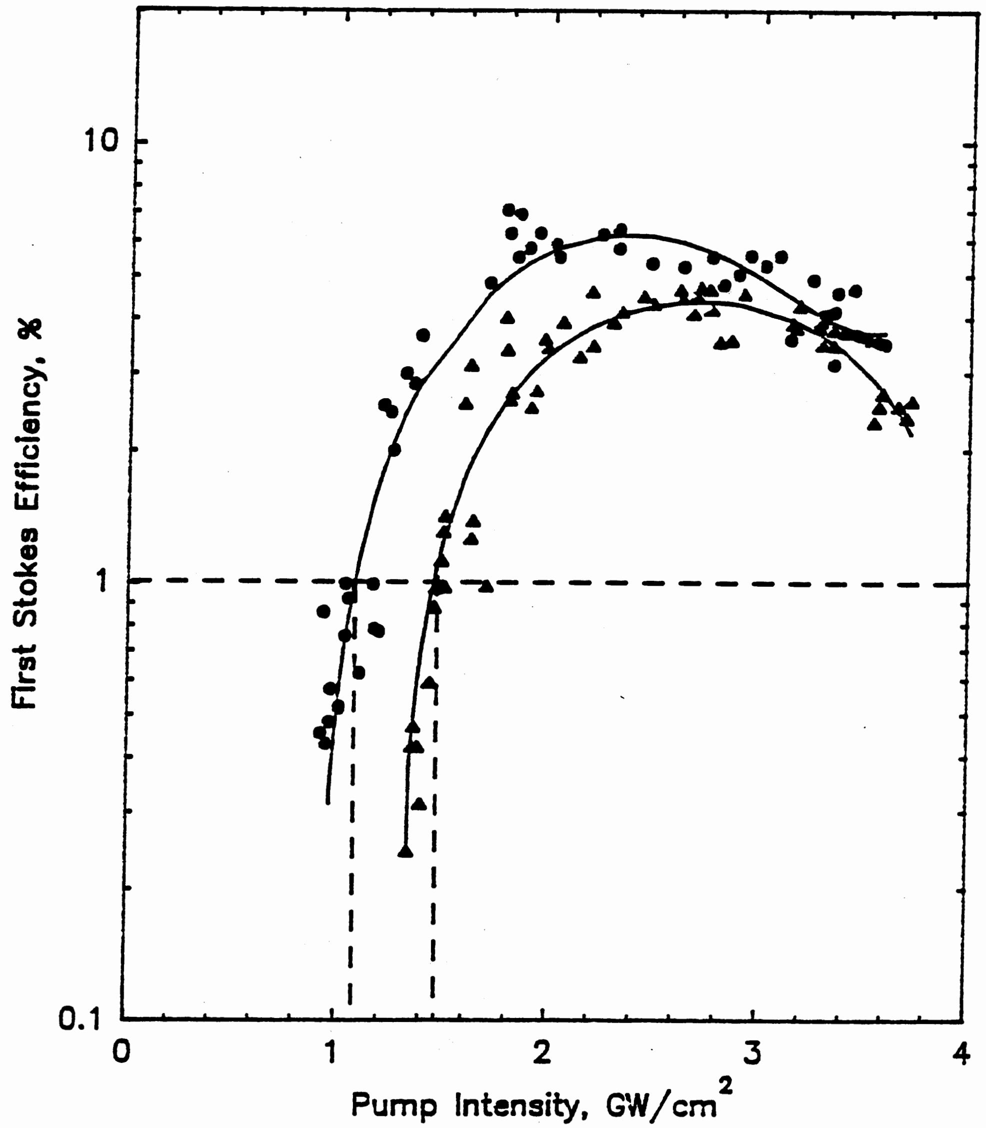

Figure 43. First Stokes SRS output efficiency (scattered in a 1.5° solid angle) versus input pump intensity. The two sets of data correspond to crystals of different length (circles - 50 mm, triangles - 40 mm).

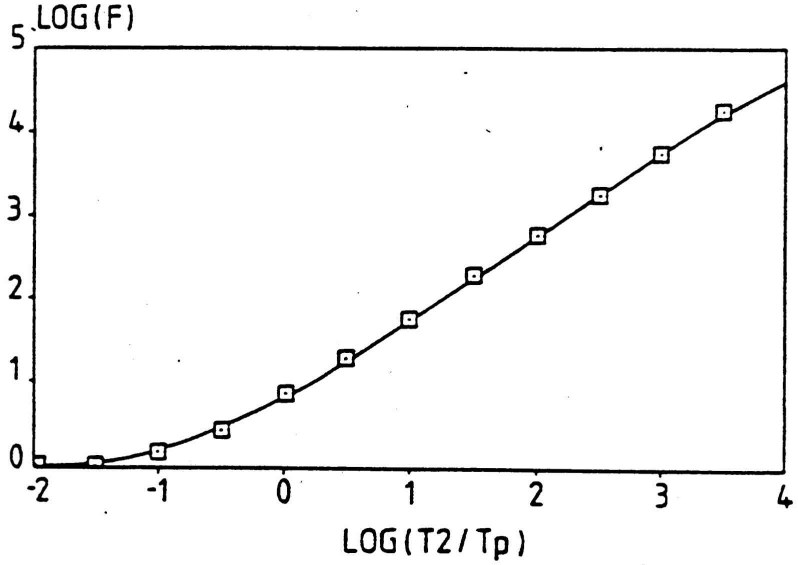

Figure 44. Factor F by which the peak power is increased relative to the steady-state threshold power where τ_p is the FWHM of the Gaussian pump pulse. After Hanna et al. [67]

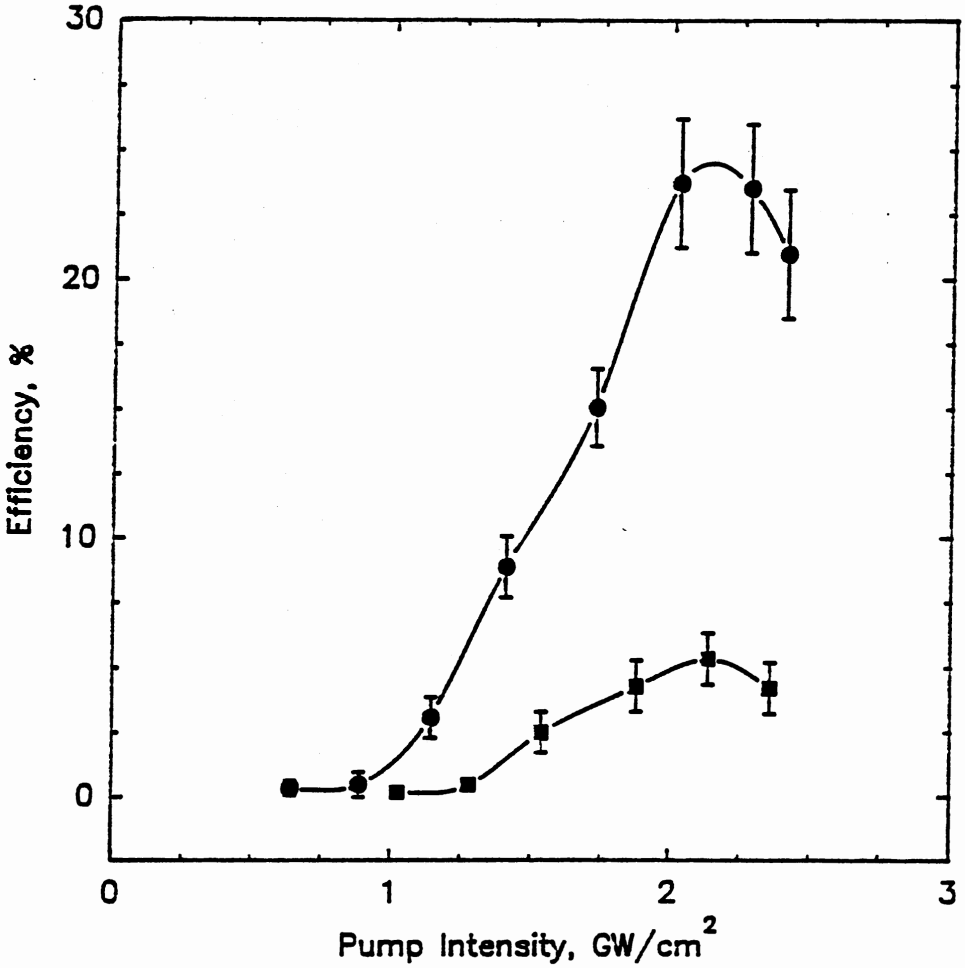

Figure 45. Overall first (circles) and second (squares) Stokes conversion efficiencies versus input pump intensity using a 50mm length $Ba(NO_3)_2$ crystal.

The angular dependencies of the SRS radiation are shown in Fig. 46 for three input pump intensities. As seen in Fig. 46 the divergences of the first and second Stokes radiation increases with the input intensity. The blooming of the first Stokes radiation can be attributed to the onset of the threshold for off-axis SRS. That is, as the pump intensity increases it becomes possible for off–axis spontaneously scattered 1st Stokes radiation to be amplified. Likewise, the second Stokes radiation, created by SRS of the first Stokes component, displays an analogous angular distribution at small angles.

The minima in the curves at 1.9° in Fig. 46 correspond to a null in the off-axis first Stokes radiation, evident as the dark ring in the photograph of the SRS radiation shown in Fig. 47. The missing 1st Stokes radiation is a result of it's coupling with the pump beam, in four photon mixing process, to create the intense ring of the second Stokes radiation. The second Stokes ring is readily apparent as the sharp maxima at 3.6° in the second Stokes angular distribution as shown in Fig. 46 and well defined orange ring in the photograph. Likewise, the intense red ring corresponds to a cone of third Stokes radiation at 5.6°. These rings become diffuse when the pump beam is focused, the result of which is shown as the second photograph in Fig. 47. In the focused geometry elements along the pump beams diameter will enter the medium at different angles, each giving rise to a unique phase matched ring of higher order radiation. The conglomerate of rings, of a particular Stokes component, appears as a single enlarged ring of that Stokes component.

It was determined in section VI that there are two distinct sets of phase matched rings; *Class I*, which obey the phase matching described by Eqs.261 and 262 , and *Class II* which do not. The data required to evaluate Eqs.261 and 262 include the index of refraction and dispersion of $Ba(NO_3)_2$. Unfortunately this data is not currently unavailable. Therefore at this stage we cannot determine the class of radiation observed in our experiments.

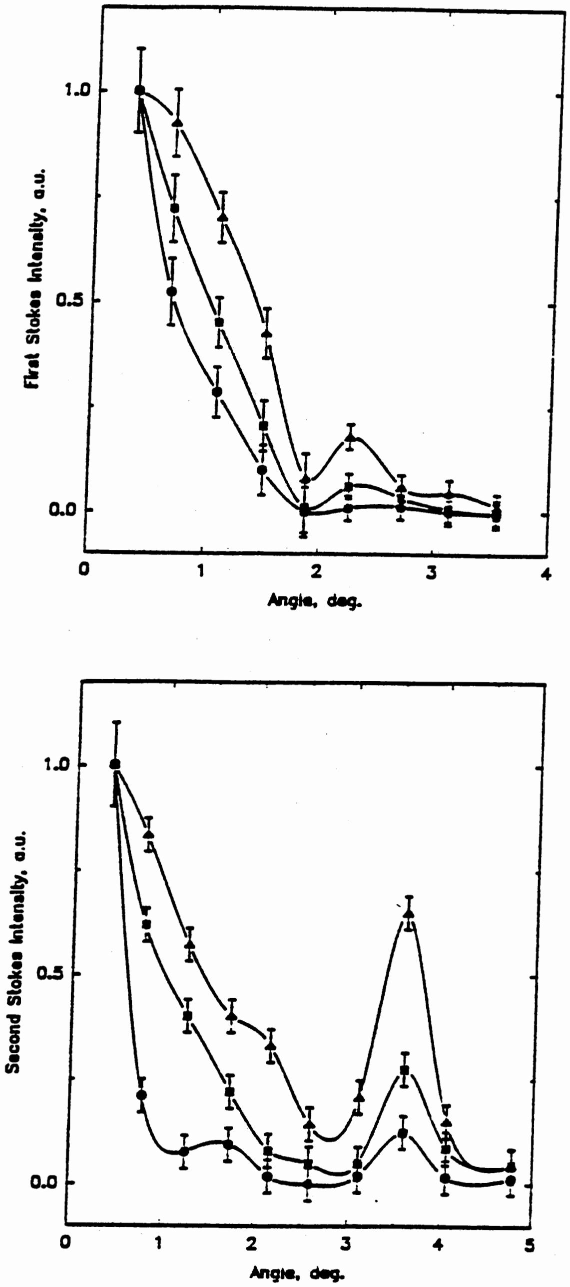

Figure 46. Normalized first (a) and second (b) Stokes angular distribution for different input pump intensities. The circles correspond to 1.4 GW/cm^2, squares to 1.7 GW/cm^2 and triangles to 2.2 GW/cm^2. The sharp minima in (a) and peak in (b) correspond to annihilation of the first and gain of the second Stokes radiation in a four photon process. All angles were measured outside the crystal.

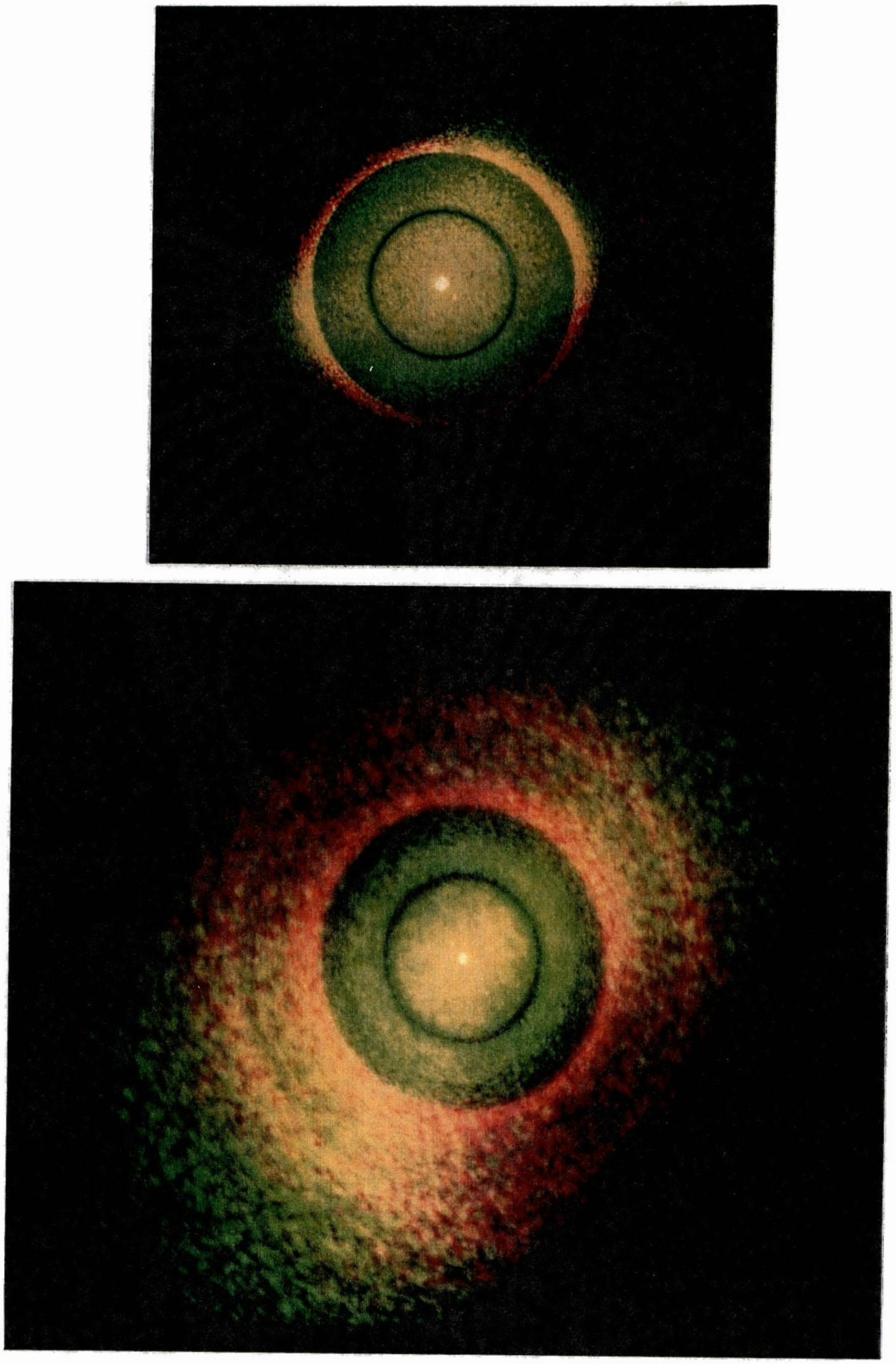

Figure 47. Photograph of the SRS light with the pump beam (a) collimated and (b) focused.

Intra–Cavity Conversion (Raman–Laser)

A Raman laser was constructed using $Ba(NO_3)_2$ as the intra-cavity Raman shifting media. The configuration used for these experiments is shown in Fig. 48. In this configuration a flashlamp pumped Nd:YAG rod was used as the active media. The Q of the cavity was controlled using a LiF:F_{2-}—center crystal as a saturable absorbing media. Normal operation of the Nd:YAG laser, Q–switch with the F_{2-}—center crystal with 90% output coupling yielded 8ns pulses with output energies of $\sim$ 200 mJ/pulse. When the $Ba(NO_3)_2$ was added to the cavity the output coupling of the $\lambda_{Nd:Yag} = 1.064\mu$m oscillation was reduced to less than 1% and the output coupling of the Raman shifted ($1^{\underline{st}}$ Stokes component, $\lambda_S = 1.197\mu$m) was set at 20%. The oscillation wavelength was measured to be $\lambda = 1.197\mu$m with shortened pulse widths of 5ns and with output energies of $\sim$ 30mJ.

The rate equation analysis of the system is currently under investigated. This system is particularly complex, since the saturation element has an emission band centered around the Raman shifted oscillation frequency. The role of the saturable absorber as a self–seeder is therefore being considered.

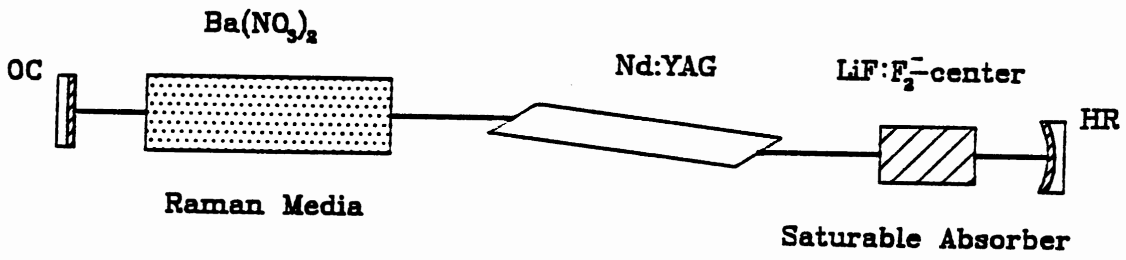

Figure 48. Raman laser configuration. The $Ba(NO_3)_2$ and Nd:YAG are used in conjunction with each other to provide gain for an oscillation wavelength of $\lambda = 1.197\mu m$. The LiF:F_{2-}—center crystal is used as a saturable absorbing Q-switch. The high reflector (HR) is highly reflecting at both 1.064 and $1.197\mu m$, whereas the output coupler (OC) is highly reflecting at $1.064\mu m$ and is 80% reflecting at $1.197\mu m$.

CHAPTER X

CONCLUSIONS

We have shown the new nonlinear optical materials KTA and RTA are potential candidates for efficient second harmonic converts. It was concluded that KTA is not type II phase matchable for the SHG of the Nd:YAG fundamental wavelength. However, it was shown to display type II phase matching for fundamental wavelengths farther out into the IR, making KTA a candidate for efficient doubling of fundamental sources such as the F_{2-}—center laser.

Pump tuned, doubly resonant parametric oscillation was observed, using KTA as the converting media. Sum frequency mixing was also observed to occur between the pump and signal beams, resulting is the emission of tunable green radiation. Increased conversion efficiencies are anticipated with the availability of high quality, single domain crystals.

Efficient, transient SRS was shown to occur in $Ba(NO_3)_2$. Calculations of the threshold intensity are in agreement with predictions for transient SRS. The results show the feasibility of using solid state Raman shifters for producing frequency shifts in the output of picosecond pulse lasers.

We have demonstrated the operation of $Ba(NO_3)_2$ as the active medium in a Raman laser. This laser provides useful output radiation at the rare wavelength of $\lambda = 1.197\mu m$.

BIBLIOGRAPHY

1. Maiman, T.E., *Nature,* **187**, 493 (1960)
2. Zumsteg, F.C., J.D.Bierlein, and T.E.Gier, *J. Appl. Phys.*, **47**, 4980 (1976)
3. Bierlein, J.D., H.Vanherzeele, *J. Opt. Soc. Am. B*, **6**, 622 (1989)
4. Drude, P., *Annalen der Phys.,* **1**, 560 and **3**, 369 (1900)
5. Goldstein, H., *"Classical Mechanics,"* 2nd ed. (Addison–Wesley 1980)
6. Pershan, P.S.,"*Progress in Optics,* "ed. E. Wolf, (North–Holland Publishing Co., 1966)
7. Franken, P.A., A.E. Hill, C.W. Peters, and G. Weinreich, *Phys. Rev. Lett.*, **7**, 118 (1961)
8. Franken, P.A. and J.F. Ward, *Rev. Mod. Phys.*, **35**, 23 (1963)
9. Kleinman, D.A., *Phys. Rev.,* **128**, 1761 (1962)
10. Bloembergen, N. , *Prog. IEEE*, **51**, 124 (1963)
11. Bloembergen, N., *"Nonlinear Optics,"* (W.A. Benjamin, Inc., N.Y. 1965)
12. Kleinman, D.A., A. Ashkin, and G.D. Boyd, *Phys. Rev.*, **145**, 338 (1966)
13. Bjorkholm, J.E., *Phys. Rev.*, **142**, 126 (1966)
14. Armstrong, J.A., N. Bloembergen, J. Ducuing, and P.S. Pershan, Phys. Rev., **127**, 1918 (1962)
15. Akhmanov, S.A., A.I. Kovrygin, and A.P. Sukhorukov, "Optical harmonic generation and optical frequency multipliers", in *Quantum Electronics: A Treatise,* vol. 1, part B, H. Rabin and C. L. Tang, Eds. N.Y. (1975)
16. Rustagi, K.C., S.C. Mehendale, and Meenakshi, *IEEE J. Quant. Elec.*, **QE–18,** 1029 (1982)
17. Eckhardt, R.C., J. Reintjes, *IEEE J. Quant. Elec.,* **QE–20**, 1178 (1984)
18. Gradshteyn, I.S., I.M. Ryzhik, "*Table of Integrals, Series, and Products,*" 4th ed. (Academic Press, 1980)

19. Maker, P.D., R.W. Terhune, M. Nisenoff, and C.M. Savage, *Phys. Rev. Lett.,* **8**, 21 (1962)

20. Yariv, A., "*Quantum Electronics,*" 2rd ed. (Wiley, 1989)

21. Shen, Y.R., "*The Principles of Nonlinear Optics,*" (Wiley 1984)

22. Giordmaine, J.A., and R.C. Miller, *Phys, Rev., Lett.*, **14**, 973 (1965)

23. Kingston, R.H., *Proc. IRE,* **50**, 472 (1962)

24. Kroll, N.M., *Phys. Rev.,* **127**, 1207 (1962)

25. Akhmanov, S.A., and R.V. Khokhlov, *Zh.Eksp. Teor. Fiz.,* **43**, 351 (1962). Transl., *Sov. Phys., JETP* **16**, 252 (1963).

26. Smith, R.G., "Optical Parametric Oscillators", in *Laser Handbook, sec.C8,* ed. F.T. Arecchi and E.O. Schulz–DuBois (North–Holland Publ. Co., 1972)

27. Byer, R.L.,"Optical Parametric Oscillators", in *Quantum Electronics: A Treatise,* vol. 1, part B, H. Rabin and C. L. Tang, Eds. (Academic Press, 1975)

28. Zernike, F., J.E. Midwinter, "*Applied Nonlinear Optics*", (Wiley, 1973)

29. Manley, J.M., and H.E. Rowe, *Proc. IRE,* **47**, 2115 (1959)

30. Giordmaine, J.A., *Phys. Rev. Lett.,* **8**, 19 (1962)

31. Hobden, M.V., *J. Appl. Phys.,* **38**, 4365 (1967)

32. Ito, H., H. Naito, H. Inaba, J. Appl. Phys., **46**, 3992 (1975)

33. Born, M., and E. Wolf, "*Principles of Optics*", 6th ed. (Pergamon Press, 1987)

34. Kleinman, D.A., *Phys. Rev.,* **126**, 1977 (1962)

35. Nye, J. F., "*Physical Properties of Crystals*", (Oxford Univ. Press, 1957)

36. Elliott, J.P., and P.G. Dawber, "*Symmetry in Physics*", (Oxford Univ. Press, 1990)

37. Kato, K., *IEEE J.Quant. Elec.*, **QE–24**, 3 (1988)

38. Vanherzeele, H., J.D.Bierlein, *Opt. Lett.*, **17**, 982 (1992)

39. Chang, K., personally comunicated (du Pont).

40. Bierlein, J.D., H.Vanherzeele, A.A.Ballman, *Appl. Phys.Lett.*, **54**, 783 (1988)

41. Loiacono, D., personally comunicated (Crystal Associates, Inc.).

42. Basiev, T.T., K. Yu, K. Voron'ko, S.B. Mirov, V.V. Osiko, and A.M. Prokhorov, *Izv., Akad., Nauk SSSR Ser. Fiz.,* **46,** 1600 (1982)

43. Kaiser, W., and M. Maier, "*Laser Handbook*", vol.2, ed. F.T. Arrecchi, E.O. Schultz–Dubois (North–Holland, Amsterdam 1972).

44. Eckhardt, G., *IEEE J. Quant. Elec.*, **QE–2**, 1 (1966)

45. Santos, R.A. , P. Tang, W. Chien, S. Kwan, G.S. Harbison, *J. Phys. Chem.,* **1990**, 2717 (1989)

46. Menzies, A.C., *Proc. Roy. Soc. Lond.,* **134**, 289 (1931)

47. Winston, H., and R.S. Halford, *J. Chem. Phys.,* **17**, 607 (1949)

48. Fately W.G., F.R. Dollish, N.T. McDevitt and F.S. Bentley, "*Infrared and Raman Selection Rules for Molecular and Lattice Vibrations: The Correlation Method,*" (Wiley 1972)

49. Wychoff, R.W.G., "*Crystal Structures*", vol.2, 480 (Wiley, 1964)

50. Brooker, M.A., D.E. Irish, G.E. Boyd, *J. Chem. Phys.,* **53**, 1083 (1970)

51. Watson, P. spontaneous Raman spectra.

52. Woodbury, E.J., W.K. Ng, *IRE,* **50**, 2347 (1962)

53. Woodbury, E.J., G.M. Eckhardt, U.S. Patent no. 3,371,265 (27 Feb. 1968)

54. Eckhardt, G.M., R.W. Hellwarth, F.J. McClung, S.E. Schwartz, D. Weiner, E.J. Woodbury, *Phys. Rev. Lett.,* **9**, 455 (1962)

55. Geller, M., D.P. Bortfeld, W.R. Sooy, *Appl. Phys. Lett.,* **3**, 36 (1963)

56. Stoicheff, B.P., *Phys. Letters,* **7,** 186, (1963)

57. Eckhardt, G.M., D.P. Bortfeld, M. Geller, *Appl. Phys. Lett.,* **3**, 137 (1963)

58. Minck, R.W., R.W. Terhune, W.G. Rado, *Appl. Phys. Lett.,* **3**, 181 (1963)

59. Hellwarth, R.W., *Phys. Rev.,* **130**, 1850 (1963), *Appl. Opt.,* **2**, 847 (1963)

60. Shen, Y.R., N. Bloembergen, *Phys. Rev.,* **137**, A1786 (1965)

61. Bloembergen, N., *Am. J. Phys.,* **35**, 989 (1967)

62. Grasyuk, A.Z., *Sov. J. Quant. Elec.***4**, 269 (1974)

63. Partanen, J.P., and M.J. Shaw, *J. Opt. Soc. Am. B,* **3**, 1374 (1986)

64. Wang, C.S., *Phys. Rev.,* **182**, 482 (1969)

65. Forsyth, A.R., "*Theory of Differential Equations*", vol. **V**, 120–130 (Dover 1959)

66. Carmen, R.L., F. Shimizu, C.S. Wang, N. Bloembergen, *Phys. Rev.,* **A2**, 60, (1970)

67. Hanna, D.C., D.J. Pointer, and D.J. Pratt, *IEEE J. Quant. Elec.,* **QE-22**, 322 (1986)

68. Terhune, R.W., *Solid State Design,* **4**, 38 (1963)

69. Chiao, R.Y., B.P. Stiocheff, *Phys. Rev. Lett.,* **12**, 290 (1964)

70. von der Linde, D., M. Maier, W. Kaiser, *Phys. Rev.,* **178**, 11 (1969)

71. Sacchi, C.A., C.H. Townes, J.R. Lifshitz, *Phys. Rev.,* **174**, 439 (1968)

72. Jani, M.G., R.C. Powell, B. Jassemnejad, R. Stolzenberger, *Appl. Opt.,* **31**, 1998 (1992)

73. Siegman, A.E., "*Lasers*" (University Science Books 1986)

74. Karpukhin, S.N., and A.I. Stepanov, *Sov. J. Quant. Elec.,* **16**, 1083 (1970)

APPENDIX

APPENDIX

PHASE MATCHING PROGRAM

This appendix contains a Mathmatica computer program, written in conjunction with Xie Jie and Dr. Bahaeddin Jessemnejad at the University of Central Oklahoma Physics Department. The program has the capability of calculating the phase matching angles and tuning curves for biaxial crystals with known indices of refraction. The indices of refraction for KTP and KTA are written in the form of Sellemier's equation, of second order, where 'y' is the wavelength measured in microns (μm).

A comprehensive description of phase matching was presented in Chapter V. The 'DegeneratePoint' procedure will calculate the phase matching angles for the degenerate signal and idler field in an OPO, and will calculate the phase matching angles for SHG of a given pump field wavelength.

"Indices of refraction of KTP — K. Kato, *IEEE Quant. Elec.,* **QE-24**, 3 (1988)";

$$\mathrm{nx}_{KTP}[\mathrm{y}]=\mathrm{Sqrt}[3.0129+0.03807/(\mathrm{y}^2\text{-}0.04283)\text{-}0.01664\mathrm{y}^2];$$

$$\mathrm{ny}_{KTP}[\mathrm{y}]=\mathrm{Sqrt}[3.0333+0.04106/(\mathrm{y}^2\text{-}0.04946)\text{-}0.01695\mathrm{y}^2];$$

$$\mathrm{nz}_{KTP}[\mathrm{y}]=\mathrm{Sqrt}[3.3209+0.05305/(\mathrm{y}^2\text{-}0.05960)\text{-}0.01763\mathrm{y}^2];$$

"Indices of refraction of KTA — K. Chang (du Pont), privately communicated"

$$\mathrm{nx}_{KTA}[\mathrm{y}]=\mathrm{Sqrt}[2.1106+1.0318/(1\text{-}(0.2106/\mathrm{y})^2)\text{-}0.0106\mathrm{y}^2];$$

$$\mathrm{ny}_{KTA}[\mathrm{y}]=\mathrm{Sqrt}[2.3889+0.7790/(1\text{-}(0.2378/\mathrm{y})^2)\text{-}0.0150\mathrm{y}^2];$$

$$\mathrm{nz}_{KTA}[\mathrm{y}]=\mathrm{Sqrt}[2.3472+1.1011/(1\text{-}(0.2402/\mathrm{y})^2)\text{-}0.0174\mathrm{y}^2];$$

"Phase-matching calculation based on J.Q.Yao, T.S.Fahlen; *J.Appl.Phys.*,**55**(1), 65 (1984)"; Since KTP follows the relationship nx<ny, nz it is a pos. biaxial crystal, i.e. n(e-ray)>n(o-ray). We must, therefore select, for Type II phase-matching, np=no ('+' in np), since the index for the pump must be smaller than the index of the sig. and idler. We must also set ns=no(ne) ('-(+)' in ns), ni=ne(no), i.e. o=o+e(e=e+o). The two possible types are commonly referred to as Type IIa and Type IIb, respectively.";

$$\begin{gathered}Bp=Cos[phi]^2Sin[theta]^2(ny[xp]^{-2}+nz[xp]^{-2})\\+Sin[phi]^2Sin[theta]^2(nx[xp]^{-2}+nz[xp]^{-2})\\+Cos[theta]^2(nx[xp]^{-2}+ny[xp]^{-2});\end{gathered}$$

$$\begin{gathered}Cp=Cos[phi]^2Sin[theta]^2ny[xp]^{-2}nz[xp]^{-2}\\+Sin[phi]^2Sin[theta]^2nx[xp]^{-2}nz[xp]^{-2}\\+Cos[theta]^2nx[xp]^{-2}ny[xp]^{-2};\end{gathered}$$

$$np[theta,phi,xp]=1/Sqrt[Bp+Sqrt[Bp^2\text{-}4Cp]];$$

$$\begin{gathered}Bs=Cos[phi]^2Sin[theta]^2(ny[xs]^{-2}+nz[xs]^{-2})\\+Sin[phi]^2Sin[theta]^2(nx[xs]^{-2}+nz[xs]^{-2})\\+Cos[theta]^2(nx[xs]^{-2}+ny[xs]^{-2});\end{gathered}$$

$$\begin{gathered}Cs=Cos[phi]^2Sin[theta]^2ny[xs]^{-2}nz[xs]^{-2}\\+Sin[phi]^2Sin[theta]^2nx[xs]^{-2}nz[xs]^{-2}\\+Cos[theta]^2nx[xs]^{-2}ny[xs]^{-2};\end{gathered}$$

$$ns[theta,phi,xs]=1/Sqrt[Bs\text{-}Sqrt[Bs^2\text{-}4Cs]];$$

$$\begin{gathered}Bi=Cos[phi]^2Sin[theta]^2(ny[xi]^{-2}+nz[xi]^{-2})\\+Sin[phi]^2Sin[theta]^2(nx[xi]^{-2}+nz[xi]^{-2})\\+Cos[theta]^2(nx[xi]^{-2}+ny[xi]^{-2});\end{gathered}$$

```
Ci=Cos[phi]^2Sin[theta]^2ny[xi]^-2nz[xi]^-2
+Sin[phi]^2Sin[theta]^2nx[xi]^-2nz[xi]^-2
+Cos[theta]^2nx[xi]^-2ny[xi]^-2;

ni[theta,phi,xi]=1/Sqrt[Bi+Sqrt[Bi^2-4Ci]];


DegenPoint=Block[{x,x1,x2,dx,xs,xi,xp,phi,phi1,phi2,dphi,theta,},

xs =2 x;  xi =2 x  ;xp =  (1/xs+1/xi)^-1;

{x1= 0.75 ; x2= 0.75; dx = 0.314;

phi1= -N[Pi/2]; phi2 = N[Pi/2]; dphi=N[Pi/50]};

f1[theta_] := FindRoot [np[theta,phi,xp] - xp/xs ns[theta,phi,xs]

-xp/xi ni[theta,phi,xi] = = 0, {theta, {0.1,1,0.1}];

Do[Print["xp = ", xp , ","] ; Print["phi = ", phi * N[180/Pi],","];

Print[f1[theta]], {x,x1,x2,dx}, {phi,phi1,phi2,dphi}]]


PumptuneSig = Block [ {xp,xp1,xp2,dxp,xs,xi,phi,theta,theta1,theta2,dtheta },

x = x_p;  xi =(xp xs)/(xs - xp); phi = 0; xp1= 0.7; xp2 = 0.8; dxp

theta1 = -N[Pi/2]; phi2 = N[Pi/2]; dphi=N[Pi/50]};.
```

```
f2[xs]:=FindRoot[np[theta,phi,xp] - xp/xs ns[theta,phi,xs]
    -xp/xi ni[theta,phi,xi] = = 0, {xs,0.3, 0.2}}];

Do[Print[”xp=”,xp,”,”]; Print[“theta = ”, N[theta(180/Pi)],”,”];

Print[f2[xs]],xp,xp1,xp2,dxp,theta,theta1,theta2,dtheta]]

PumptuneIdler=Block[{xp,xp1,xp2,dxp,xs,xi,phi,theta,theta1,theta2,dtheta },

x = x_p; xs =(xp xi)/(xi - xp); phi = 0;xp1= 0.7; xp2 = 0.8; dxp
    theta1 = -N[Pi/2]; phi2 = N[Pi/2]; dphi=N[Pi/50]};

f3[xi] := FindRoot[ np[ theta, phi , xp]- xp/xs ns[theta,phi,xs]
    -xp / xi  ni [ theta , phi , xi ] = = 0,{xi,0.3, 0.2}];

Do [ Print [“xp = ”, xp, ”,”] ; Print [ “theta = ”,N[theta(180/Pi)],”,”];

Print [f3[xi]],xp,xp1,xp2,dxp,theta,theta1,theta2,dtheta]]
```

VITA

JAMES THOMAS MURRAY

Candidate for the Degree of

Master of Science

Thesis: FREQUENCY CONVERSION IN NEW NONLINEAR OPTICAL MATERIALS

Major Field: Physics

Biographical:

Personal Data: Born in Colorado Springs, Colorado, USA, November 25, 1966, the son of Norman and Margaret Murray.

Education: Graduated from Centennial High Scool, Pueblo Colorado, May 1985; recieved Bachelor of Science Degree from the Colorado School of Mines, Golden, Colorado in December, 1989, with a major in Physics Engineering; completed the requirements for the Master of Science Degree in Physics at Oklahoma State University, Stillwater, Oklahoma, December, 1992.